Paleodynamics and organic carbon characteristics in a thermokarst affected landscape in West Alaska

MSc. Research GEO4-1520

2016 - 2017

Submitted by

Loeka L. Jongejans

Supervision

Utrecht University:	Dr. Francien Peterse
Alfred Wegener Institute Potsdam:	Dr. Jens Strauss
	Dr. Josefine Lenz

Affiliated and funded by the ERC Project PETA-CARB

The weather varies, as do your dreams

Table of contents

List of figures

List of tables

Abbreviations and nomenclature

Notation	Meaning	SI-unit
°	degree	
°C	degree Celsius	273.15 °K
‰	per mille	
^{14}C	radiocarbon; radioactive isotope of carbon	
a	Latin: annus; year	$3.1536*10^{7}$ s
ACL	average chain length	
AMS	accelerator mass spectrometry	
BD	bulk density	kg m^{-3}
BIT	branched and isoprenoid tetraethers	
BP	before present [referring to 1950]	
brGDGTs	branched glycerol diakyl glycerol tetraethers	
cal	calibrated	
CBT	cyclisation of branched tetraethers	
cm	centimeter	10^{-2} m
cm^3	cubic centimeter	10^{-6} m^3
CPI	carbon preference index	
DTM	digital terrain model	
eV	electronvolt	$1.6*10^{-19}$ J
g	gram	10^{-3} kg
GFZ	German Research Center for Geosciences	
Gt	gigaton	10^{12} kg
ka	Latin: kilo annus; thousand years	$3.1536*10^{10}$ s
km^2	squared kilometer	10^{6} m^2
m	meter	
m/z	mass-to-charge ratio	
MAAT	mean annual air temperature	
MAT	mean annual temperature	
MBT	methylation of branched tetraethers	
mg	milligram	10^{-3} g
MIS	Marine Isotope Stage	
ml	milliliter	10^{-6} m^3
mm	millimeter	10^{-3} m
Mt	megaton	10^{9} kg
ng	nanogram	10^{-9} g

nm	nanometer	10^{-9} m
NSO	nitrogen-, sulfur- and oxygen-containing compounds	
Ø	diameter	
OC	organic carbon	
p	or p-value; probability for a statistical test used in the context of null hypothesis	
Pa	Pascal	
PETA-CARB	junior group at AWI; Rapid permafrost thaw in a warming Arctic and Impacts on the Soil Organic Carbon Pool	
pH	potential of hydrogen	
pMC	percent modern carbon; 100 pMC = atmospheric ^{14}C concentration in 1950	
ppm	parts per million	
psi	pounds per square inch	$1.450377*10^{-4}$ Pa
RPM	rounds per minute	
s	second	
SI	international system of units	
SOC	soil organic carbon	
TC	total carbon	
TIC	total inorganic carbon	
TN	total nitrogen	
TOC	total organic carbon	
u	unified atomic mass unit	$1.6605*10^{-27}$ kg
v/v	percent concentration volume/volume	
vol%	percent per volume	
VPDB	Vienna Pee Dee Belemnite	‰
WIV	wedge-ice volume	
wt%	weight percentage	
$\delta^{13}C$	isotopic ratio between stable carbon isotope ^{13}C and ^{12}C	
µg	microgram	10^{-6} g
µl	microliter	10^{-9} m^3
µm	micrometer	10^{-6} m
ρ_s	mineral density	kg m^{-3}
Σ	sum	
φ	soil porosity	

Abstract

Keywords: yedoma, Baldwin Peninsula, late Quaternary, depositional environment, organic carbon

Global warming will continue to warm the Arctic resulting in the degradation of permafrost soils which leads to large-scale ground subsidence. Vast regions of the Arctic are covered with ice-rich silts, known as yedoma, containing large ice wedges. The formation of thermokarst lakes is one of the most important forms of permafrost degradation. Consequently, large amounts of previously freeze-locked organic carbon (OC) can be mobilized and released, which is of global significance for the carbon cycle.

The aim of this research was to reconstruct the late Quaternary depositional environment and organic carbon characteristics of a thermokarst affected landscape, to better understand the processes involved in thermokarst development and identify the vulnerability of the organic carbon. Fieldwork was conducted on Baldwin Peninsula during the summer expedition in 2016 in West Alaska. Yedoma and drained thermokarst lake basin (DTLB) exposures were sampled and a thermokarst lake core was taken. Sedimentological and biochemical parameters, as well as lipid biomarkers were analyzed. A land cover classification map was made from the peninsula using Landsat imagery and a digital terrain model. By extrapolation of the field data, an estimation of the OC quantity on the peninsula and the loss since the Late Pleistocene was made.

Yedoma deposition started > 50 cal ka BP whereas the DTLB deposits and thermokarst lake sediments originate from the Holocene. The grain size distributions show that the yedoma and DTLB deposits accumulated in a dominantly aeolian, stable regime. Yedoma was deposited in a drier and colder climate than the DTLB, as indicated by the lower BIT index (mean BIT: 0.94 for yedoma and 1.00 for DTLB) and MBT index.

About 53 Mt of OC is stored in the frozen deposits on Baldwin Peninsula and it is estimated that the net loss since the Late Pleistocene is 3 Mt OC. The frozen DTLB deposits contain the largest share of OC (36 Mt, 70%). However, the yedoma deposits contain the most labile OC, as has been shown by the CPI (mean: 11.6 for yedoma and 8.8 for DTLB). This OC has been freeze-locked and not or barely altered by microbial degradation. The OC is terrestrially derived for the yedoma and DTLB deposits. The thermokarst lake shows a lacustrine input (mean $\delta^{13}C$ -28.5‰).

Because of the high ice content of the deposits on the Baldwin Peninsula, the deposits are highly susceptible and vulnerable to permafrost thaw. The high quality of the stored OC in the yedoma deposits makes these carbon pools an important source for microbial alteration. This poses an important input of carbon to the carbon cycle.

1. Introduction

1.1 Scientific relevance and background

Global warming will lead to increased carbon dioxide (CO_2) and methane (CH_4) emission (e.g. from wetlands) into the atmosphere, which leads to further warming (carbon cycle feedback). Melting of snow and ice will decrease surface albedo which will result in higher absorption of the surface (ice-albedo feedback). Also, warming will lead to higher evaporation rates, which will increase atmospheric water vapor concentrations, which is a greenhouse gas (water vapor feedback). The above-mentioned feedbacks are positive feedbacks: the processes are caused by and will amplify the warming. According to the Intergovernmental Panel on Climate Change (IPCC; 2014), the global mean surface temperature increase at the end of the 21th century (2081-2100) will likely be in the range between 1.5 and 2.0°C due to the increased greenhouse effect.

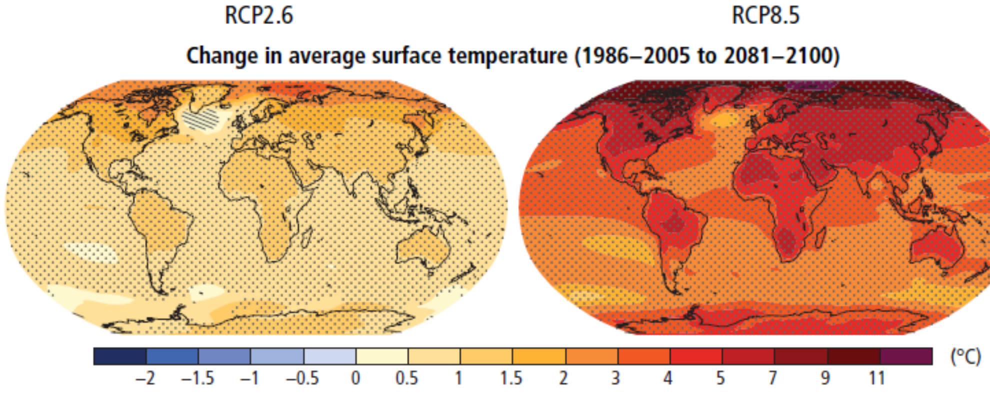

Figure 1.1: Change in average surface temperature based on multi-model mean projections for 2081-2100 relative to 1986-2005.RCP2.6: stringent mitigation scenario, RCP8.5: scenario with very high greenhouse gas emissions. From IPCC (2014)

The Arctic region is and will keep warming more rapidly than the global mean (Figure 1.1). This phenomenon is called Arctic amplification, which is likely caused by sea ice and snow cover (positive) feedbacks (Hansen et al., 1997). The Arctic is especially vulnerable to climate change as large areas are underlain by permafrost, i.e. perennially frozen soils. Top-down thawing of permafrost will continue with ongoing climate change. Ground ice bodies will melt fast which will trigger large-scale ground subsidence. This process is called thermokarst which leads to disturbances in the landscape and sediment composition (van Everdingen, 1998). Coastal and river erosion will increase due to a higher sea-level level, higher seawater temperatures, reduced sea-ice content and greater river discharge (Grosse et al., 2011). Such topographic changes also pose a risk to infrastructure. According to Hugelius et al. (2014), around 1,300 Gt of soil organic carbon (SOC; global total is ~2,500 Gt) is stored in the upper 1 m of the northern permafrost region, of which 800 Gt is perennially frozen. Depending on time and temperature, part of the stored carbon can be decomposed. On average, the loss of organic carbon (OC) ranges from 17 to 34% for organic soils and 6 to 13% for mineral soils (average decade-long loss; Schuur et al., 2015).

The freezing of soil ceases the process of decomposition. Ongoing climate change, however, will rapidly thaw the frozen soils, which results in a potential reactivation of this sequestered carbon pool (Schuur et al., 2015; Vonk et al., 2015). The carbon can be reworked by microbial decomposition and released into the atmosphere as greenhouse gases, or transported and buried in other reservoirs such as lakes, rivers and oceans. Late Pleistocene ice-rich yedoma deposits contain labile organic carbon that is highly decomposable (Zimov et al., 2006a). Molecular biomarkers can be used to analyze the molecular composition and the quality of the organic carbon. The quality of the OC is the degree of degradation; in this study the OC is referred to as poorly degraded (high quality; when little or no degradation has occurred) and further degraded (low quality). To estimate future release of greenhouse gases from permafrost soils, the quantity and quality of OC needs to be studied.

In this thesis, late Quaternary sediments were studied. The Quaternary is divided into the Pleistocene (2.588 Ma to 11.7 ka BP) and the Holocene (11.7 ka BP to today) (section 2.3, Table 2.1). A reconstruction of the Earth's past climate helps to explain how certain environments developed. Also, data from the past can be used as input for climate models. Sediment archives store information about the past climate and depositional environment. Permafrost archives need to be studied to better understand the processes involved in permafrost degradation, as well as to decipher potentially analogue changes in the past. Moreover, it is highly relevant to characterize the organic carbon pools so that the potential vulnerability to future permafrost degradation can be identified. To analyze the molecular composition and the degree of degradation of the organic carbon, sedimentological and biochemical parameters, as well as molecular biomarkers were analyzed. Sediment samples were taken from the Baldwin Peninsula, a thermokarst affected landscape in the permafrost region in West Alaska. Three landscape units were studied: Late Pleistocene yedoma deposits, Holocene thermokarst drained lake basin deposits and modern thermokarst lake sediments.

1.2 Objectives

The aim of this research is to reconstruct the landscape development of the Baldwin Peninsula, West Alaska, during the late Quaternary with the focus on organic-matter pools. The data from sediment archives give insights into thermokarst dynamics and organic carbon characteristics. Furthermore, the reconstruction leads to a better understanding of past climates, which is necessary for understanding the future. A multi-proxy approach is applied on sediment samples taken from three stratigraphic landscape units: yedoma deposits, drained thermokarst lake deposits and thermokarst lake deposits. This thesis includes three objectives:

(1) Characterizing the sediments from thermokarst affected landscapes, which will be addressed using the following questions: (I) What were paleoenvironmental conditions during and after deposition and (II) what is the regional coverage of the deposits?

(2) Characterizing organic-matter pools, for which the following questions were asked: (I) How much organic carbon is stored, (II) what is the origin and (III) what is the quality of the stored carbon?

(3) Deciphering stratigraphical differences, for which the following question was raised: How do sedimentological and biochemical parameters differ between thermokarst and yedoma deposits?

2. Geological and geographical background

2.1 Periglacial environments and permafrost

Periglacial is derived from the words ‘peri’ (Greek: around) and ‘glacial’, in other words: areas around glaciated areas. Periglacial environments are characterized by freezing and thawing of ground and they are dominated by permafrost. Permafrost can be defined as (the state of) ground of which the temperature is at or below 0°C for at least two consecutive years (French, 2007). Figure 2.1 shows a typical cross section of a periglacial environment. On top of the permafrost a seasonally unfrozen layer occurs, the active layer. The active layer thickness varies between a few tens of centimeters to several meters (Schuur et al., 2008). Polar or latitudinal permafrost can reach depths of 1500 m (Washburn, 1979). Between 12.8 to 17.8% of the exposed land area on the Northern Hemisphere is underlain by permafrost (Zhang et al., 2000). The extent and distribution of permafrost on the Northern Hemisphere is shown in Figure 2.2. The distribution can be continuous (90-100% coverage), discontinuous (50-90%), sporadic (10-50%) or isolated (0-10%). Permafrost occurrence can be predicted by looking at the temperatures at the bottom of the winter snow pack: if the temperature is lower than -3°C, permafrost is probable (French, 2007). Due to a snow or vegetation cover, the mean annual ground surface temperature (MAGST) exceeds the mean annual air temperature (MAAT), which is called the surface offset. The temperature profile of permafrost shows seasonal variation down to the depth of zero annual amplitude. Below this depth, the temperature profile is characterized by a geothermal gradient. The permafrost base is located at the point where the mean annual temperature is above 0°C. Epigenetic permafrost occurs when ground is exposed to perennial freezing after formation (downward freezing). Syngenetic permafrost is formed during sedimentation; the formation happens at the same time as deposition of soil material takes place (French, 2007). Hereby, both the ground surface and the permafrost table move upward (Shur and Jorgenson, 1998).

Ground ice exists in the form of ice wedges, pore ice, segregated ice or intrusive ice. Ice wedges result from thermal contraction cracking and infill of water in repeated freeze- and thaw-cycles (French, 2007). They form networks that express as superficial polygonal patterns. These patterns are one of the most well-recognized and widespread periglacial features. Pore ice is formed by the in situ freezing of pore water. Segregated ice expresses as ice layers or lenses which can be from a few millimeters to tens of meters thick. Intrusive ice results from the intrusion of water under soil water pressure and occurs as sill or pingo ice (French, 2007). Ground ice can take up to 80% of soil volume (Schuur et al., 2008) like in yedoma deposits (Schirrmeister et al., 2013).

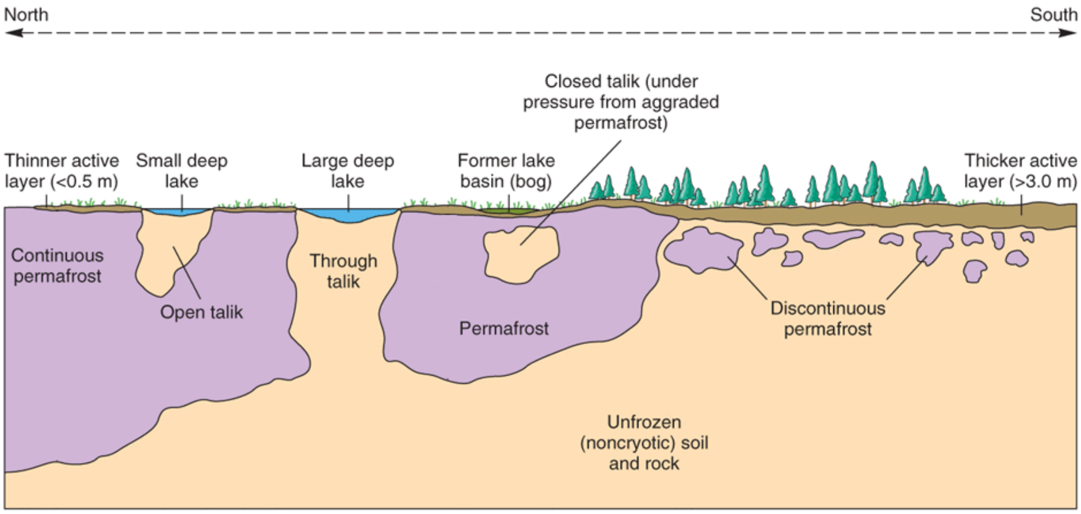

Figure 2.1: Cross section of periglacial environment. From Christophersen (2009).

Figure 2.2: Permafrost extent and distribution on the Northern Hemisphere. From Brown et al. (1998).

2.2 Permafrost degradation and thermokarst

Permafrost degradation occurs when mean ground temperatures allow thawing. Top-down thawing starts when the mean annual temperature at the surface of the permafrost exceeds the melting point (in salty soil, the melting point of water is below 0°C). Ground cover is very important in this temperature balance: both snow and vegetation cover 'protect' the permafrost, as they insulate the ground from the cold air. Hence, the lack or removal of vegetation and organic soil, for example by forest fires, typically leads to degradation (Shur and Jorgenson, 2007). Thus, local permafrost thaw is caused by a change of the thermal regime. Active layer thickening is an important gradual process in early permafrost thaw. More rapid thaw processes are the development of thermokarst lakes, thermal erosion and abrasion by river and the ocean (Schuur et al., 2008).

Thermokarst is the process of surface subsidence caused by the change of the thermal regime. One can distinguish between thermal erosion and thermokarst subsidence. The first is a result of surface water erosion and is typically visible by the formation of rills and gullies by surface runoff. Thermokarst subsidence is a result of a loss of water by thawing of ground ice, after which the water is evaporated or drained (French, 2007). This is often caused by the development of thaw lakes (i.e. thermokarst lakes). These lakes often form by coalescence of water pools that arise after the degradation of ice wedges (Figure 2.3a-b). A body of unfrozen ground – a talik – forms underneath the lake. When water depth exceeds winter ice thickness, the lake and the talik deepen (Grosse et al., 2013) which is shown in Figure 2.3c. Apart from vertical growth, thermokarst lakes undergo radial expansion (Hopkins and Kidd, 1988; Jones et al., 2012). Lateral expansion rates are generally in the range of tens of centimeters to a meter per year (Burn and Smith, 1990; Jones et al., 2011; Lenz et al., 2016c). Eventually, thermokarst lakes show shrinkage and gradual or sudden drainage (Figure 2.3d). Different processes can lead to the drainage such as infilling by sedimentation or peat growth, horizontal outflow through thermal erosion of ice wedge networks or coastal erosion, or vertical outflow through open taliks (Burn and Smith, 1990; Lenz et al., 2016a). Following drainage, the basins can become vegetated after 5 to 10 years and begin to accumulate peat after 20 to 100 years (Jones et al., 2012). After a certain time, depending on climatic factors and the initial depth and age of the former lake, the talik can refreeze again (Jones et al., 2012, Lenz et al., 2016c). Permafrost degradation and the associated melting of ground ice, lead to changes in topography and ecosystem dynamics. In early stages of thermokarst lake formation, organic carbon is mainly released in anoxic conditions as the greenhouse gas CH_4 (Figure 2.3b). In later stages of thermokarst lake formation and after drainage, however, the basins can act as a net carbon sink by CO_2 uptake in aquatic productivity or by peat accumulation (Figure 2.3c-d). After drainage, the sediments and stored carbon can refreeze and reform permafrost (Walter Anthony et al., 2014), whereby the organic matter is locked.

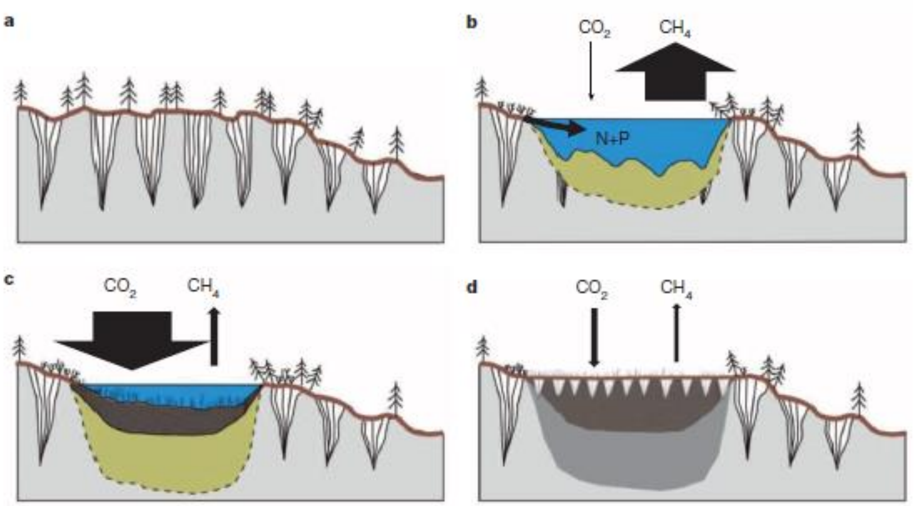

Figure 2.3: Thermokarst lake development and drainage. a) Landscape with massive ice wedges, b) lake expansion with dominated CH_4 emission, c) partially drained lake with dominated CO_2 uptake by aquatic productivity, d) complete drainage and refreezing of carbon in sediments. From Walter Anthony et al. (2014).

Thermokarst lake development is a cycle which can repeat over and over again, following the main phases expressed in Figure 2.3. The landscape units studied in this research are yedoma deposits (Figure 2.3a), thermokarst lake sediments (Figure 2.3b-c) and drained thermokarst lake basins (Figure 2.3d).

2.3 Yedoma

Especially prone to thermokarst development are yedoma permafrost deposits. Yedoma is Late Pleistocene ice-rich and silty syngenetic permafrost (Kanevskiy et al., 2011). The name translates from the Russian word е дома which refers to a mound which rises a several dozen meters above surrounding terrain. Also, the term Ice Complex has been used extensively, indicating the high ice content of the deposits. Large parts of Alaska and Siberia are covered by these deposits (Strauss et al., 2015), both Arctic and boreal regions (Kanevskiy et al., 2011). Figure 2.4 shows the general distribution of yedoma. Yedoma formation started around > 55 ka BP and continued to 12 ka BP (Schirrmeister et al., 2013, Strauss et al., 2015; Shur et al., 2012).

Table 2.1 shows the Quaternary stratigraphic terminology used, including the marine-isotope (MIS) time scale. Yedoma formation started during the Early Wisconsinan Stadial (MIS4). This stage is characterized by harsh climate conditions and severe soil erosion took place. The next stage is the Middle Wisconsinan Interstadial (MIS3) which had a warmer and moister climate than before (Andreev et al., 2011). However, regional climate differences existed during the MIS3 in Siberia which allowed yedoma deposition to continue in drier conditions (Wetterich et al., 2014). Deposition continued in the Late Wisconsinan (MIS2) which was characterized by a very cold and dry climate (Andreev et al., 2011).

Table 2.1. Quaternary stratigraphic terminology. From Andreev et al. (2011).

Epoch	**West European nomenclature**	**North American nomenclature**	**Marine Isotope Stages (MIS)**	**Age [ka BP]**
Holocene			1	ca. 10.3-0
	Late Weichselian	Late Wisconsinan	2	ca. 30-10.3
Late	Middle Weichselian	Middle Wisconsinan	3/4	ca. 50-30
Pleistocene	Early Weichselian	Early Wisconsinan	4/5a-d	ca. 110-50
	Eemian	Sangamonian	5e	ca. 130-115

Yedoma deposition generally includes repeated cycles of accumulation of snow together with plant and mineral material in the form of hills, and transportation by proluvial, fluvial and aeolian processes. The combination of periglacial transport processes typically results in a multimodal grain size distribution of the deposited sediments (Schirrmeister et al., 2008). It forms in poorly drained landscapes in which the permafrost table is close to the surface (Schirrmeister et al., 2013). The thickness of the deposits generally reaches 10 to 30 m but can locally reach 50 m (Sher, 1997; Shur et al., 2012). For comparison, syngenetic permafrost that was formed in the Holocene only reaches a thickness of several meters (Shur and Jorgenson, 1998). Yedoma is penetrated by large syngenetic ice wedges up to 5-8 m wide and 30-40 m high (Sher, 1997). Wedge ice can occupy up to 50% of the volume (Kanevskiy et al., 2011; Ulrich et al., 2014). Adding up ice wedge-ice, pore ice and segregated ice, the volumetric ice content of yedoma is in the range between 70 and 80% (Schirrmeister et al., 2008; Ulrich et al., 2014; Strauss et al., 2013; Shur et al., 2012).

Degradation of yedoma has occurred during the transition from a cold and dry climate during the Late Pleistocene to a warmer and wetter climate in the Holocene. It is estimated that ~70% of the yedoma region is affected by degradation (Strauss et al., 2013). Yedoma in Eastern Europe has vanished completely. One of the main forms of yedoma degradation is thermokarst lake formation. Thermokarst lakes in yedoma areas are on average considerably deeper than non-yedoma thermokarst lakes (10-20 m compared to 1-3 m, respectively) due to the presence of large ice wedges in the yedoma (Morgenstern et al., 2011; Shur et al., 2012). Yedoma is an important carbon reservoir: typical total organic carbon values are 2-5 weight percent (Zimov et al., 2006b; Schirrmeister et al., 2008). More importantly, the organic carbon stored in yedoma, previously freeze-locked, is highly decomposable (Strauss et al., 2013; Vonk et al., 2013). Therefore, thawing of yedoma can be an important source of greenhouse gas emissions. And thawing of ground with such high ice content leads deep ground subsidence. In order to improve the estimates of the amount of OC stored in yedoma, the spatial coverage of yedoma deposits needs to be improved (Vonk et al., 2013). Furthermore, coastal erosion is of big importance for yedoma degradation, as a large share of the deposits is located at the coast (Figure 2.4). With higher rates of erosion, the permafrost soils can be rapidly degraded.

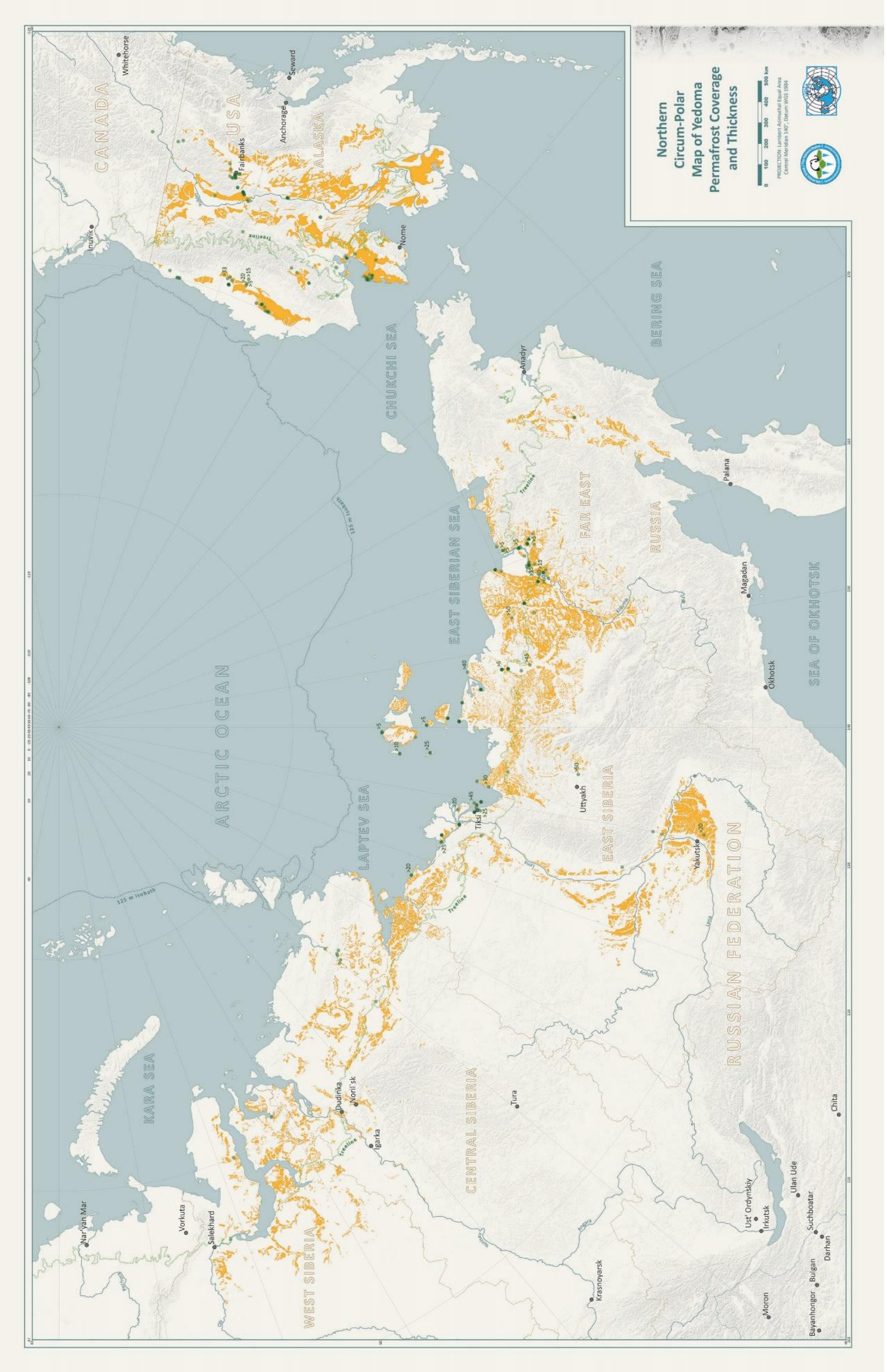

Figure 2.4: Distribution of yedoma in Siberia and Alaska (in orange). From Strauss et al. (2016)

2.4 Regional setting: Baldwin Peninsula

The study area of Baldwin Peninsula is part of the former landmass Beringia that remained unglaciated during the Late Pleistocene and connected Siberia (from the Taymyr Peninsula) to Alaska and Yukon (Canada) during sea-level low stands in the Late Pleistocene (Schirrmeister et al., 2013). The Baldwin Peninsula is located in an arm of the Kotzebue Sound in northwest Alaska (66°40'N, 162°15'W). Figure 2.5 shows the study sites near the Cape Blossom. The study area is located in the continuous permafrost zone, but is close to the transition of continuous to discontinuous permafrost. A large part of the peninsula is penetrated by ice wedges (Figure 2.6a and b).

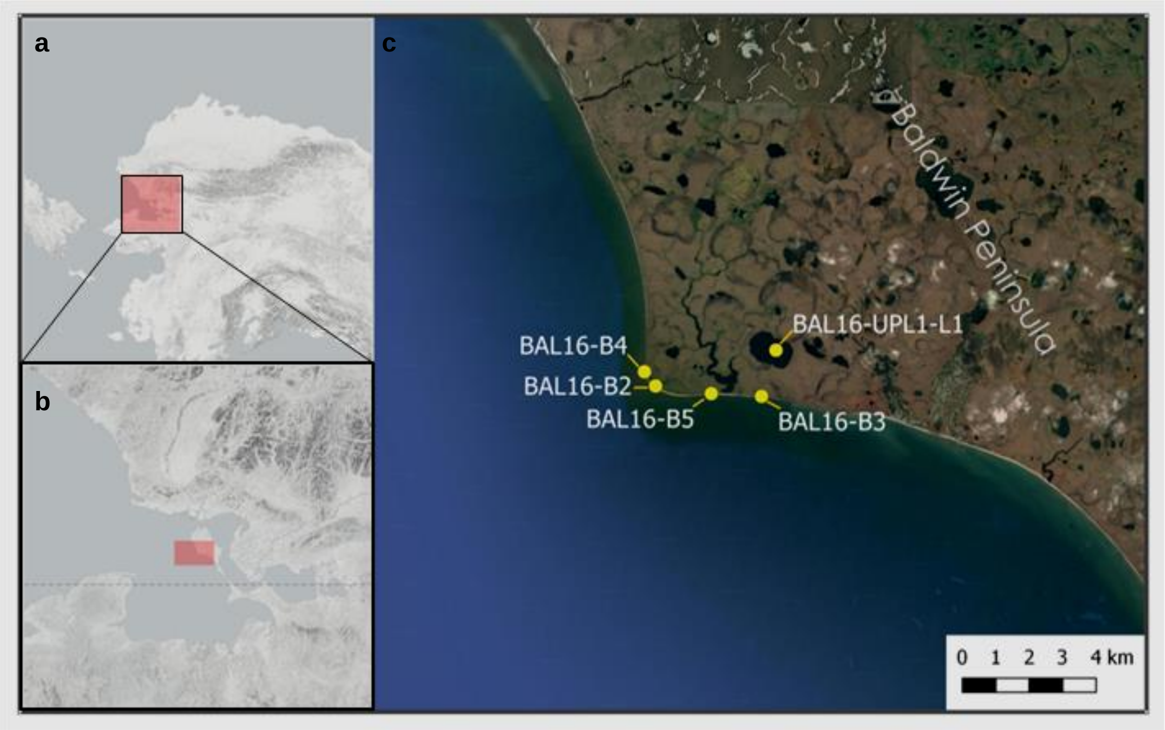

Figure 2.5: Map of study area. Overview map of Alaska (a) indicating in red the Kotzebue area. b) Detail map indicating in red the Baldwin Peninsula (c). Study sites are marked with yellow dots. From Google Earth and CartoDB. Map by I. Nitze.

The Baldwin Peninsula lower stratigraphic units are part of a middle Pleistocene push-moraine complex composed of marine, fluvial and glacial sediments (Huston et al., 1990). Marine deposits were exposed during a transgression, after which large glaciers from the Kobuk, Noatak and Selawik river valley overrode the sediments into a large push moraine. Distinct silt, gravel and diamicton members were deposited on top of the glacially folded sediments (Huston et al., 1990; Pushkar et al., 1999). On top of the moraine, the landscape consists of ice rich Late Pleistocene and Holocene deposits. Yedoma developed by the deposition of fine grained deposits originating from the floodplains from the river that now composes the Noatak and Kobuk Rivers (Wetterich et al., 2012). In the field, the presence of yedoma was confirmed at Cape Blossom (Lenz et al., in prep). The climate nowadays is subarctic with average annual precipitation of 280 mm and a MAAT of -5.15°C (US Climate Data, 2017).

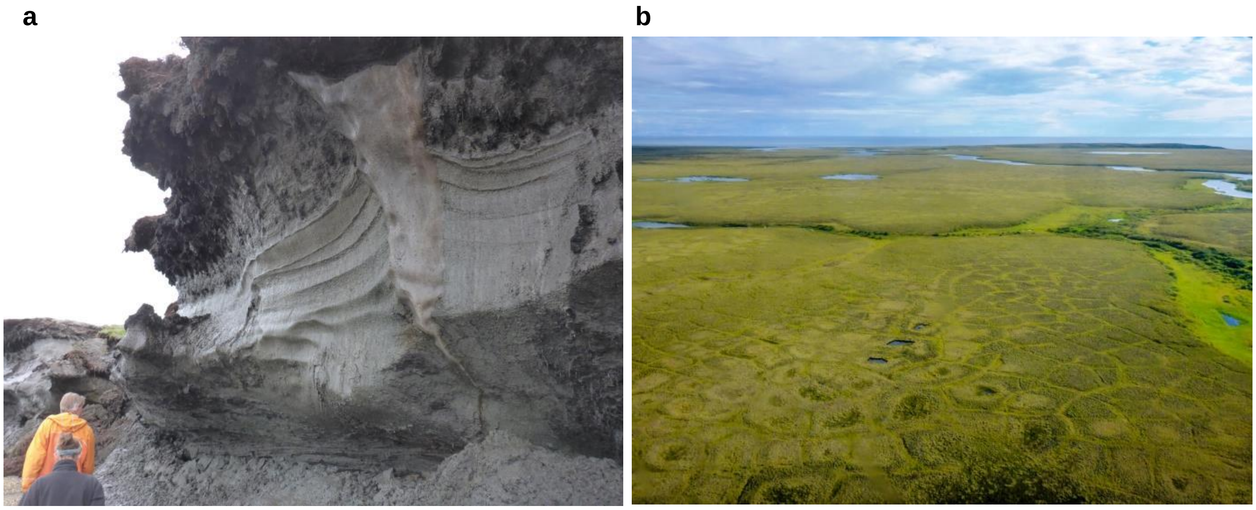

Figure 2.6: Field impressions. a) Ice wedge in coastal bluff near BAL16-B3 (66.729842°N, 162.419372°W; Photo by J. Strauss). b) Ice wedge field north of BAL16-UPL1-L1 (66.75795°, 162.423508°W; Photo by J. Lenz).

3. Methods

This study involves the following methodological parts: fieldwork, laboratory analyses, statistical analysis and remote sensing.

3.1 Fieldwork

Fieldwork was performed as part of the European Research Council (ERC) funded PETA-CARB Project (Rapid Permafrost Thaw in a Warming Arctic and Impacts on the Soil Organic Carbon Pool; 2013-2018) led by Guido Grosse. The sediment samples (Table 3.1) were retrieved during the PETA-CARB Expedition West Alaska in August 2016 (Expedition report by Lenz et al., prep). Two drained thermokarst lake basin (DTLB) exposures were sampled in vertical transects (BAL16-B3 and BAL16-B4) as well as a yedoma exposure (BAL16-B2) using a handheld power drill (ø 57 mm). A third DTLB exposure was sampled using a knife (BAL16-B5). The samples were stored in separate plastic bags, labeled and grouped per study site. They were kept frozen during and after transportation. A 34 cm long sediment core was taken from a shallow thermokarst lake (135 m deep at core site, BAL16-UPL1-L1). A piston corer operated with extension rods was used with a PVC tube (ø 60 mm). The core was kept cool and stored after transport at 4°C until it was opened at AWI Potsdam. Figure 2.5 shows the study sites.

Table 3.1: Overview of study sites of yedoma exposure, drained thermokarst lake basin (DTLB) exposures and thermokarst lake sediments.

Sample ID	Landscape unit	Coordinates	Samples
BAL16-B2	Yedoma exposure	66.73262°N, 162.49450°W	18 samples
BAL16-B3	DTLB exposure 1	66.72987°N, 162.42284°W	9 samples
BAL16-B4	DTLB exposure 2	66.73644°N, 162.50208°W	31 samples
BAL16-B5	DTLB exposure 3	66.73060°N, 162.45685°W	4 samples
BAL16-UPL1-L1	Thermokarst lake sediments	66.74220°N, 162.41310°W	34 cm long sediment core, 9 subsamples
Total			**71 samples**

3.2 Laboratory analyses

Figure 3.1 shows the flowchart of the laboratory methods. The geochronology and sedimentology were used to answer the first objective of this study concerning the sediments and the depositional environment. The biogeochemistry and biomarkers were analysed to answer the second objective concerning the organic carbon pools. The third objective concerning the stratigraphical differences was answered by taking into account all different proxies.

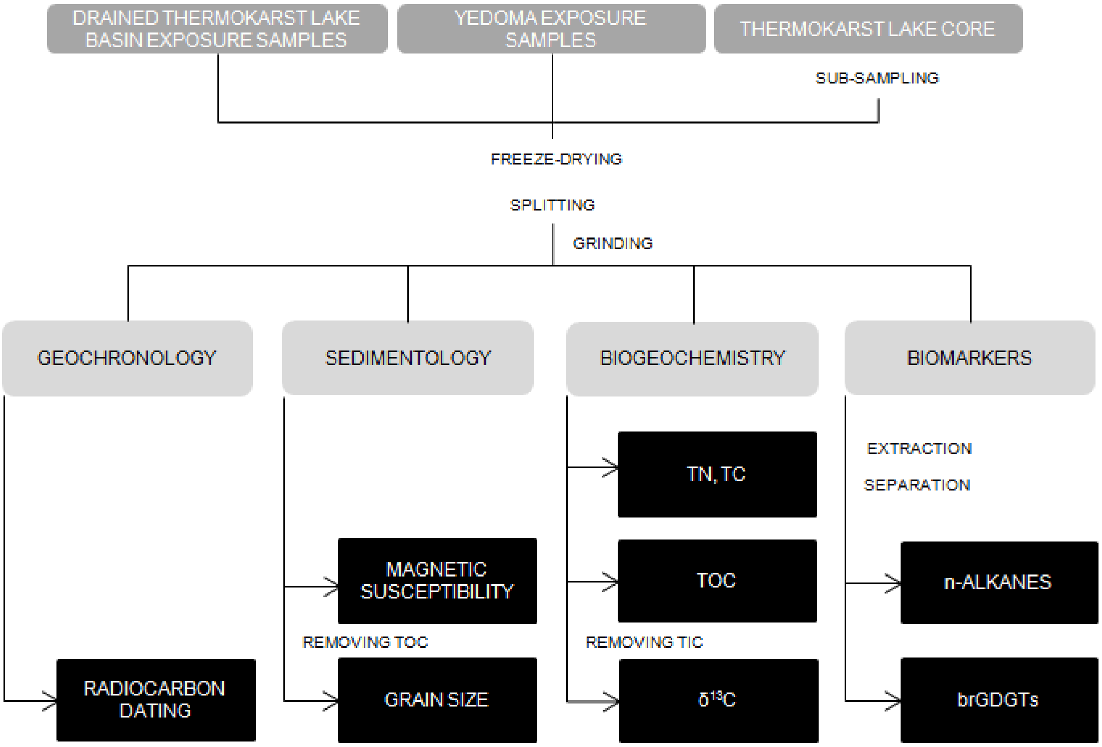

Figure 3.1: Flow chart of laboratory analyses: geochronology, sedimentology, biogeochemistry and biomarkers.

The exposure samples (BAL16-B2 to BAL16-B5) were freeze-dried (frozen at -30°C and dried under vacuum). Then they were homogenized and split into three parts for sedimentological analyses and radiocarbon dating, biogeochemistry and biomarker analyses. The biogeochemistry samples were ground in agate beakers (Planetary Mill Pulverisette 5, Fritsch). The samples for biomarker analysis were placed in glass tubes that were cleaned by heating (> 500°C) and with isopropanol. Before and after thawing and drying, all samples were weighed to calculate ice content and bulk density.

The thermokarst lake core (BAL16-UPL1-L1) was split into halves by sawing the plastic tube open and cutting the sediment with a nylon string. The 'archive half' was used for non-destructive analyses and the 'working half' was used for destructive analyses. After cleaning the sediment surface, the core profile was described visually and a high-resolution photograph was taken from the archive half at the German Research Center for Geosciences (GFZ) in Potsdam. Also, the magnetic susceptibility was measured in a non-destructive analysis on the archive halve at the GFZ. The working half was subsampled for biogeochemistry and radiocarbon dating. Nine samples of 6 cm^3 were taken in an interval of 3-5 cm and stored in 12.5 ml sample containers and freeze-dried. The samples were weighted before and after freeze-drying to calculate water content and bulk density. The samples for biogeochemistry analyses were ground.

3.2.1 Geochronology

Radiocarbon dating is based on the differences between the $^{14}C/^{12}C$ ratio in the atmosphere and the organic matter. The atmospheric ratio is assumed to be constant. After death of a living organism, the unstable ^{14}C decays into ^{14}N with a constant rate with a half-life (time it takes for half of the substance to decay) of 5370±40 year. This causes a decrease in the $^{14}C/^{12}C$ ratio. When the current ratio is compared to the known original ratio, the time since the death of the organism can be calculated. Radiocarbon dating is limited to samples older than 50 ka BP. Due to changes in the production rate (changes in the cosmic-ray flux), and the carbon cycle, the radiocarbon concentration in the atmosphere varies over time. Therefore, a calibration of the obtained ages is required (Reimer et al., 2013).

Six samples from yedoma exposure BAL16-B2, seven from DTLB exposure BAL16-B4 and two from thermokarst lake core BAL16-UPL1-1 were selected for radiocarbon dating. The samples were wet-sieved to remove small material that cannot be used for dating, after which they were dried in the drying cabinet at 50°C. Fine samples were dried as bulk and not further treated. The sieved samples were picked for plant macrofossils, such as branches and bark. The samples were sent to the external lab Radiocarbon Laboratory Poznan for radiocarbon dating using the technique of accelerator mass spectrometry (AMS). The radiocarbon ages were then calibrated using the CALIB 7.1 software and the IntCal13 calibration curve (Stuiver et al., 2017) and expressed as calibrated kilo years before present (cal ka BP).

3.2.2 Magnetic susceptibility

The magnetic susceptibility of a sample is a function of the concentration and type of magnetic minerals (Begét et al., 1990). Therefore, different sediment layers with different mineral composition can be distinguished. Also, the magnetic susceptibility can be an indication for input of allochthonous material into lakes (Thompson et al., 1975). The method for measuring this quantity is based on magnetic induction and the detection of magnetization of the matter. Sediments rich in diamagnetic components – such as organic matter – show a negative bulk magnetic susceptibility (Lascu, 2009). Differences within the profiles will be described.

The magnetic susceptibility of the exposure samples (BAL16-B2 to BAL16-B5) was measured using the Bartington MS2B Dual Frequency Sensor. Both low and high frequencies were measured at least 3 times of which an average was calculated. Further on, the low frequency measurements are used. Then, the measurements were divided by the bulk density which gives the mass-specific magnetic susceptibility. The unit is [10^{-8} m^3 kg^{-1}] but is referred to as ‘SI’ (international system of units).

The magnetic susceptibility of the lake core (BAL16-UPL1-L1) was measured at the GFZ using a split-core logger (Bartington MS2E sensor) for a non-destructive analysis. The core was covered with plastic so that the sediment surface could be followed without contamination. The core was then analyzed in intervals of 1 mm. This type of analyses does not include the density of the material, so that the obtained values are unit less (although in the scale of 10^{-6}), but the values are reported as 'SI' (note: the absolute values should not be compared to those of the mass-specific values).

3.2.3 Grain size

The analysis of grain size is important in identifying the origin of deposits. The grain size distributions of the sediments can give insights into the medium of transportation, as well as the depositional mechanism.

Grain size was analyzed for the exposure samples (BAL16-B2 to BAL16-B5). In order to only measure the clastic material, OM was removed from the samples by treating the samples with hydrogen peroxide (H_2O_2). For this, about 10 ml of sample material was weighed into 400 ml beakers to which 100 ml of 3% H_2O_2 and 4 drops of ammonia were added. The beakers were then placed on a shaker at 60°C for 2-3 weeks. Five times a week, the beakers were cleaned and 10 ml of H_2O_2 was added (and later 20 ml when the reaction was less strong). The pH was kept between 6 and 8 by adding ammonia or acetic acid to allow an optimal reaction. After the complete removal of the organic material, the samples were washed with about one liter of purified water to remove the H_2O_2. The samples were then centrifuged (Cryofuge 8500 i for 10 minutes at 5050 RPM, 20°C; Multifuge 3-S Heraeus 2-3 times for 15 minutes at 4000 RPM) and freeze-dried. The samples were manually homogenized and about 1 gram was weighed into 250 ml plastic bottles and a spoon spatula of dispersing agent (tetrasodium pyrophosphate, $Na_4P_2O_7$) was added. The bottles were filled with an ammonia solution (10 ml NH_4OH in 100 liter of water) and placed in an overhead shaker overnight. As a last step before measuring, the samples were split into 8 homogeneous samples to enable measurement of samples with concentrations between 5-15%. The material was hereby also sieved for > 1 mm to avoid damage to the laser. Inorganic particles > 1mm were weighed and if the residue was significant compared to the sample, it was included in the distribution afterwards. The grain size was analyzed with the Malvern Mastersizer 3000 laser. The device cleans automatically and measures background scatter. After a sample is inserted into the dispersion unit, it is channeled through the device to the measurement cell. Here it is exposed to a red laser and blue led (633 nm and 470 nm), of which the scatter is measured by the detectors. The average is calculated of three measurements per split sample (standard deviation <10%).

Grain size statistics are calculated using the software GRADISTAT. The grain size scaling is shown in Table 3.2. The distribution is shown using geometric scaling, in order not to put too much emphasis on coarse sediment. The average size, the spread of sizes around the average (sorting), the skewness and kurtosis were obtained (Blott and Pye, 2001).

Table 3.2: Grain size scale. From Blott and Pey (2001)

Grain size [mm] or [µm]	Descriptive terminology	
64 mm		
	Very coarse	
32		
	Coarse	
16		Gravel
	Medium	
8		
	Fine	
4		
	Very fine	
2		
	Very coarse	
1		
	Coarse	
500 µm		Sand
	Medium	
250		
	Fine	
125		
	Very fine	
63		
	Very coarse	
31		
	Coarse	
16		Silt
	Medium	
8		
	Fine	
4		
	Very fine	
2		
	Clay	

3.2.4 Total nitrogen, total carbon, total organic carbon

Total carbon (TC), total nitrogen (TN) and total organic carbon (TOC) can be used to reconstruct paleoenvironmental conditions. In this study, especially TOC and the TOC/TN ratio are important. TOC is the organic material derived from bio productivity, whereas total carbon also includes the total inorganic carbon (TIC; carbonates, bicarbonates and dissolved carbon dioxide). The TOC/TN ratio indicates the degree of decomposition of organic material, where a high value means that the organic material is well preserved (Schirrmeister et al., 2011). A high rate of mineralization is indicated by values up to 12, a moderate rate shows a ratio between 13 and 25, and a low mineralization shows higher values (Walthert et al., 2004). Also, variation in the TOC/TN ratio can describe different sources of origin. For this application, the values for TOC/TN from Meyers (1994) will be used (Figure 3.2). However, Meyers (1994) uses the atomic ratio of TOC/TN ratio. Therefore, the values from Figure 3.2 were converted by dividing by 1.167, the ratio of the atomic weight of carbon (12.001 amu) and nitrogen (14.007 amu). This leads to a typical TOC/TN ratio for aquatic algae between 3 and 9, whereas land plants show ratios of ≥ 17.

TC, TN and TOC are measured based on the principle of combustion chromatography (burning of samples to analyze concentration in the gas phase). TC and TN were determined using the Elementar Vario EL III. Five milligram of each homogenized sample was weighed into small tin capsules in duplicate. A blank capsule was measured in the beginning for background detection and a calibration run was performed before and after every fifteen samples. The percentage of total carbon and nitrogen was calculated. The determination of TOC (Elementar Vario Max C) is very similar. However, the sample is burned at a lower temperature so that the inorganic carbon is not measured. Depending on the previously measured TC values, fifteen to hundred milligrams of the samples was weighed into crucibles and placed into the machine. TN, TC and TOC are expressed in weight percentage (wt%).

3.2.5 Stable carbon isotopes

$\delta^{13}C$ is the ratio between the stable isotopes ^{12}C and ^{13}C. The analysis of these stable isotopes is important for the understanding of degradation and the degree of preservation of organic matter (Andersson et al., 2012). By combining the $\delta^{13}C$ record with the TOC/TN ratio, plant identification is possible. Figure 3.2 shows the typical atomic TOC/TN ratio (12.001:14.007) and $\delta^{13}C$ signal of lacustrine and marine algae as well as C_3 land plants. C_3 plants use basic photosynthesis, whereas C_4 plants use an intermediate step whereby 4 carbon atoms are formed (Meyers, 1997). C_4 plants do not occur in the Arctic or subarctic environments and are therefore not discussed in this study. The graph in Figure 3.2 is important in this study as it indicates the source of organic matter by distinguishing between marine and terrestrial material (on the vertical axis), and between algae and land plants, as well as the degree of degradation of the material (both on the horizontal axis) with lower TOC/TN values with degradation, as stated in section 3.2.4.

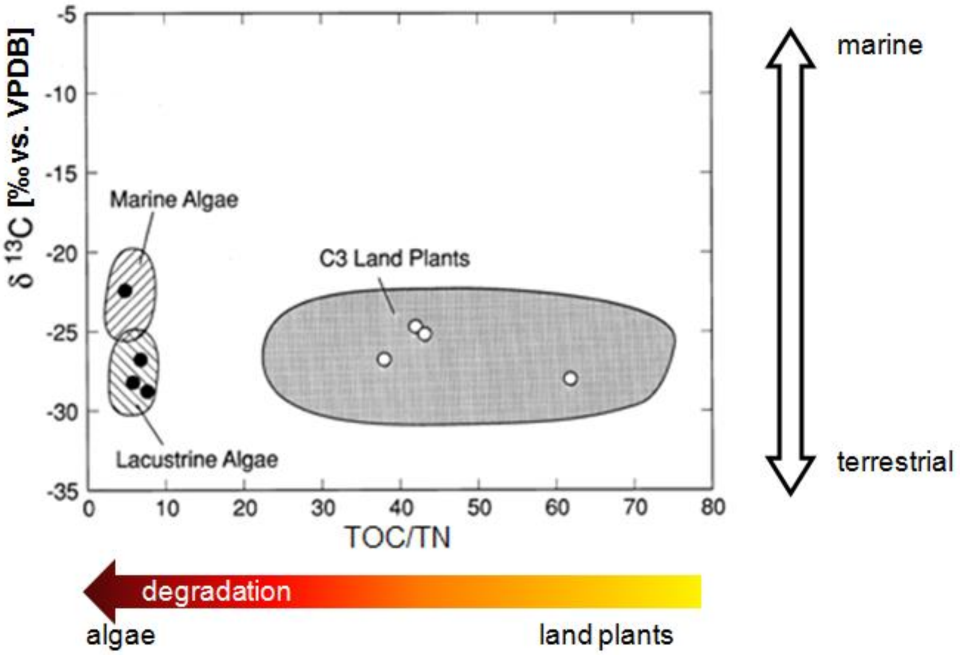

Figure 3.2: Atomic TOC/TN ratio and $\delta^{13}C$ signal indicating the source of organic matter and the degree of degradation. Adapted from Meyers (1997).

Carbonate was removed from the sediment by treating the samples with 20 ml hydrogen chloride (HCl) for three hours at 97.7°C. Purified water was added and the samples were decanted and washed three times. When the chloride content was under 500 parts per million (ppm), the samples were filtered over a glass microfiber filter (Whatman Grade GF/B, nominal particle retention of 1.0 µm). Afterwards, the residue was dried in a drying cabinet at 50°C. Dry samples were ground manually and weighed into tin capsules. The required sample weight was calculated by dividing 20 by the TOC value. A ThermoFisher Scientific Delta-V-Advantage gas mass spectrometer equipped with a FLASH elemental analyzer EA 2000 and a CONFLO IV gas mixing system was used to determine the $\delta^{13}C$. In this system, the sample is combusted at 1020°C so that the OC is transferred to CO_2, after which the isotope ratio is determined relative to a laboratory standard of known isotopic composition. Capsules for control and calibration were run in between. The unit is per mille (‰) and the ratio is compared to the standard established from the Vienna Pee Dee Belemnite (VPDB) which is taken as the standard ratio.

3.2.6 Ice content, bulk density and organic carbon content

The absolute ice content was calculated using Equation 1 and is expressed in weight percentage.

$$\text{Absolute ice content [wt\%]} = \frac{\text{wet weight} - \text{dry weight}}{\text{wet weight}} * 100 \qquad \text{Equation 1}$$

The porosity of the soil (φ) is the ratio between pore volume (equals the ice content if saturated) and the total volume. Assuming a constant mineral density (ρ_s) of $2.65*10^3$ kg m^{-3}, the bulk density (BD) [10^3 kg m^{-3}] of the exposure samples was calculated using Equation 2a. The bulk density of the unfrozen thermokarst lake sediments was measured using Equation 2b.

$$\text{BD } [10^3 \text{ kg m}^{-3}] = (\varphi - 1) * (-\rho_s) \qquad \text{Equation 2a}$$

$$\text{BD } [10^3 \text{ kg m}^{-3}] = \frac{\text{dry weight}}{\text{volume}} \qquad \text{Equation 2b}$$

The TOC values were converted to volumetric values [kg m^{-3}] using Equation 3.

$$\text{TOC}_{\text{vol}} \text{ [kg m}^{-3}] = \text{BD} * \frac{\text{TOC}_{wt\%}}{100} \qquad \text{Equation 3}$$

The total carbon budget in megaton on Baldwin Peninsula was estimated using Equation 4 (with the thickness of the deposit given in m, the coverage of the stratigraphic landscape unit in m^2, the BD in 10^3 kg m^{-3}, wedge-ice volume WIV in vol% and TOC in wt%.

$$\text{OC budget [Mt]} = \frac{\text{thickness} * \text{coverage} * \text{BD} * \frac{100 - \text{WIV}}{100} * \frac{\text{TOC}_{wt\%}}{100}}{10^6} \qquad \text{Equation 4}$$

3.2.7 Biomarkers

The molecular composition of the permafrost sediment samples was studied in more detail by analyzing lipid biomarkers. Biomarkers are complex molecular fossils that can show insights into the source of organic matter, the diagenesis of sediments and the degree of degradation. Lipid membranes are present in all living organisms. The main function is the regulation of the transport of water and solutes into or out of the cells (Peters et al., 2007). The study of the lipid biomarkers can provide more detailed information on organic inputs (Cohen, 2003). In this study, n-alkanes and branched glycerol diakyl glycerol tetraethers (brGDGTs) are studied. In total, six samples from yedoma exposure BAL16-B2 and seven from DTLB exposure BAL16-B4 were selected for lipid biomarker analysis.

3.2.7.1 n-Alkanes

n-alkanes are long-chained, single-bonded hydrocarbons. The principle sources are algae, submerged or floating vascular plants and terrestrial plants (Meyers, 2003). The absolute concentration of n-alkanes can be used to roughly estimate organic-matter quality: higher lipid concentrations indicate a better quality (Strauss et al., 2015). However, n-alkane distributions can also indicate periods of enhanced production as a result of changes in the environment (e.g. vegetation, climate).

Odd-to-even predominance of carbon chains can be described by the carbon preference index (CPI). CPI values decrease as microbial degradation occurs (Glombitza et al., 2009; Andersson et al., 2012). Therefore, degradation of OC would typically lead to an increasing trend upwards in the profile, as the lower located sediments had more time to degrade (when assuming the principle of superposition). Hence, this index is very useful in paleo-environmental studies. The CPI is calculated following the revised calculation from Marzi et al. (1993), shown in Equation 5.

$$\mathrm{CPI} = \frac{(\sum_{i=n}^{m} C_{2i+1}) + (\sum_{i=n+1}^{m+1} C_{2i+1})}{2*(\sum_{i=n+1}^{m+1} C_{2i})} \qquad n=23\text{-}33 \qquad \text{Equation 5}$$

Here, n is the starting dominating chain length divided by 2, m the ending dominating chain length divided by 2 and i the carbon number (index). The interval of C_{23}–C_{33} is used for the calculation of CPI.

The average chain length (ACL) describes the average number of carbon atoms per molecule. This parameter is based on the “higher plant” n-alkanes C_{27}, C_{29} and C_{31} (Poynter and Eglinton, 1990). Higher land plants are dominated by long-chain n-alkanes (25 to 30 carbon atoms), whereas bacteria and algae contain mainly shorter chains (15 to 20 carbon atoms) (Killops and Killops, 2009) (Figure 3.3). The formula for calculating the ACL is shown in Equation 6.

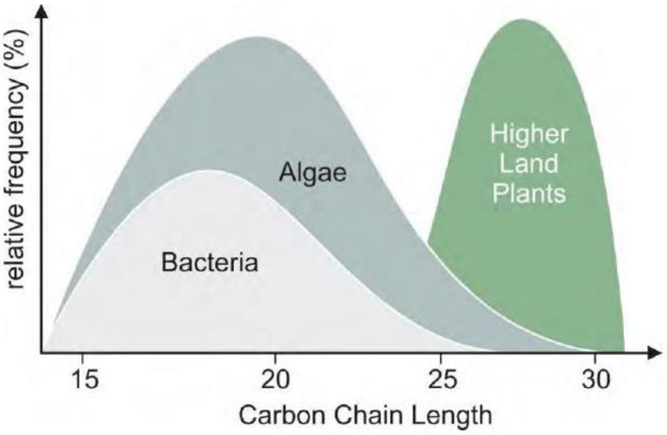

Figure 3.3: Relative frequency of n-alkane chain length in different organisms. From Strauss et al. (2015), modified from Killops and Killops (2009).

$$\mathrm{ACL} = \frac{\sum \mathrm{iC_i}}{\sum \mathrm{C_i}} \qquad n=23\text{-}33 \qquad \text{Equation 6}$$

Here, i is the carbon number (index) and C the concentration. The interval of C_{23}–C_{33} is used.

3.2.7.2 brGDGTs

Branched glycerol diakyl glycerol tetraethers (brGDGTs) are bacterial membrane lipids. They are non-volatile high molecular weight compounds. The molecular structures are shown in Figure 3.4. The structures differ in mass by the presence of cyclopentane moieties (a, b, c) and the amount of methyl branches (I, II, III). Crenarchaeol is an isoprenoid GDGT with a higher mass-to-charge ratio (m/z). brGDGTs are mainly produced in terrestrial environments, whereas crenarchaeol is most abundant in marine and lacustrine environments by archaea (Hopmans et al., 2004). The branched and isoprenoid tetaethers (BIT; Equation 7) index is the ratio between brGDGTs and crenarchaeol and was designed by Hopmans et al. (2004) as a proxy to determine the relative input of soil organic matter into a marine environment. In soils, the ratio between crenarchaeol and brGDGTs appears to be correlated to precipitation (Dirghangi et al., 2013): the BIT index is lower when precipitation is limited (mean annual precipitation < 500 mm).

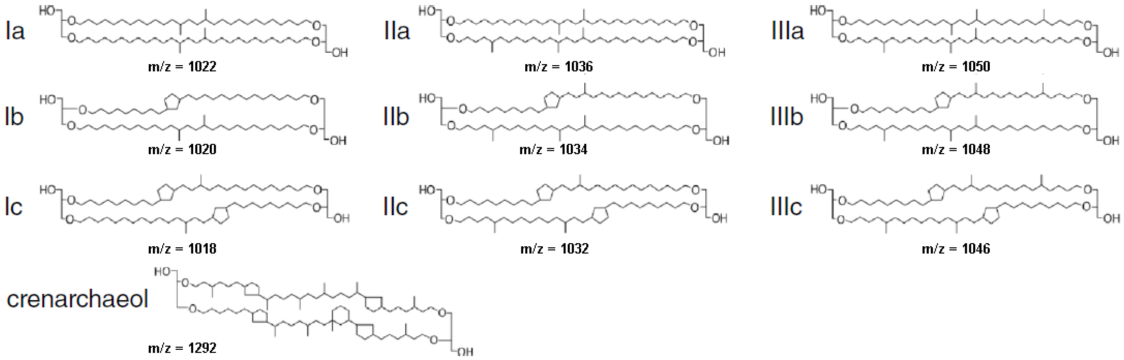

Figure 3.4: Molecular structures of brGDGTs with mass-to-charge ratio.

$$\mathrm{BIT} = \frac{\mathrm{Ia+IIa+IIIa}}{\mathrm{Ia+IIa+IIIa+crenarchaeol}} \quad \text{Equation 7}$$

The degree of cyclisation, quantified in the cyclisation of branched tetraethers (CBT) index, is related to soil pH (Equation 8).

$$\mathrm{CBT} = -\log\frac{\mathrm{Ib+IIb}}{\mathrm{Ia+IIa}} \quad \text{Equation 8}$$

The methylation of branched tetraethers (MBT; Equation 9) is primarily related to mean annual temperature (MAT). The methylation index is assumed to be positively correlated to MAT (Weijers et al., 2007). Since the MBT is also weakly related to soil pH, the two indices can be combined in to MBT-CBT proxy which enables the estimation of MAT based on brGDGT distributions in an environmental sample (Equation 10; by Weijers et al., 2007).

$$\mathrm{MBT} = \frac{\mathrm{Ia+Ib+Ic}}{\mathrm{Ia+Ib+Ic+IIa+IIb+IIc+IIIa+IIIb+IIIc}} \quad \text{Equation 9}$$

$$\mathrm{MAT} = \frac{\mathrm{MBT}-0.122-(0.187*\mathrm{CBT})}{0.020} \quad \text{Equation 10}$$

The revised MAT’ transfer function by Peterse et al. (2012) is shown in Equations 11 and 12. For the MBT’, the brGDGT-IIIb and brGDGT-IIIc are omitted from the equation.

$$\mathrm{MBT}' = \frac{\mathrm{Ia+Ib+Ic}}{\mathrm{Ia+Ib+Ic+IIa+IIb+IIc+IIIa}} \quad \text{Equation 11}$$

$$\mathrm{MAT}' = 0.81 - 5.67 * \mathrm{CBT} + 31.0 * \mathrm{MBT}' \quad \text{Equation 12}$$

3.2.7.3 Extraction and separation

The methods for the lipid biomarker analysis were adapted from Schulte et al. (2000) and Strauss et al. (2015). The accelerated solvent extractions (ASE) were performed with a Dionex 200 ASE extractor, using dichloromethane/methanol (DCM/MeOH) (99:1 v/v). About 8 g of the samples was weighed into the extraction cell bodies and placed into the machine one at a time. After 5 minutes of heating, a static phase was carried out for 20 minutes at a temperature of 75°C and a pressure of 10^6 Pa. The filtrate was concentrated in a closed cell evaporation system (TurboVap 500) at 42°C. Excess solvent was then evaporated under N_2 (gas). Four internal standards were added: 5α-androstane for the aliphatic fraction, ethylpyrene for the aromatic fraction and 5α-androstan-17-on and erucic acid for the nitrogen-, sulfur-, and oxygen-(NSO-) containing compounds. 80 µl was taken for all standards with a concentration of 100 µg/ml. As the separation system uses the solvent n-hexane, n-hexane-insoluble substances needed to be removed. This was done by filtering the samples through sodium sulfate with an excess of n-hexane (‘asphaltene’ precipitation), after which the samples were concentrated again. The total extract was separated by medium-pressure liquid chromatography (MPLC; Radke et al., 1980) into fractions of aliphatic hydrocarbons, aromatic hydrocarbons and polar heterocompounds (NSO compounds). For this, the dissolved extracts were injected into the MPLC system and were led through a column and pre-column with n-hexane. The pre-columns were filled with silica gel (thermally deactivated silica 100 63-200 µm and 200-500 µm on top with ratio ~ 7:1). Afterwards, the NSO-fraction was further separated manually into a polar and acid fraction by guiding the extracts through a KOH-impregnated silica gel column with dichloromethane.

3.2.7.4 Measurements

The n-alkanes are measured using gas chromatography/mass spectrometry (GC-MS; GC Trace GC Ultra and MS DSQ, both Thermo Electron Corporation). After injection, the sample is vaporized and mixed with the inert carrier gas helium. The GC uses the programmable temperature vaporization, for which the sample is placed in a cool chamber of 50°C and is heated to 300°C (heating rate of 10°C s^{-1}, isothermal holding time of 10 minutes). The mix is then led through a capillary column (50 m long, ø 22 mm, film thickness 0.25 µm) (Peters et al., 2007). The oven temperature was programmed from 50°C to 310°C (heating rate of 3°C $minute^{-1}$, isothermal holding time of 30 minutes). The GC was linked to the MS to enable compound identification (ionization mode at 70 eV, at 230°C). Full scan mass spectra were obtained from *m/z* 50 to 600 Da (2.5 scans s^{-1}). Using the software XCalibur, the peaks in the GC-MS total ion current chromatogram were integrated (Appendix Figure A.1). By comparing the peak area of the target compounds to the peak area of the applied internal standards, the quantification of the n-alkanes could be made.

The GDGTs analyses are performed on a Shimadzu LC-10AD HPCL (high-performance liquid chromatography) device coupled to a Finnigan TS 7000 mass spectrometer with an APCI (Atmospheric Pressure Chemical Ionization) interface. Previous studies (Weijers et al., 2007; Peterse et al., 2012) found that the polar NSO-fraction contains the brGDGTs. However, in this study, the apolar or acid fraction contained the brGDGTs. The samples were separated in a Prevail Cyano column (2.1x150 mm, 3μm; Alltech) with a precolumn filter at 30°C. The mobile phase started with 5 minutes of n-hexane (99:1 v/v), a linear gradient to 1.8% isopropanol within 40 minutes, in 1 minute to 10% isopropanol (held for 5 minutes for cleaning) and finally back to initial conditions in 1 minute (held for 16 minutes for calibration). The flow rate of the device was set to 200 μl min^{-1}. The APCI device has a corona current of 5 μA, voltage of 5 kV, the vaporizer temperature is 350°C and the capillary temperature 200°C. The source operates with nitrogen sheath gas at 60 psi and without auxiliary gas. Full mass spectra were obtained at a scan rate of 0.33 s. The integration was once again performed in XCalibur (Appendix Figure A.2 and Figure A.3), comparing the compound peaks to an Archaeol run that was run at the start and end of each measuring day.

3.3 Statistical analyses

3.3.1 Mann-Whitney-Wilcoxon test

A Mann-Whitney-Wilcoxon test was performed for testing for significant difference between two populations: yedoma exposure (BAL16-B2) and DTLB exposures (BAL16-B3 to BAL16-B5). It is a non-parametric test which means that no normal distribution is assumed, in contrast to a one-way ANOVA. Also, this test allows groups of different sizes. The null hypothesis states that the different groups are drawn from identical populations. The test statistic U is calculated according to Equation 13. Equation 14 shows the formulae for calculating the z-score.

$$U_1 = n_1 n_2 + \frac{n_1(n_1+1)}{2} - R_1 \quad \text{and} \quad U_2 = n_1 n_2 + \frac{n_2(n_2+1)}{2} - R_2 \qquad \text{Equation 13}$$

$$z = \frac{|U-\mu|-0.5}{\sigma} \qquad \text{Equation 14}$$

Here, U is the lowest of U_1 and U_2, R the rank, n the sample size, μ the mean and σ the standard deviation. The p-value is calculated using the normal cumulative distribution of the z-score (indicates how many standard deviations the score deviates from the mean). If the p-value exceeds 0.05, the null hypothesis cannot be rejected (Zaiontz, 2013).

3.3.2 Kruskal-Wallis test

A Kruskal-Wallis is designed for comparing multiple populations and was used for testing significant differences for the biogeochemistry between three groups: the yedoma exposure BAL16-B2, the DTLB exposures BAL16-B3 to BAL16-B5 and the thermokarst lake core BAL16-UPL1-L1. The test statistic H is calculated with Equation 15. All values, independent of group, are ranked. The ranks are added per group, squared and divided by total sample size.

$$H = \frac{12}{n(n+1)} \sum_{j=1}^{k} \frac{{R_j}^2}{n_j} - 3(n+1) \qquad \text{Equation 15}$$

Here, k is the number of groups, n_j the size of the j^{th} group, R_j the rank sum for the j^{th} group and n is the total sample size. The p-value is calculated using the right-tailed probability of the chi-squared distribution, using 2 degrees of freedom (Zaiontz, 2013).

3.4 Mapping

A map of the stratigraphic landscape units of Baldwin Peninsula was developed using a Landsat 8 satellite image (false color image with short-wave infrared, near-infrared and deep blue bands (bands 7-5-1), resolution 30 x 30 m) as well as a digital terrain model (DTM; resolution 5x5 m). Hereby, the three landscape units were identified: yedoma, DTLB and thermokarst lake deposits. The coverage of the different deposits was calculated which is required for the estimation of the organic carbon stored on the Baldwin Peninsula (Equation 4). Using a GIS-program, the different units were distinguished and digitalized. As stated before (section 2.1), thermokarst lakes and drained lake basins are relatively easy to distinguish. Yedoma deposits were identified by the specific landform: elevated areas like low flat hills with characteristic geomorphological indicators, like penetration by small deep lakes and thermokarst mound (baidzharakhs) (Kanevskiy et al., 2011).

4. Results

In section 4.1, the results are shown for each of the study sites, starting with the yedoma exposure (BAL16-B2), then the DTLB exposures (BAL16-B3, BAL16-B4 and BAL16-B5) and finally the thermokarst lake core (BAL16-UPL1-L1) (Table 3.1). The parameters are presented in graphs over depth, as well as in additional tables. Grain size values are interpreted according to Folk and Ward (1957). A summary of all cryological, sedimentological and biochemical data is given in Appendix Table A.1; the data of n-alkanes and brGDGTs are shown in Appendix Table A.2 and Table A.3, respectively. In section 4.2, the results from the statistical tests are presented. Finally, in section 4.3, the results from the land cover classification and organic carbon calculations are shown.

4.1 Sedimentary profiles

4.1.1 BAL16-B2

The yedoma site consists of a yedoma bluff of about 16 m thick on top of medium silty sediments. The obtained proxies of the yedoma exposure are presented over the depth of the complete section. However, the exposure was sampled in five different sampling zones I-V (Table 4.1). This classification is only based on spatial variation so no stratigraphical differences are implied. This distinction was made so that it is clear that the record is not continuous, but rather a compilation of the exposure. Zones I, II, III and V are shown in Figure 4.1 and zone IV in Figure 4.2: similar points in the pictures are indicated with the yellow crosses 1 and 2. Depths are measured from the cliff top. Zone III contains small ice bands (< 2 mm) and macro lenses. Zone IV is brownish-grey and ice-rich, ice bands and ice lenses are present, as well as sparse organic remains and an organic band at 1594 cm. Zone V is located in the sediments under the yedoma (not visible in the picture, hence the green arrow) and includes mega-lenses (< 30 cm long, 1-3 cm thick) with very clear ice.

Table 4.1: BAL16-B2 samples with corresponding depths in sampling zone I-V.

Sampling zone	**Sample ID**	**Depth [cm]**
I	BAL16-B2-20 to 27	620-965
II	BAL16-B2-28 to 32	1065-1142
III	BAL16-B2-33 to 39	1242-1399
IV	BAL16-B2-1 to 5	1500-1600
V	BAL16-B2-40 to 42	1700-1870

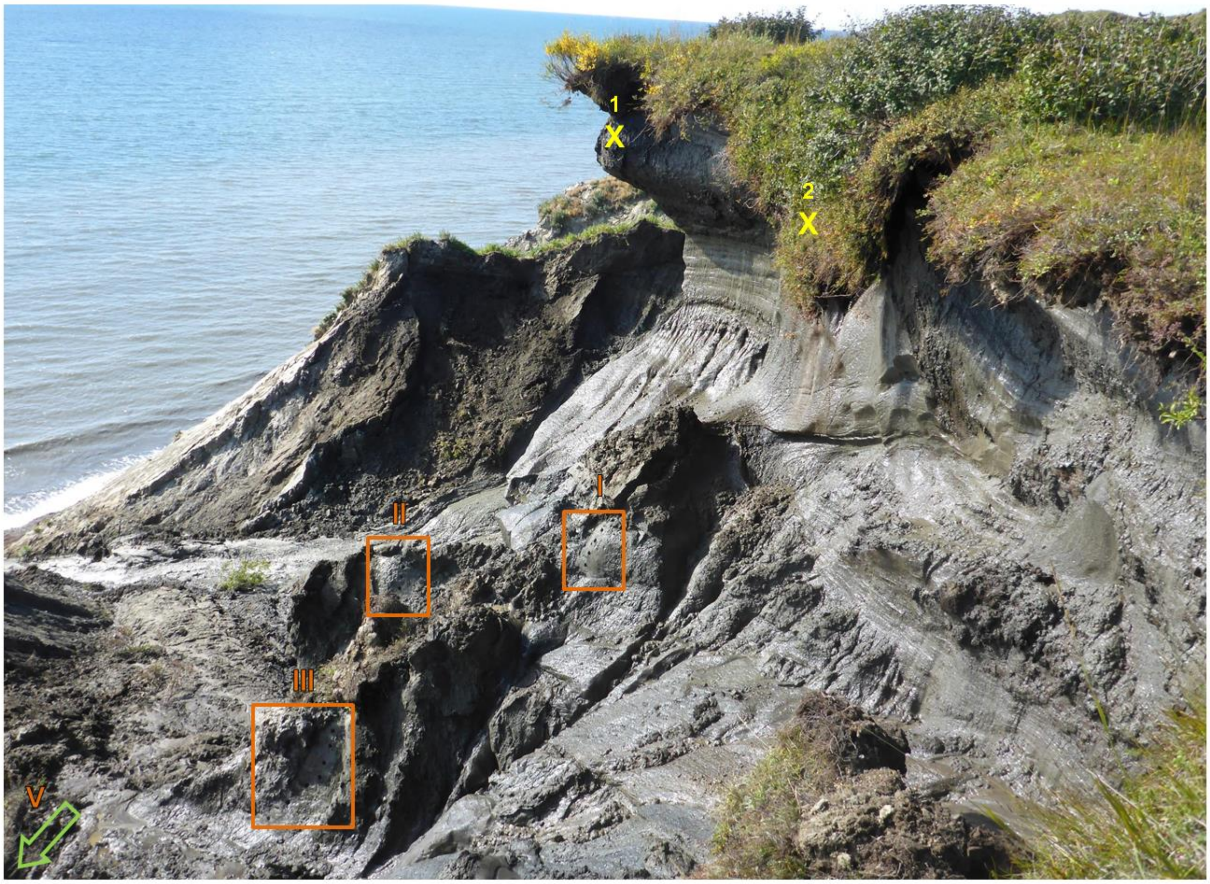

Figure 4.1: Exposure BAL16-B2 (side 1). Sampling zone I, II and III indicated with orange rectangle and zone V indicated with green arrow. Yellow crosses '1' and '2' indicate similar points in the landscape as indicated in Figure 4.2. Photo by J. Strauss.

The radiocarbon dates (Table 4.2) of the yedoma deposits range from > 50 to 10 ka BP. The samples taken at 620, 1399 and 1500 cm have infinitive ages. The sediments at 945 and 1600 cm are young (10 and 19.6 ka BP) compared to the other samples. There is no consistent age-depth trend. The cryological, sedimentological and biochemical parameters are shown in Figure 4.3. The absolute ice content varies between 35 and 70 wt% and shows most variation in the lower part. The bulk density has an average of $0.80*10^3$ kg m^{-3} and shows most variation in the bottom part up to 1100 cm with minima at 1555 cm ($0.35*10^3$ kg m^{-3}) and 1366 cm ($0.40*10^3$ kg m^{-3}). The magnetic susceptibility ranges between 26 and 86. The lower part of the exposure has more variation in the magnetic susceptibility. The TOC has an average of 1.9 wt% and shows almost no variation. The TOC value at 1065 cm is below the analytical accuracy of 0.1 and is therefore excluded from further calculations. The TOC/TN ratio is also relatively steady over the whole profile with a mean of 10.1. The $\delta^{13}C$ is in the range of -24.8 to -28.3‰ and shows minima at 1555 and 1399 cm.

Figure 4.2: Exposure BAL16-B2 (side 2) , sampling zone IV indicated with orange rectangle. b) Close-up of sampling zone IV. Yellow crosses ‘1’ and ‘2’ indicate similar points in the landscape as indicated in Figure 4.1. Person with length of 170 cm for scale. Photos by J. Strauss.

Table 4.2: Radiocarbon dates of BAL16-B2. Calibrations were performed using CALIB 7.1 software and the IntCal13 calibration curve (Stuiver et al., 2017). Poz: Poznan Radiocarbon Laboratory, Poland.

Sample ID	**Ext. ID**	**Depth**	**^{14}C ages**	**±**	**Mean cal ages 2σ (95.4 %)**	**±**	**Rounded ^{14}C ages**	**±**
		[cm]	**[a BP]**		**[a BP]**		**[cal a BP]**	
BAL16-B2-20	Poz-89527	620	> 48,000					
BAL16-B2-26	Poz-89700	945	8,890	50	10,037.5	153.5	10,000	150
BAL16-B2-31	Poz-89702	1117	40,810	1,800	44,747	3,125	44,700	3,130
BAL16-B2-39	Poz-89703	1399	> 50,000					
BAL16-B2-1	Poz-89526	1500	> 50,000					
BAL16-B2-5	Poz-89523	1600	16,200	90	19,551.5	287.5	19,600	290

The n-alkane parameters and brGDGT concentration over depth are shown in Figure 4.4 and Appendix Table A.4. The remaining brGDGT parameters are shown in Table 4.3. The absolute n-alkane concentration ranges from 545 to 1843 µg g^{-1} TOC is lowest at 945 cm and the maximum at 1117 cm. The ACL shows values between 28.8 in the bottom sample and 28.2 in the top, and a peak of 30.0 at 1117 cm. The samples are dominated by chains with a high number of carbon atoms: the dominating chain is n-C_{31} for B2-31 and n-C_{29} for the other samples (Appendix Table A.2). A mean value of 11.6 is shown for the CPI, the minimum is 9.0 (1399 cm). No clear trend over depth is seen in the n-alkane concentration or the CPI.

The brGDGT concentration is stable with an average of 448 ng g^{-1} TOC and a maximum at 1399 cm (1,277 ng g^{-1} TOC). The brGDGT concentrations 1117 cm were too low (within noise) for integration. All samples are dominated by brGDGT-II, except at 1600 cm where brGDGT-III dominates (Appendix Table A.3). as expected for terrestrial samples, the BIT index varies between 0.88 (at 1600 cm) and 1.00. MBT and MBT' show similar values with an average of 0.23 and a higher value at 1399 cm (0.39). This leads to negative mean annual temperatures for all samples down to -1.5°C except for a positive temperature at 1399 cm of 7.6°C. The MAT' shows the same trend, but about 4.5°C higher.

The profile has a unimodal grain size distribution and is dominated by coarse silt leaning towards sandy silt (Figure 4.5). A ternary diagram classifies soil texture according to combinations of clay, silt and sand percentages (Figure 4.5b). A general trend of coarsening is observed closer to the surface. The grain distribution shows poorly sorted material (mean sorting = 2.77), an excess of fines (mean skewness = -0.22) and is mesokurtic (mean kurtosis = 1.10). The samples show a unimodal distribution. The grain size distributions seem quite similar, but samples at 1870 to 1700 cm are in the finer fraction. The clay content is very stable with values around 6 vol% in the lower half of the profile up to 1300 cm and 3 vol% in the upper half. The silt content varies between 76 and 92 vol%. The sand content is lowest from the bottom to 1331 cm around 9 vol%. In the upper part, the sand content fluctuates more between 13 and 22 vol%. The mean grain size varies between 9 and 33 µm and has an average of 23 µm.

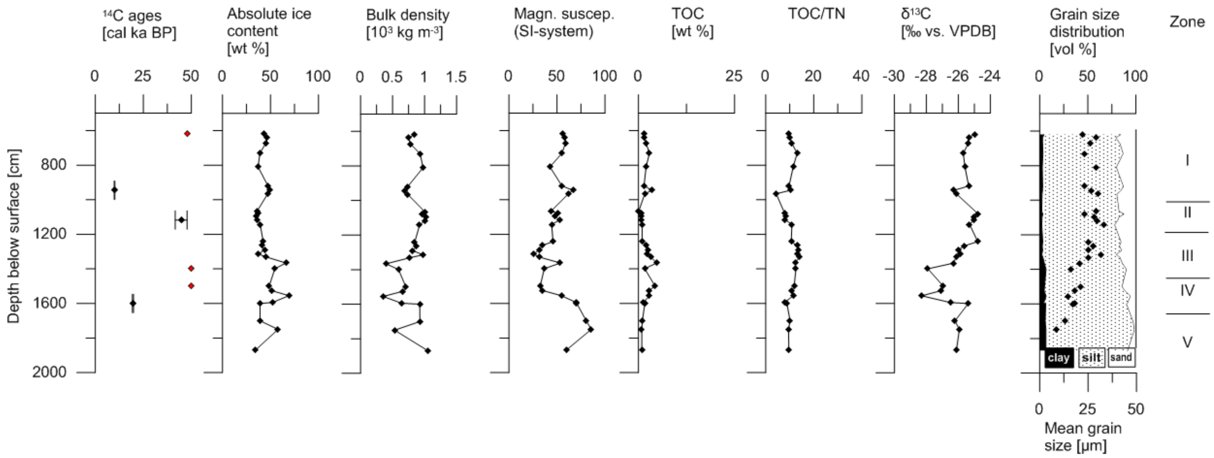

Figure 4.3: Summary of cryological, sedimentological and biochemical parameters of BAL16-B2: calibrated radiocarbon dates (infinitive ages in red), absolute ice content, bulk density, magnetic susceptibility, TOC (note: different axis), TOC/TN, $\delta^{13}C$, grain size distribution and mean grain size. The sampling zones are indicated on the right.

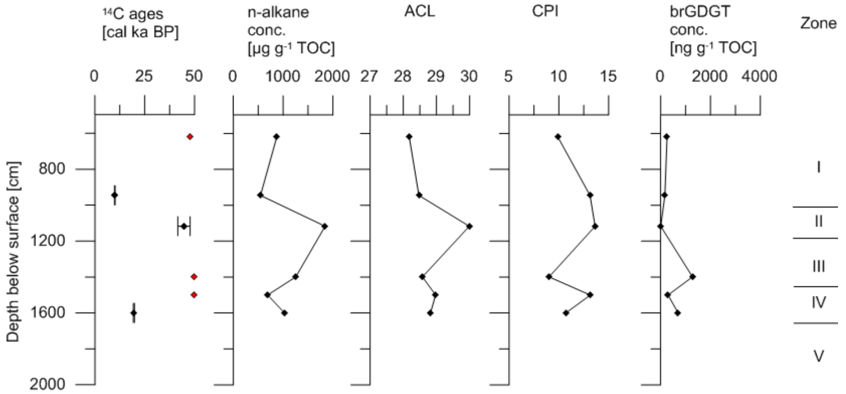

Figure 4.4: Summary of biomarker parameters of BAL16-B2: calibrated radiocarbon dates (infinitive ages in red), n-alkane concentration per g of TOC, ACL, CPI and brGDGT concentration per g of TOC. The sampling zones are indicated on the right.

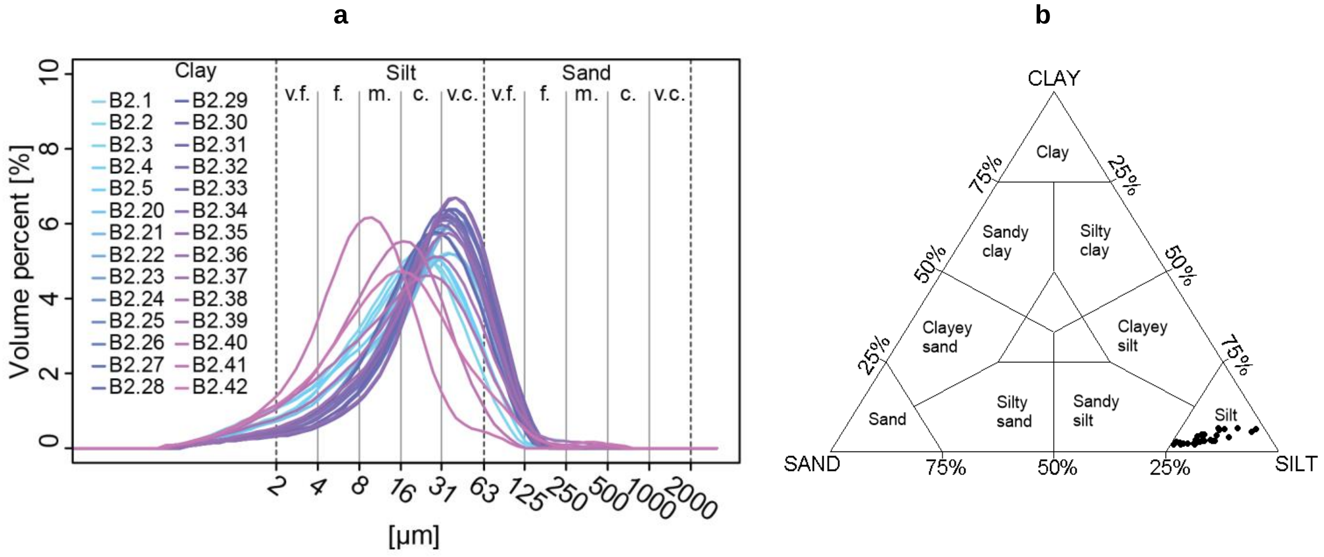

Figure 4.5: Grain size characteristics of BAL16-B2. a) Distribution and b) ternary diagram after Shepard (1954)

Table 4.3: Summary of brGDGT parameters of BAL16-B2: BIT, MBT and MAT from Weijers et al., 2007, and MBT’ and MAT’ from Peterse et al. (2012). Samples were given an external ID at GFZ.

Sample ID	Ext. ID	Depth	BIT	MBT	MAT	MBT'	MAT'
				Weijers et al. (2007)		Peterse et al. (2012)	
		[cm]			[°C]		[°C]
BAL16-B2-20	G016921	620	0.90	0.19	-1.5	0.19	3.8
BAL16-B2-26	G016922	945	0.96	0.19	-1.3	0.19	3.8
BAL16-B2-31	G016923	1117	n/a	n/a	n/a	n/a	n/a
BAL16-B2-39	G016924	1399	1.00	0.39	7.6	0.39	9.4
BAL16-B2-1	G016919	1500	0.97	0.20	-0.2	0.20	4.7
BAL16-B2-5	G016920	1600	0.88	0.18	-1.0	0.18	4.0

4.1.2 BAL16-B3

DTLB exposure BAL16-B3 (Figure 4.6) is around 4 meters high and consists mainly of peat or peat inclusions. The upper three samples (50 to 5 cm) were taken from the active layer, whereas the other samples were taken from the permafrost. The permafrost is characterized by ice bands.

Figure 4.6: Exposure BAL16-B3 with sampled spots.

The cryological, sedimentological and biochemical parameters are shown in Figure 4.7. The absolute ice content is in the range of 41 to 83 wt%. The bulk density varies between 0.18 and $0.88*10^3$ kg m^{-3} with an average of $0.50*10^3$ kg m^{-3}. The magnetic susceptibility decreases upwards in the profile from 42.7 in the bottom to 9.8 at 50 cm. An increasing trend is shown in the TOC from 1.4 to 37.3 wt%. The TOC is higher at 84 and 58 cm (39.0 wt%). The TOC/TN ratio increases from the bottom (11.6) to the top (24.8) with a peak at 84 cm (30.8). A slight decrease is shown in the $\delta^{13}C$ upwards in the profile from -27.06‰ to 27.79‰.

This profile is characterized by coarse silt to medium silt and shows a unimodal distribution (Figure 4.8a and b. The sediment is poorly sorted (mean sorting = 2.98), fine skewed (mean skewness = -0.22) and is mainly mesokurtic (mean kurtosis = 1.13). The clay content is very uniform with an average of 5 vol%. The silt content varies between 77 and 90 vol% with highest values at 200 to 170 cm and from 84 to 58 cm below the surface. The sand content shows variation between 6 and 19 vol%. The mean grain size is on average 19 µm.

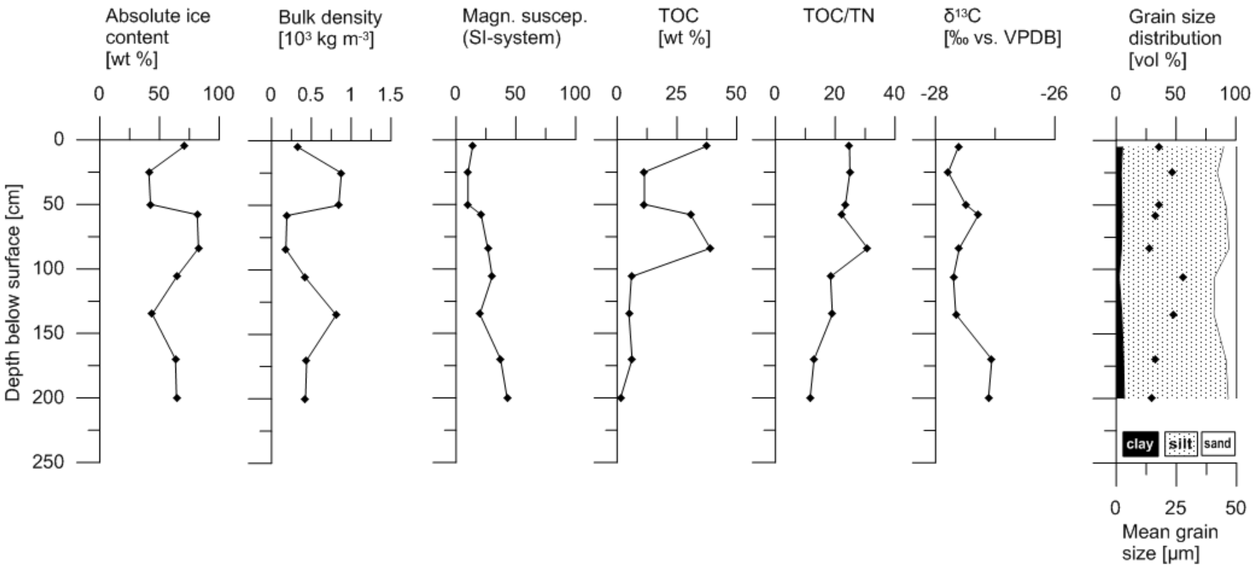

Figure 4.7: Summary of cryological, sedimentological and biochemical parameters of BAL16-B3: absolute ice content, bulk density, magnetic susceptibility, TOC, TOC/TN, δ^{13}C, grain size distribution and mean grain size.

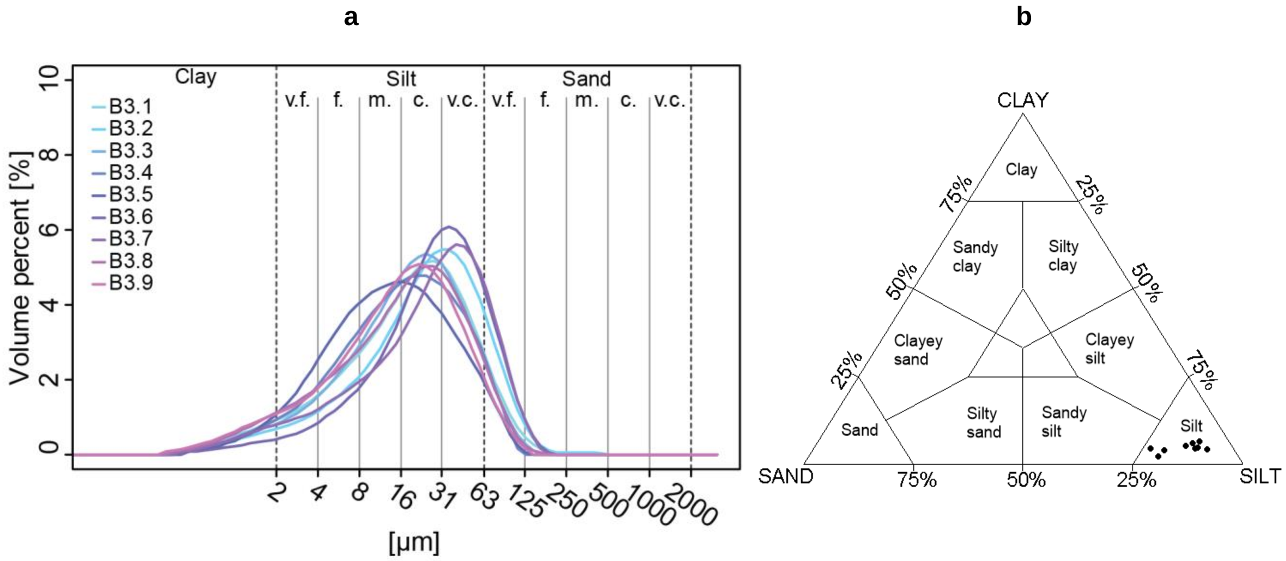

Figure 4.8 Grain size characteristics of BAL16-B3. a) Distribution and b) ternary diagram after Shepard (1954)

4.1.3 BAL16-B4

DTLB exposure BAL16-B4 (Figure 4.9) is about 8 meters high and contains different cryotextural features such as ice inclusions, lenses and veins. Also, inclusions of peat and organic remains are visible. The sediments are mostly laminated, the lower part (798 to 583 cm) contains pebble layers.

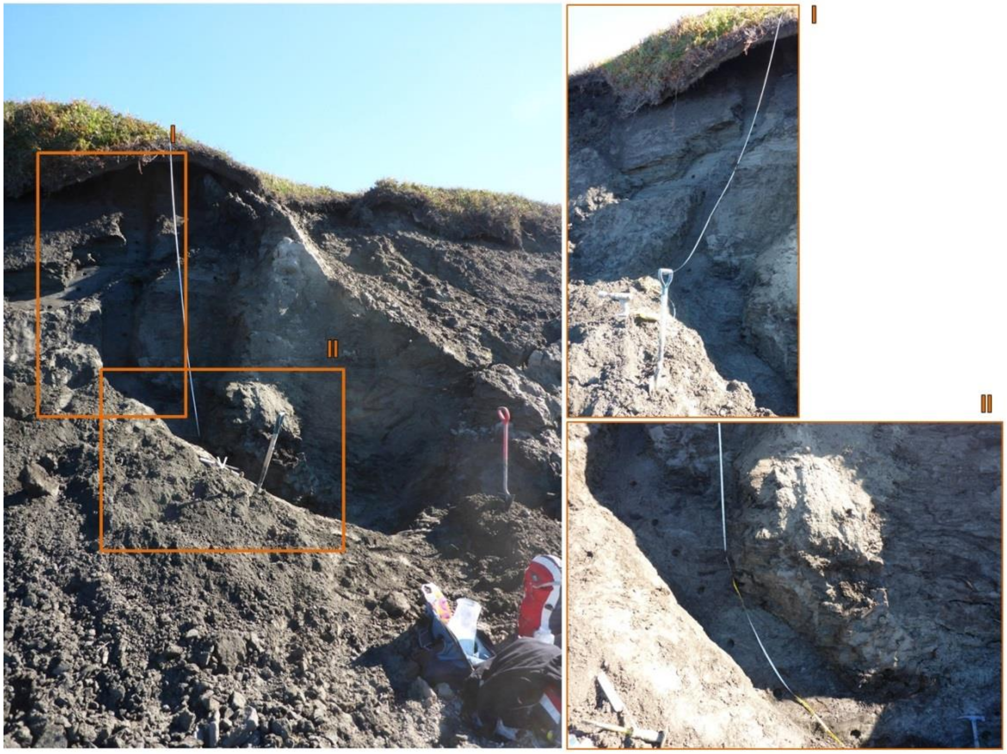

Figure 4.9: Exposure BAL16-B4 and sampling areas I and II indicated with orange rectangles (left), close up of sampling spots I and II (right).

Table 4.4: Radiocarbon dates of BAL16-B4. Calibrations were performed using CALIB 7.1 softwrare and the IntCal13 calibration curve (Stuiver et al., 2017). Poz: Poznan Radiocarbon Laboratory, Poland.

Sample ID	Ext. ID	Depth [cm]	^{14}C ages [a BP]	±	Mean cal ages 2σ (95.4%) [a BP]	±	Rounded ^{14}C ages [cal a BP]	±
BAL16-B4-2a	Poz-89704	22	105.7 [a]	0.33	239	15	240	20
BAL16-B4-4a	Poz-89705	132	1,700	30	1,590.5	46.5	1,590	50
BAL16-B4-6a	Poz-89706	166	2,125	30	2,079.5	77.5	2,080	80
BAL16-B4-14a	Poz-89707	340	42,800	1,600	46,361.5	2,967.5	46,400	3,000
BAL16-B4-18a	Poz-89708	434	> 50,000					
BAL16-B4-24a	Poz-89709	583	> 50,000					
BAL16-B4-31a	Poz-89710	788	> 50,000					

[a] Modern sample, uncertainty given in percent modern carbon (pMC).

The ages (Table 4.4) are in the range from > 50 cal ka BP to 240 cal a BP and show no age inversions. Hence, the sediments up to 340 cm are dated to be very old (>50 and 46 cal ka BP at 340 cm) and the upper part young (2,080 to 240 cal a BP). The cryological, sedimentological and biochemical parameters are shown in Figure 4.10. The absolute ice content is in the range of 27 to 74 wt%, most variation is seen in the top 3 m. The bulk density decreases upwards in the profile and ranges between 1.27 and $0.29*10^3$ kg m^{-3}. The magnetic susceptibility is highest in the bottom sample (69) and shows little variation in the rest of the profile with a mean of 24. The TOC has a mean of 6.4 wt%, higher values were measured in the interval from 250 cm to the surface than in the lower part, and a strong increase in the top two samples is shown (42.3 wt%). The sample at 798 cm has a TOC value below the analytical accuracy of 0.1 and is therefore excluded from further calculations. The TOC/TN increases to the top ranging from 11.3 at the bottom to 29.0. The $\delta^{13}C$ displays an opposite trend with higher values in the lower part (-25.8‰) and a decrease to the top (-28.7‰). Also, a sudden decrease is visible from 280 to 250 cm.

The parameters of n-alkanes and the brGDGT concentration are plotted in Figure 4.11. The parameters of brGDGTs are shown in Table 4.5. The absolute n-alkane concentration reaches its maximum of 16,444 µg g^{-1} TOC in the bottom sample. The other samples have much lower concentrations ranging from 982 to 3,355 µg g^{-1} TOC. The ACL is higher than 28 for all samples except at 583 and 430 cm (27.8 and 27.7). The CPI increases towards the top from 5.7 to 12.6.

The brGDGT concentration is around 1,000 ng g^{-1} TOC with higher concentrations at 160 and 120 cm up to 3,778 ng g^{-1} TOC. The brGDGT concentrations at 798 cm were too low for integration. The samples taken at 430, 160, 120 and 8 cm are dominated by brGDGT-II and those at 583 and 340 cm by brGDGT-III (Appendix Table A.2). A very low concentration of crenarchaeol was found at 340 cm, leading to a BIT index of 0.99. The other samples do not contain crenarchaeol so the BIT index is 1.00. The MBT and MBT' are similar and show a narrow range from 0.16 to 0.30. This results in negative MAT for all samples, with the lowest value of -10.9°C in the top sample and the highest value of -0.8°C at 160 cm. The MAT' shows a similar pattern, but about 6°C higher.

This profile is characterized by coarse to very fine sand and shows a general decreases in mean grain size to the top (Figure 4.12a and b). All samples have poorly sorted sediments (mean sorting = 2.79) and are skewed to the fine side. The upper samples (250 cm to surface) are mainly composed of coarse silt and are mesokurtic, whereas the samples below (especially in the interval of 385 to 280 cm) are coarser and the distributions are more leptokurtic. The clay content is quite uniform between 2 and 7 vol% whereas the silt content ranges between 67 and 90 vol%. The sand content is minimal from 160 to 38 cm (3 vol%) and is higher between 410 and 280 cm (maximum of 42 vol%). The mean grain size ranges between 12 and 40 µm with maxima at 768, 355 and 300 cm.

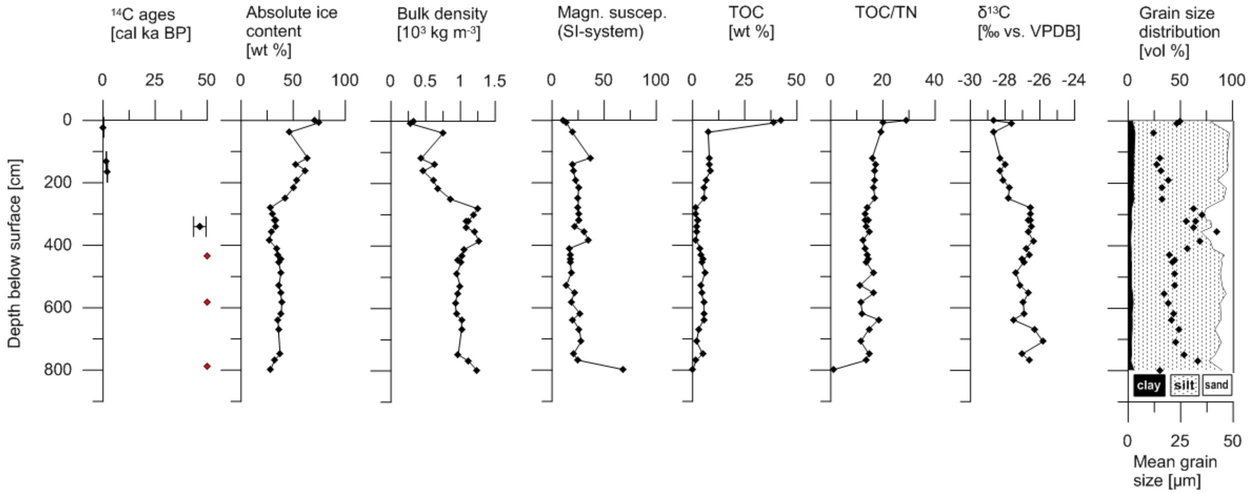

Figure 4.10: Summary of cryological, sedimentological and biochemical parameters of BAL16-B4: calibrated radiocarbon dates (infinitive ages in red), absolute ice content, bulk density, magnetic susceptibility, TOC, TOC/TN, δ^{13}C, grain size distribution and mean grain size.

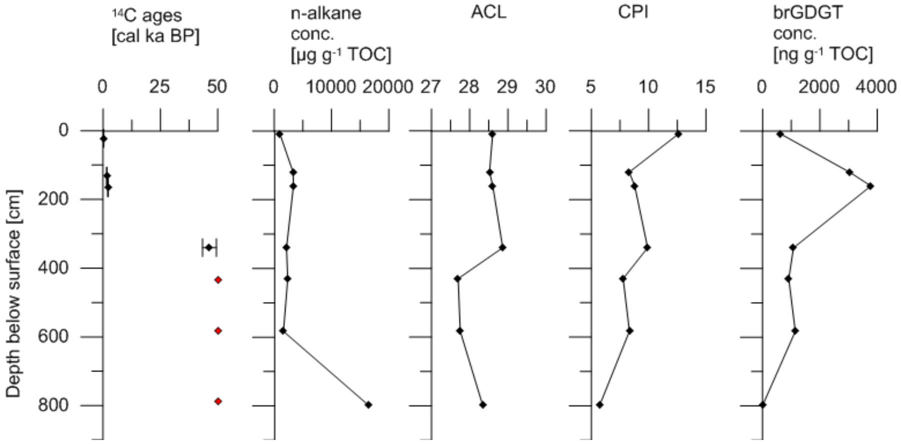

Figure 4.11: Summary of biomarker parameters of BAL16-B4: calibrated radiocarbon dates (infinitive ages in red), absolute lipid concentration per g of sediment, absolute concentration per g of TOC, ACL, CPI, brGDGT concentration per g per sediment and brGDGT concentration per g of TOC.

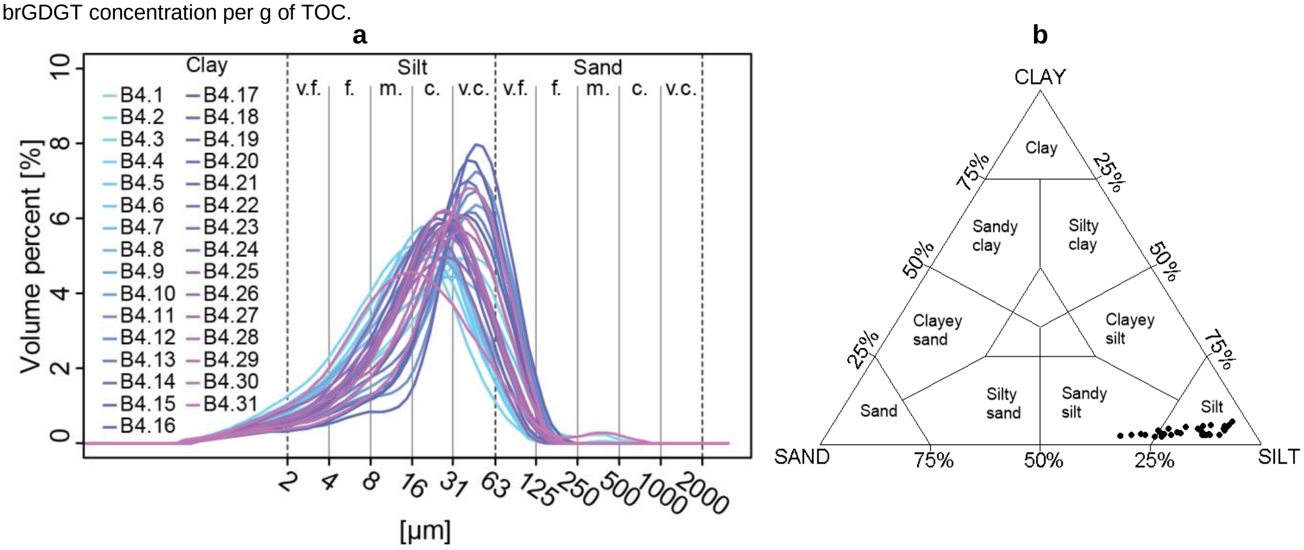

Figure 4.12: Grain size characteristics of BAL16-B4.a) Distribution and b) ternary diagram after Shepard (1954)

Table 4.5: Summary of brGDGT parameters of BAL16-B4: BIT, MBT and MAT according to Weijers et al. (2007) and MBT' and MAT' according to Peterse et al., (2012).

Sample ID	**Ext. ID**	**Depth**	**BIT**	**MBT**	**MAT**	**MBT'**	**MAT'**
				Weijers et al. (2007)		**Peterse et al. (2012)**	
		[cm]			**[°C]**		**[°C]**
BAL16-B4-2	G016925	8	1.00	0.25	-10.9	0.25	-1.9
BAL16-B4-4	G016926	120	1.00	0.27	-1.4	0.27	3.9
BAL16-B4-6	G016927	160	1.00	0.30	-0.8	0.30	4.3
BAL16-B4-14	G016928	340	0.99	0.25	-1.1	0.25	4.0
BAL16-B4-18	G016929	430	1.00	0.21	-2.4	0.22	3.3
BAL16-B4-24	G016930	583	1.00	0.16	-7.3	0.16	0.2
BAL16-B4-31	G016931	798	n/a	n/a	n/a	n/a	n/a

4.1.4 BAL16-B5

DTLB exposure BAL16-B5 is about 3 meters high and the deposit is very peaty. The cryological, sedimentological and biochemical parameters are shown in Figure 4.13. The absolute ice content varies between 46 and 73 wt%. The bulk density shows relatively low values between 0.30 and 0.75*10^3 kg m^{-3}. The magnetic susceptibility has a maximum of 97 at 82 cm and a minimum of 10 at 30 cm. The TOC increases along the profile with values between 1.6 wt% at the bottom and 37.0 wt% at the top. The TOC/TN also increases along the profile from 13.1 to 35.4 at the surface. The $\delta^{13}C$ shows a positive trend ranging from -25.9 to -27.9‰.

The grain size was measured for the samples at 30 and 82 cm (Figure 4.14). The grain size could not be measured in the two lower samples of this profile, because the required concentration for the laser was not reached. The two samples show very similar grain size characteristics with poorly sorted sediment. The distribution is fine skewed (mean skewness = -0.23), mesokurtic (mean kurtosis = 1.06) and unimodal. The clay content is low (5 and 7 vol%), as is the sand content (11 and 8 vol%). The samples are both dominated by silt (85 and 86 vol%), which is also shown in the ternary diagram (Figure 4.14b). The mean grain is 19 and 16 µm, respectively.

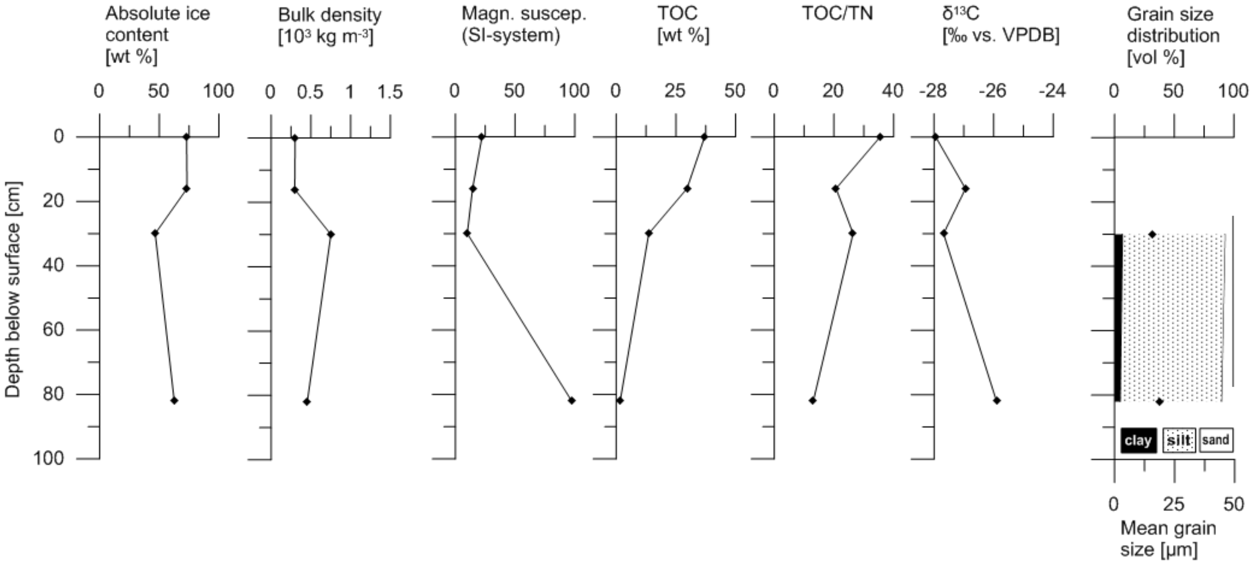

Figure 4.13: Summary of cryological, sedimentological and biochemical parameters of BAL16-B5: absolute ice content, bulk density, magnetic susceptibility, TOC, TOC/TN, $\delta^{13}C$, grain size distribution and mean grain size.

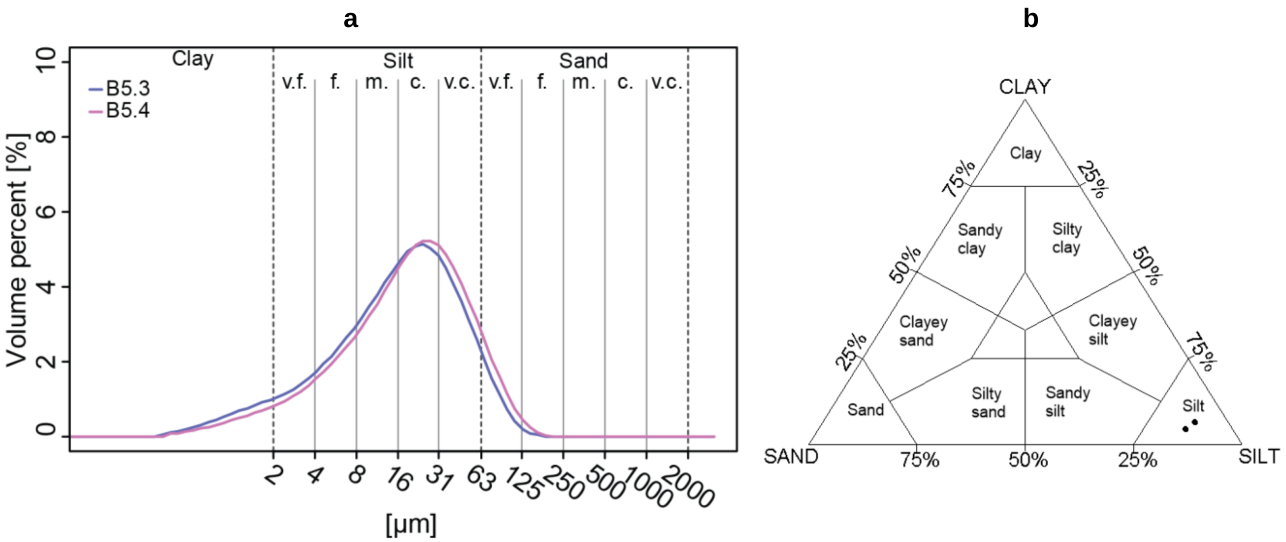

Figure 4.14: Grain size characteristics of BAL16-B5. a) Distribution and b) ternary diagram after Shepard (1954).

4.1.5 BAL16-UPL1-L1

The thermokarst lake is subcircular with a N-W extent of about 1400 m long and 800 m wide and and the water depth is 135 cm at the coring site. Unfrozen lake sediments were cored, the core was compacted from 34 cm long to 29 cm within five days due to loss of about 50 g of water. Figure 4.15 shows the profile of the lake core on the right. The sediment medium silty to clayey, slightly layered and organic layers are visible at 4, 5, 7 cm depth, as well as thicker organic layers at 15-16 and 19-20. Rootlets and mosses were visible at 5 cm.

Table 4.6: Radiocarbon dates of BAL16-UPL1-L1. Calibrations were performed using CALIB 7.1 softwrare and the IntCal13 calibration curve (Stuiver et al., 2017). Poz: Poznan Radiocarbon Laboratory, Poland.

Sample ID	**Ext. ID**	**Depth** [cm]	**^{14}C ages** [a BP]	**±**	**Mean cal ages 2σ (95.4%)** [a BP]	**±**	**Rounded ^{14}C ages** [cal a BP]	**±**
BAL16-UPL1-L1-A	Poz-89349	19-20	425	30	482	43	480	40
BAL16-UPL1-L1-B	Poz-89351	26.5-27.5	1,940	30	2,014.5	64.5	2,010	60

The age of the lake sediments is 2,010 cal a BP at a depth of 26.5-27.5 cm and 480 cal a BP at 19-20 cm (Table 4.6). The obtained parameters are shown in Figure 4.15. The bulk density is constant around 0.42*10^{-3} kg m^{-3}. The magnetic susceptibility ranges between 20 and 46. The record shows quite some variation in the lower part up to 10 cm with minima at 25.0 cm (23), 19.5 cm (20) and at 12.0 cm (29). The magnetic susceptibility in the upper 10 cm is stable around 40. The TOC is constant between 13.8 and 14.4 wt%. The TOC/TN is also very stable around 22.5. The δ^{13}C shows a slight decrease from -28.4 in the bottom to -28.8‰ in the top.

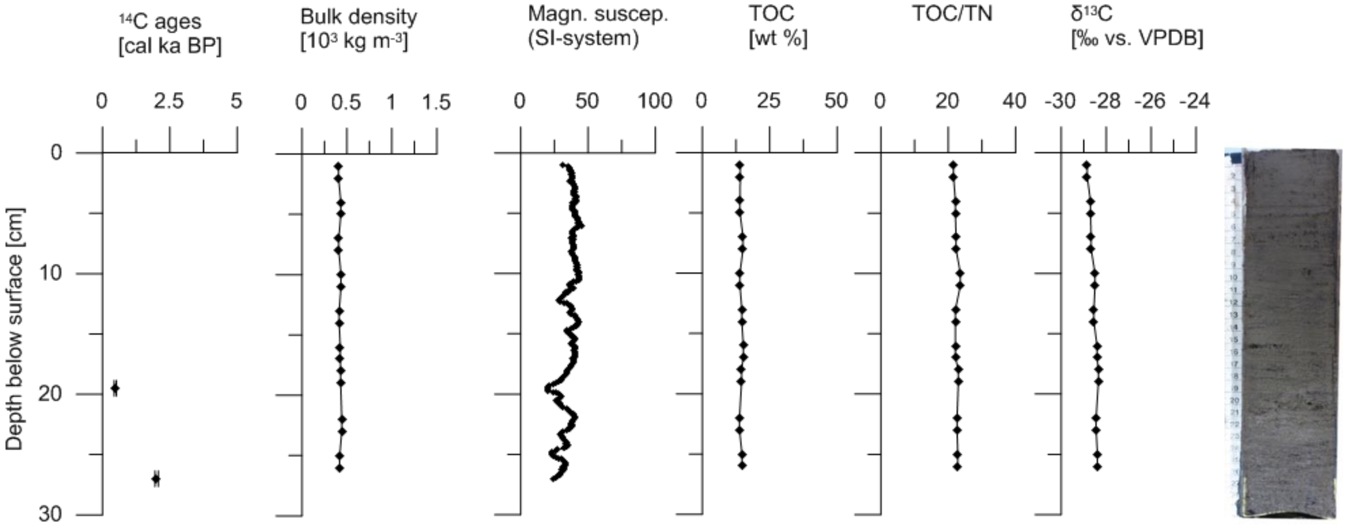

Figure 4.15: Summary of cryological, sedimentological and biochemical parameters of BAL16-UPL1-L1: calibrated radiocarbon dates (note: different axis), bulk density, magnetic susceptibility, TOC, TOC/TN and δ^{13}C. Picture of core displayed on the right.

4.2 Statistical significance

A Mann-Whitney-Wilcoxon was applied to test for differences between yedoma and DTLB exposures (Table 4.7). Furthermore, a Kruskal-Wallis test was used on the biogeochemical parameters between the yedoma exposure, DTLB exposures and thermokarst lake core (Table 4.7 in grey). Significant differences were revealed for TOC, TOC/TN, $\delta^{13}C$, volumetric organic carbon content, n-alkane concentration (μg g^{-1} sediment and μg g^{-1} TOC), brGDGT concentration (μg g^{-1} sediment), CPI and CBT.

Table 4.7: Outcome statistical tests: The upper row contains the p-values and the lower row indicates whether the difference between the groups is significant (and thus whether the null hypothesis has been rejected). The outcome of the Kruskal-Wallis test is displayed in grey.

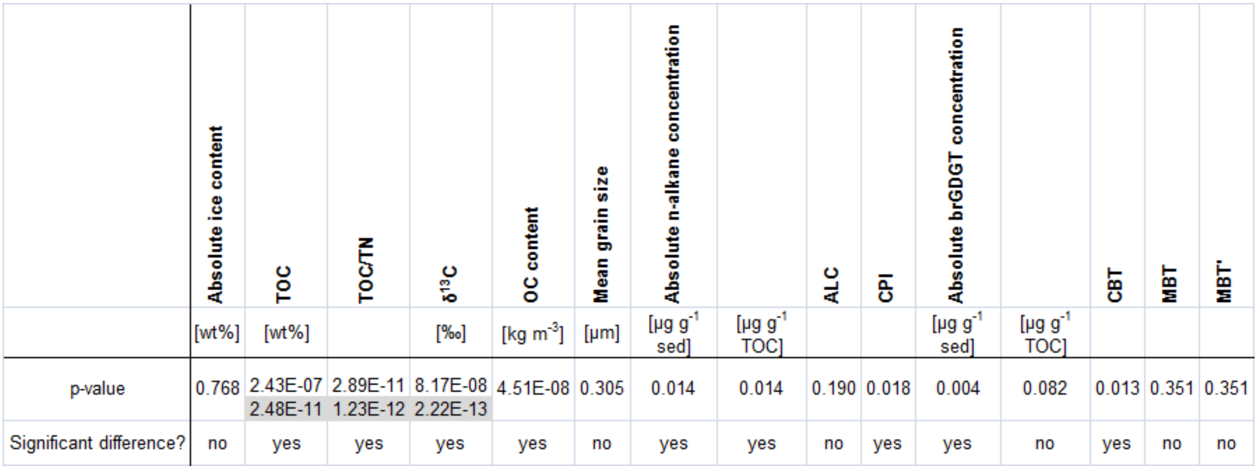

	Absolute ice content [wt%]	TOC [wt%]	TOC/TN	$\delta^{13}C$ [‰]	OC content [kg m^{-3}]	Mean grain size [µm]	Absolute n-alkane concentration [µg g^{-1} sed]	[µg g^{-1} TOC]	ALC	CPI	Absolute brGDGT concentration [µg g^{-1} sed]	[µg g^{-1} TOC]	CBT	MBT	MBT'
p-value	0.768	2.43E-07 2.48E-11	2.89E-11 1.23E-12	8.17E-08 2.22E-13	4.51E-08	0.305	0.014	0.014	0.190	0.018	0.004	0.082	0.013	0.351	0.351
Significant difference?	no	yes	yes	yes	yes	no	yes	yes	no	yes	yes	no	yes	no	no

4.3 Remote sensing

Figure 4.16 shows a false color image (a) and DTM (b) of the southwest coast of the peninsula. In the false color image, it is clearly seen that the peninsula mainly consists of drained lake basins and thermokarst lakes: water is colored black, the drained lake basins are recognized as round-shaped polygons. The basins are on different elevational levels and intersect each other (Figure 4.17b). A land cover classification map was produced distinguishing between DTLBs (green), yedoma (yellow), thermokarst lake (blue) and surface water (white) (Figure 4.17b). For the latter no information is available, so this area is left out of further calculations. The total area mapped is about 450 km^2 of which ~65% is DTLB, ~30% is yedoma and ~5% is thermokarst lake (Table 4.8).

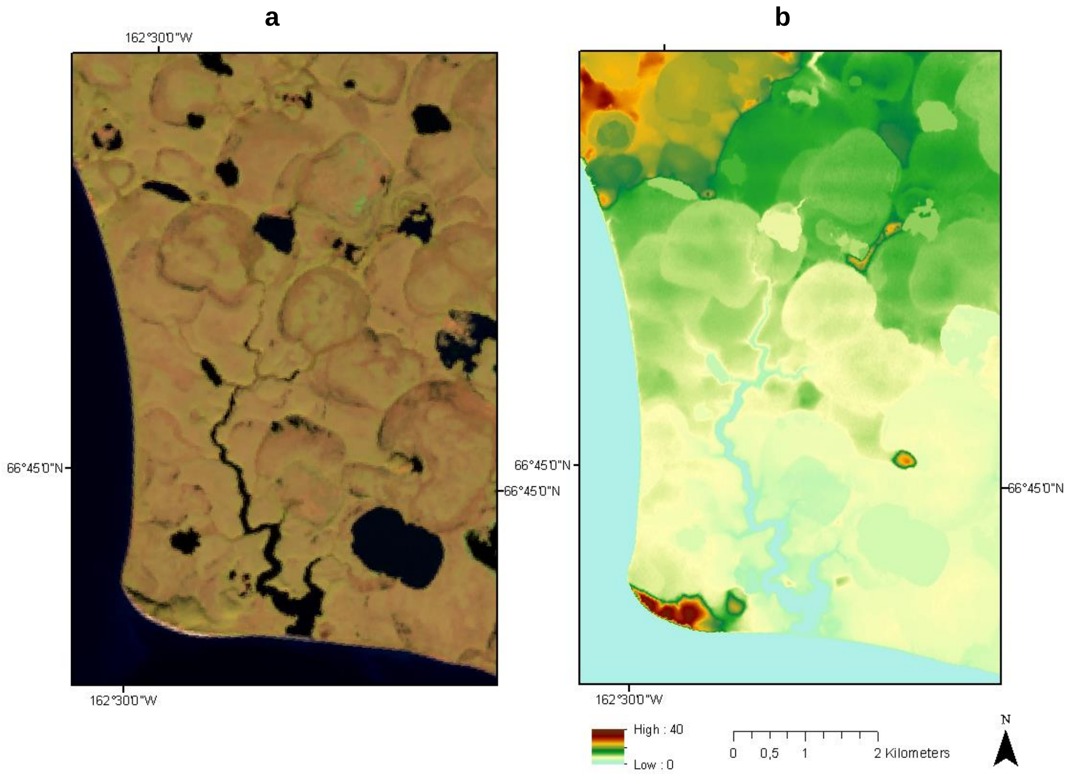

Figure 4.16: Thermokarst development on Baldwin Peninsula. a) False color image with short-wave infrared, near-infrared and deep blue bands (7-5-1). b) Digital Terrain Model showing elevation from 0.40 m. Landsat 8 image from 13.10.2016.

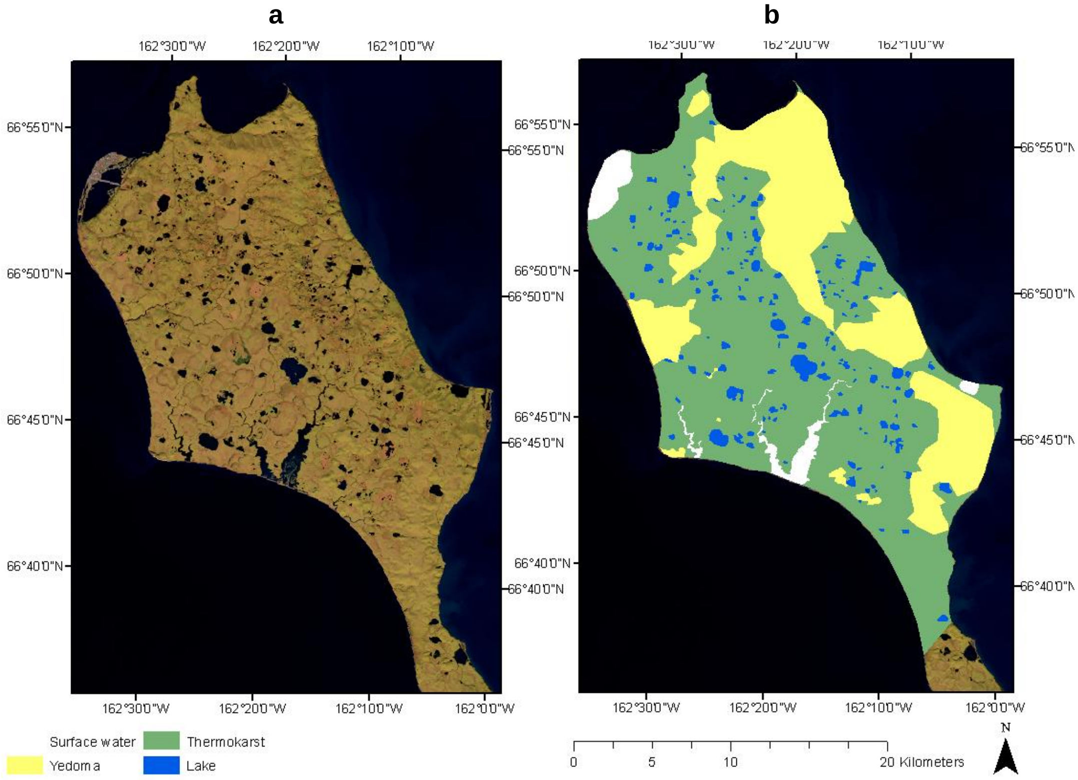

Figure 4.17: Land cover classification of Baldwin Peninsula. a) False color image. b) Land cover classification with drained thermokarst lake basin deposits (green), yedoma deposits (yellow), thermokarst lakes (blue) and surface water (white).

Table 4.8: Coverage of landscape units on Baldwin Peninsula: yedoma, drained thermokarst lake basin (DTLB) and thermokarst lake.

Landscape unit	Coverage [m^2]	Coverage [%]
Yedoma	136,620,000	30
DTLB	296,440,000	65
Thermokarst lake	21,180,000	5

4.3.1 Organic carbon budget

The organic carbon budget is calculated according to Equation 4. Hence, thickness and regional coverage of the deposits need to be considered, as well as bulk density, wedge-ice volume and TOC of the samples. In the calculations, frozen and unfrozen deposits are treated separately. Based on field observations, the following deposit thicknesses were assumed: 15 m for yedoma deposits, 5 m for DTLB deposits and 2 m for thermokarst lake sediments. The coverage per landscape unit is taken from Table 4.8. Bulk density was calculated for the exposure samples and the thermokarst lake samples according to Equation 2a and b, respectively. Values for wedge-ice volume for drained lake basin (8.9 vol%) and yedoma (46.3 vol%) exposure sites from Siberia and Alaska were taken from Ulrich et al. (2014). Wedge-ice volume was assumed to be zero for the thermokarst lake sediments. Weighted TOC values were used to compensate for the representation of the samples, as different sampling intervals were used.

The field data were extrapolated to the whole peninsula. The volumetric and absolute organic carbon budget per stratigraphic landscape unit for the frozen deposits and unfrozen thermokarst lake deposits is given in Table 4.9. The thermokarst lake sediments contain 61 kg OC m^{-3} which adds up to an absolute budget of 2.6 Mt. The yedoma deposits contain 8.2 kg OC m^{-3} and the DTLB 24.2 kg OC m^{-3}, corresponding absolute values of OC storage are 16.8 Mt in yedoma and 35.8 Mt in DTLB deposits. The final estimation led to a total organic carbon budget of the frozen sediments on Baldwin Peninsula of 52.7 Mt (deeper deposits below frozen yedoma and DTLB deposits are excluded).

Table 4.9: Estimation of organic carbon budget on Baldwin Peninsula in landscape units yedoma, drained thermokarst lake basin (DTLB) and thermokarst lake.

Landscape unit	Volumetric OC budget [kg m^{-3}]	Absolute OC budget [Mt]
Yedoma	8.2	16.8
DTLB	24.2	35.8
Thermokarst lake	61.1	2.6

Furthermore, an estimation of the OC pool during the Late Pleistocene was made (Table 4.10). By subtracting the modern budget from the Late Pleistocene budget, a rough OC loss from frozen deposits on the Baldwin Peninsula since the Pleistocene was made. In this calculation, it was assumed that the whole peninsula was covered by frozen yedoma deposits. The field data from yedoma exposure BAL16-B2 were extrapolated to the whole peninsula. This leads to an Late Pleistocene OC budget of 55.9 Mt and therefore, a net OC loss of 3.3 Mt was estimated.

Table 4.10: Estimation of organic carbon loss on Baldwin Peninsula since Late Pleistocene in landscape units yedoma, drained thermokarst lake basin (DTLB) and thermokarst lake.

	Modern OC budget [Mt]	**Late Pleistocene OC budget [Mt]**	**Net OC loss [Mt]**
Frozen deposits	52.7	55.9	3.3

5. Discussion

The landscape units that were studied are part of the thermokarst development cycle (section 2.2). It starts with yedoma deposits which are relatively undisturbed and contain large ice wedges. The next step in the cycle is the formation of the thermokarst lakes which is a time of higher lake productivity. Finally, the lakes are drained and the permafrost can reform again, resulting in the drained lake basins. Due to different processes going on during these phases, the sediments and the organic carbon in the soil differ between the landscape units. Here, all parameters will be discussed and compared. The discussion is split into two parts: the depositional environment and organic carbon pools. Section 5.1 describes the depositional environment of the sediments by discussing the geochronology, sedimentology and climatic parameters. Section 5.2 describes the organic carbon pools by discussing the source (Section 5.2.1), quality (Section 5.2.2) and quantity (5.2.3) of the organic carbon.

5.1 Depositional environment

The formation of the yedoma started (> 50 ka BP) in the Early Wisconsinan. Two samples were dated to be much younger (10 and 19.6 ka BP). There is no clear trend of age against depth in yedoma exposure BAL16-B2. The near-surface sample in the exposure is very old, whereas the lowermost sample is younger than the overlying samples. Hence, the exposure does not follow the principle of superposition. Dating of syngenetic sediments concerns several issues (Vasil'chuk et al., 2017). Syngenetic sediments can contain allochthonous material due to the fluvial or alluvial character of deposition. Also, the permafrost sediments generally have a high potential of preservation of old carbon. Uptake of old carbon can cause overestimation of ages. Rejuvenation is generally restricted to active layer sediments, as modern carbon cannot enter the frozen sediments. Vasil'chuk et al. (2017) showed that the youngest ages in the syngenetic sediments are typically closest to the actual timing of accumulation, and older ages should be rejected. However, in this approach one should pay attention to modern carbon contamination. Hence, syngenetic sediments can show both overestimations as well as underestimations in dating, because of re-deposition of older carbon or transport and refreezing of material downhill.

The thermokarst lake sediments at BAL16-UPL1-L1 have been deposited during the Holocene. The sedimentation rate between 2,010 and 480 a BP of ~5 cm ka^{-1} is very low (Table 5.1). It is possible that there is a hiatus in the sediment record. Assuming that the surface sediments have been deposited recently, the sedimentation rate over the past 480 years is ~40 cm ka^{-1}. This fits very well to the results of Lenz et al. (2016c) who showed a sedimentation rate of ~40 cm ka^{-1} (40-0 cm over 1060 cal a BP-today) in thermokarst lakes on the Seward Peninsula (peninsula south of Kotzebue Sound). The magnetic susceptibility minima at 19.5 cm might be related to the organic layer that is visible at 19-20 cm and suggests an enrichment of organic matter.

Table 5.1: Lake sedimentation rates

Age [cal a BP]	**Sedimentation rate [cm ka^{-1}]**
0	
	41 +4/-3
480 +/- 40	
	4.9 +0.3/-0.3
2,010 +/- 60	

The largest part of the peninsula consists of drained thermokarst lake basins. Partial drainage of lakes led to the origin of smaller lakes in the remnants of old basins. Also, new lakes formed in the older basins. This is shown by the fact that the different lake basins intersect each other and are situated on different elevations. The DTLB exposure BAL16-B4 was dated: the lower part of the exposure up to 340 cm is older than 46 ka BP, whereas the samples above (166 cm to surface) are younger than 2,100 a BP. Here it is hypothesized that the younger part was deposited during the development of a Holocene thermokarst lake in the older yedoma deposits. The upper sediments were likely deposited in a thermokarst lake and after drainage, and the lower sediments were probably part of the unfrozen talik underneath the lake. The absolute ice content and bulk density suggests a different character of the two parts of the exposure.

The analysis of grain size distribution can be used to deduce the source of sediments or a change in depositional regime. The exposures show relatively little variation in grain size distribution (Figure 5.1). The sediments consist of silt to sandy silt and show a unimodal distribution, which indicates the dominating aeolian transport. In some samples, a small peak is visible in the middle sand domain. This and the fact that the sediment is poorly sorted, indicate that also other transport processes have played a role. A large portion of the Baldwin Peninsula has likely been covered by yedoma during the Late Pleistocene. It has been partly exposed to thermokarst processes already since the Late Pleistocene, but the main disturbances probably occurred later in the Holocene. The little variation in the grain size distribution points to a stable depositional mechanism and suggests a common sediment source of the yedoma and thermokarst deposits: yedoma deposits have been subsided and reworked by thermokarst processes.

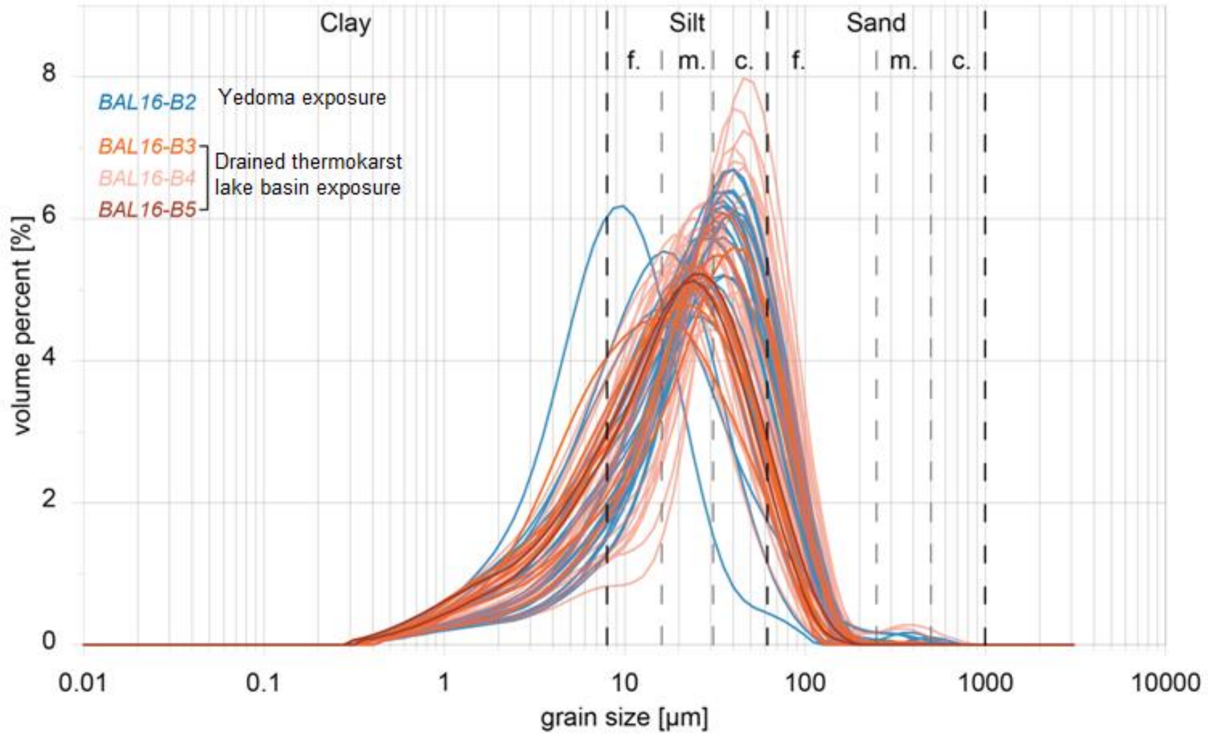

Figure 5.1: Grain size distributions of yedoma (blue) and thermokarst deposits (red shades).

The yedoma deposit at Baldwin Peninsula does not show the characteristic multimodal grain size distribution that is described for Siberian yedoma deposits (Schirrmeister et al., 2008; Strauss et al., 2012). However, previous studies have showed that Alaskan yedoma deposits generally have a larger influence of aeolian transport and show a more unimodal grain size distribution (Strauss et al., 2012; Schirrmeister et al., 2016). Yedoma in Alaska is often present in foothill regions, on north-facing slopes and in narrow valleys (Schirrmeister et al., 2013). This leads to a unimodal character in Alaskan yedoma deposits. Also, the homogenous character is typical for yedoma deposits (Strauss et al., 2012; Murton et al., 2015).

The lower three samples (1870 to 1700 cm) were taken in the sediments underneath the yedoma. As shown before (Section 4.1.1), the grain size distribution of these three samples differs from that of the sediments above. Performing the Mann-Whitney-Wilcoxon test on the two groups (yedoma vs. sediments below yedoma), pointed out that the mean grain size is significantly different ($p<0.01$). This implies a change in depositional mechanism, which is supported by the variable magnetic susceptibility in the lower part of the exposure. This confirms the different character of the yedoma and the sediments underneath. These underlying sediments are likely part of the Baldwin silt unit described by Huston et al. (1990) and Pushkar et al. (1999).

As was shown in Section 4.1.3, the grain size characteristics of the DTLB exposure BAL16-B4 is different for the lower part (up to 280 cm) and the upper part, regarding the distribution and mean grain size. The lower sediments are very similar to the yedoma deposits. No clear trend over depth is shown in BAL16-

B4. The magnetic susceptibility of the DTLB exposure BAL16-B3 and B5 decreases upwards, which indicates an enrichment of organic carbon.

The frozen deposits on the Baldwin Peninsula have a mean absolute ice content of ~45 wt% (excluding wedge-ice volume). Because of the high ice content, the deposits are highly susceptible and vulnerable to permafrost thaw.

The BIT and MBT indices based on the brGDGTs were used to reconstruct the past climate. The BIT index is lower for BAL16-B2 (mean BIT = 0.94) than for BAL16-B4 (mean BIT = 1.00). This indicates that the yedoma is deposited in drier conditions than the thermokarst deposits. This is line with other paleo-reconstructions from Alaska (Lenz et al., 2016a) and Siberia (Andreev et al., 2011). The MBT is lower when compounds containing more methyl branches are formed, which occurs at lower temperatures. Soils in the Arctic are generally dominated by brGDGTs with additional methyl branches (Weijers et al., 2007). The yedoma samples are mostly dominated by brGDGT-II. The larger relative contribution of brGDGT-II in yedoma was also found by Peterse et al. (2014) in Late Pleistocene yedoma cliff samples from Duvannyi Yar, Siberia. The DTLB exposure shows a larger relative contribution of brGDGT-III in the lower (older) and of brGDGT-II in the upper (younger) part with mean MBT values of 0.21 and 0.27, respectively. This suggests that the depositional environment of the lower sediments was colder than that of the overlying sediments.

Assuming that average temperatures were lower in the Pleistocene and increased during the Holocene, the MAT and MAT’ for both yedoma and thermokarst deposits are relatively high (range between -10.9 to 7.6°C). The MAT’ values presented in this study were on average ~4.5°C higher than the MAT values. When applying the MBT/CBT transfer function on brGDGT distributions in Arctic sediments, two main problems come to light. Firstly, Arctic environments are characterized by large seasonal variation in temperature and ice cover. This results in a short growing season and therefore, the MBT/CBT is likely not a representative proxy for annual air temperature, but represents growing season (i.e. summer) temperatures instead (Pearson et al., 2011; Peterse et al., 2014). Hence, the MAT values are biased by seasonality differences and it is not yet known how large this bias is and how it differs for the different landscape units. Secondly, it was pointed out that the revised MBT’/CBT’ transfer function (Peterse et al., 2012) results in reconstructed temperatures that are up to ~8°C higher than the original transfer function, due to the flatter slope of the calibration. Although the revised function generates better MAT’ estimates for low- to mid-latitude soils, it overestimates MAT’ for higher latitudes (Peterse et al., 2014). Therefore, the MBT’/CBT’ transfer function does not lead to accurate estimates for MAT’ in this study.

5.2 Organic-matter pools

To estimate future release of greenhouse gases from permafrost soils, the thaw-vulnerable OC pool needs to be identified. Therefore, the OC pool on Baldwin Peninsula is assessed whereby the quantity, source and quality of the OC are identified. Furthermore, the differences between the different stratigraphic landscape units present on the peninsula are described.

5.2.1 Organic carbon quantity

The amount of OC stored on Baldwin Peninsula was estimated (Equation 4). The regional coverage of the landscape units was derived from the land cover classification map. Average values for deposit thickness, TOC and BD were extrapolated from the five study sites to the whole Baldwin Peninsula. Values for wedge ice volume of the yedoma and DTLB deposits were taken from Ulrich et al. (2014). Firstly, the TOC of the different landscape units is discussed. Afterwards, the carbon budget is discussed and compared to previous studies.

The TOC of the yedoma exposure has an average of 1.9 wt% (range from 0.1 to 4.7 wt%). This fits well to TOC variations from previous yedoma study sites across Siberia and Alaska (Figure 5.2). The thermokarst lake contains the most OC (mean = 14.4), which is likely due to the lake productivity, even though thermokarst lakes are generally characterized by low primary production under Arctic climate (Lenz et al., 2016b). The DTLB deposits cover a large range of values, which can be explained by the shared features of the yedoma and thermokarst lake facies. Although the mean TOC of the yedoma deposits is not very high, when comparing to DTLB deposits and thermokarst lake sediments, the volume of the yedoma deposits is of great importance, as the deposits are generally between 10 and 30 m thick.

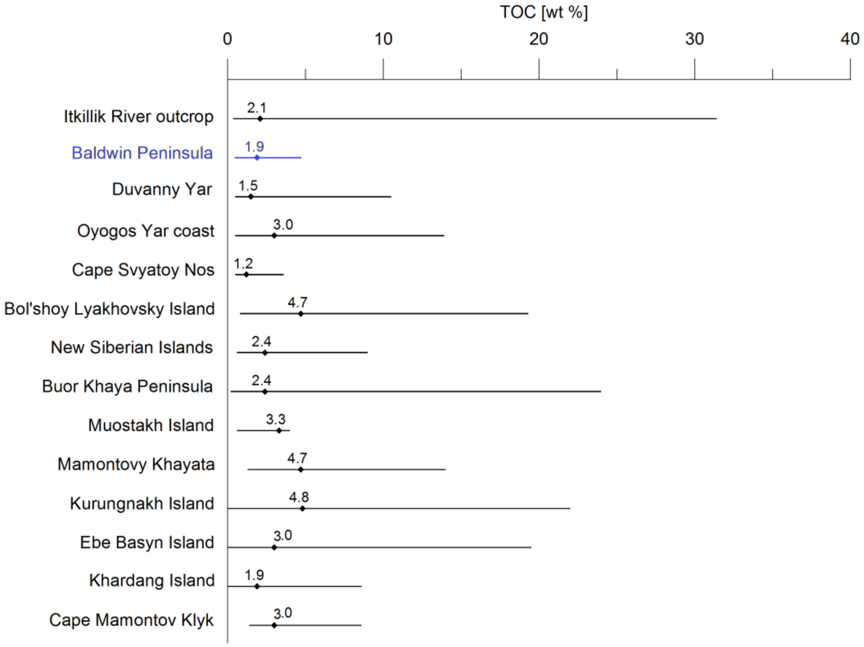

Figure 5.2: TOC variations from different yedoma study sites in Siberia and Alaska. Sorted from easternmost (Itkillik River outcrop, Alaskan North Slope) to westernmost (Cape Mamontov Klyk, western Laptev Sea) study sites from Schirrmeister et al. (2008a), Schirrmeister et al. (2008b), Schirrmeister et al. (2011), Strauss et al. (2013) and Strauss et al. (2015), including Baldwin Peninsula from this study (blue).

The OC budget calculations showed that yedoma deposits contain 8 kg OC m^{-3} and DTLB deposits 24 kg OC m^{-3}. Comparable data were found by Schirrmeister et al. (2011) and Strauss et al. (2013) (Table 5.2) who estimated the volumetric OC budget in northern East Siberia and the total yedoma region (~1,387,000 km^{2}), respectively. Both studies showed a ~3 times higher volumetric OC budget for DTLB deposits compared to yedoma deposits. The data from Baldwin Peninsula showed that ~70% (36 Mt) of the OC pool in frozen deposits is stored in DTLB deposits and ~30% (17 Mt) in yedoma deposits. The thermokarst lake deposits store 2.6 Mt OC.

Table 5.2: Estimations of volumetric OC budget from other studies in landscape units yedoma and drained thermokarst lake basin (DTLB).

		Northern East Siberia	**Total yedoma region**
Landscape unit	**Baldwin Peninsula**	**Schirrmeister et al. (2011)**	**Strauss et al. (2013)**
	[kg m^{-3}]	**[kg m^{-3}]**	**[kg m^{-3}]**
Yedoma	8.2	14+/-3[a]	10+7/-6
DTLB	24.2	45+/-23[a]	31+23/-18

[a] Data from Schirrmeister et al (2011), recalculated to include wedge-ice volume.

About 70% of the area of Baldwin Peninsula is affected by degradation (~65% DTLB and ~5% thermokarst lake). The degradation processes led to more than 10 m of ground subsidence compared to the yedoma level. An estimation was made of the OC budget during the Late Pleistocene (56 Mt), assuming that Baldwin Peninsula was covered entirely with yedoma deposits. The net OC loss since the Late Pleistocene is 3.3 Mt. The fact that it is a net loss means that much more OC has been produced (e.g. in thermokarst lakes) but even more degraded. Moreover, this calculation assumes the same surface area for Late Pleistocene and now, so it does not include the surface area that was lost to coastal erosion which means that it is an underestimate.

5.2.2 Organic carbon source

The degradability of OC is highly dependent on the quantity and quality of the material, rather than on the age (Knoblauch et al., 2013; Strauss et al., 2013; Stapel et al., 2016). Therefore, it is of great importance that it is known where the OC comes from and what state it is in. The source of organic matter is discussed based on the TOC/TN ratio, stable carbon isotopes and biomarker distributions.

The TOC/TN ratio is an indicator for the source of organic carbon and the degree of degradation of the material. Stable carbon isotopes can be used to distinguish between marine and continental plant sources (Meyers, 1994). Figure 5.3 shows a scatter plot of the TOC/TN and $\delta^{13}C$ per study site. All sites have $\delta^{13}C$ values between -30 and -24‰, which indicates that the organic matter is terrestrially derived. The yedoma exposure has TOC/TN ratios up to 14. The low values could be an indication of an influence of organic material derived from algae. The thermokarst lake has high TOC/TN values with a mean of 22.5. Furthermore, the $\delta^{13}C$ of the thermokarst lake sediments are low (mean = -28.5‰), which is typical for lacustrine algae (Meyers, 1994). The DTLB exposures show a large range of TOC/TN ratios, which can be explained by the large variance in TOC.

The analysis of biomarkers showed high values for the average chain length of both the DTLB (>27.7) and the yedoma exposure (>28.2) which suggests that the organic matter is mainly derived from terrestrial higher plants (Killops and Killops, 2009). Additionally, Figure 5.4 shows the n-alkane distributions of the yedoma and DTLB exposures which show that the long- and odd-chains dominate. This is another indication that the OM is dominantly derived from terrestrial higher plants (Eglinton and Hamilton, 1967). These findings suggest that the variation in these TOC/TN and $\delta^{13}C$ should mainly be explained by the processes involved in the different phases of the thermokarst development. A trend is shown ranging from high $\delta^{13}C$ and low TOC/TN to low $\delta^{13}C$ and high TOC/TN, illustrated by the black arrow in Figure 5.3. This trend follows the thermokarst development starting with the old yedoma deposits in the upper left corner to the thermokarst lake sediments in the lower right corner and the DTLB deposits in between, as this is a mix between the other two facies.

It has been shown in Section 4.1.3 that there is a difference in TOC and $\delta^{13}C$ values between the lower and upper sediments in DTLB exposure BAL16-B4. The upper 250 cm of the exposure contain relatively more OC and show lower $\delta^{13}C$ values which could be an indication for lake production. These findings are therefore, in agreement with the hypothesis (section 5.1) that the upper 250 cm of the exposure was deposited during thermokarst lake development and after drainage.

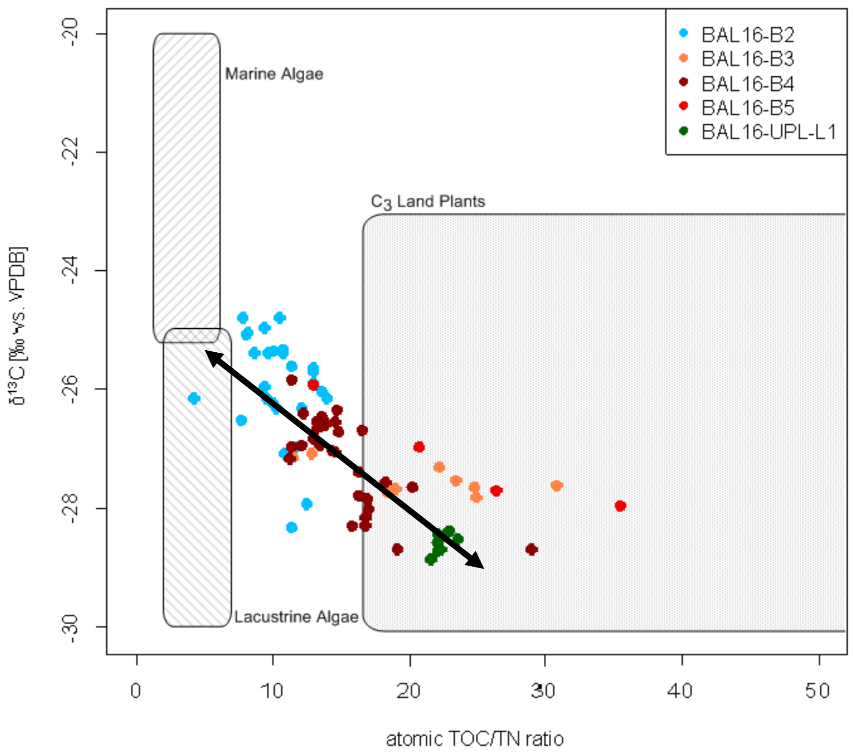

Figure 5.3: Scatterplot of $\delta^{13}C$ and TOC/TN ratio of yedoma exposure BAL16-B2 (blue), drained thermokarst lake basin exposures BAL16-B2 to B5 (shades of red) and thermokarst lake sediments BAL16-UPL1-L1 (green) with trend between the different facies indicated with the black arrow.

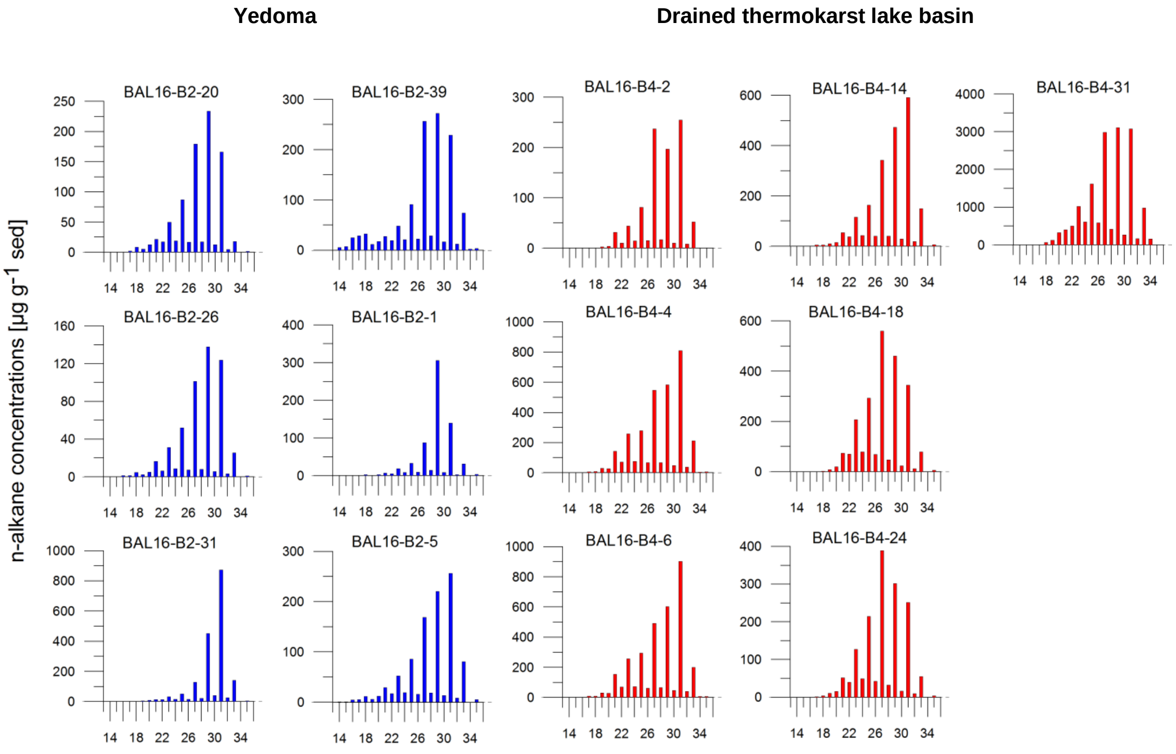

Figure 5.4: n-Alkane concentrations of yedoma (blue) and drained thermokarst lake basin deposits (red).

Boxplots of the n-alkane and brGDGT concentration for yedoma and DTLB deposits are shown in Figure 5.5. The DTLB deposits have higher concentrations of both n-alkanes and brGDGTs. The statistical tests pointed out that the differences are significant in n-alkane concentration per gram of sediment and per gram of TOC as well as in brGDGT concentration per gram of sediment. This suggests a different composition of the OC. Yet, no significant difference was found in the brGDGT concentration per gram of TOC, implying a different source of the clastic material between the yedoma and DTLB deposits but a similar source of brGDGTs.

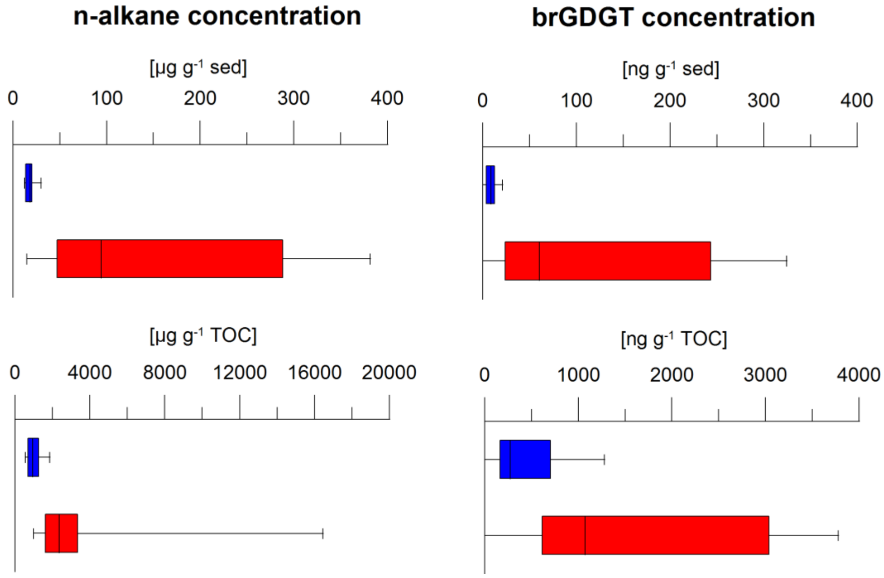

Figure 5.5: Boxplots of biomarker parameters of yedoma (blue; n=6) and drained thermokarst lake basin deposits (red; n=7). Concentrations of n-alkanes (left) and brGDGTs (right) per g of sediment (upper row) and per g of TOC (lower row).

5.2.3 Organic carbon quality

The degree of degradation of the organic carbon is discussed using the TOC/TN ratio and lipid biomarkers. Also, the future implications of climate change on the organic matter pool is discussed.

Permafrost locks organic carbon by freezing, thereby preserving the quality of the carbon. When permafrost soils are exposed to thermokarst, the carbon can be mobilized and reworked. The DTLB deposits have possibly gone through multiple thermokarst lake generations and therefore, the OC in these deposits is expected to be further degraded. This is indeed shown in the CPI values: an increasing trend upwards in the profile indicates that degradation has occurred. The lack of degradation-depth trend in yedoma suggests that minimal or no degradation has occurred. This shows that the OC is incorporated soon upon sedimentation and has mostly been freeze-locked since then (Strauss et al., 2015; Stapel et al., 2016).

Boxplots of the TOC/TN ratio and CPI are shown for the yedoma and DTLB exposures in Figure 5.6. The TOC/TN ratio is lower for the yedoma deposits than for the DTLB deposits, which suggests that the OC in the yedoma has been further degraded. This is in disagreement, however, with the previously shown absence of a degradation-depth trend in the yedoma exposure. Schirrmeister et al. (2011) states that sediments that have been deposited during a glacial or stadial period, are generally characterized by lower TOC and TOC/TN values and higher δ^{13}C values, indicating a stable environment and a reduced productivity. This would mean that the TOC and TOC/TN values are low in the yedoma deposits and do not necessarily reflect a strong degree of degradation. Furthermore, the CPI signal of the thermokarst deposits is significantly lower than that of the yedoma deposits which indicates better preserved carbon in the yedoma.

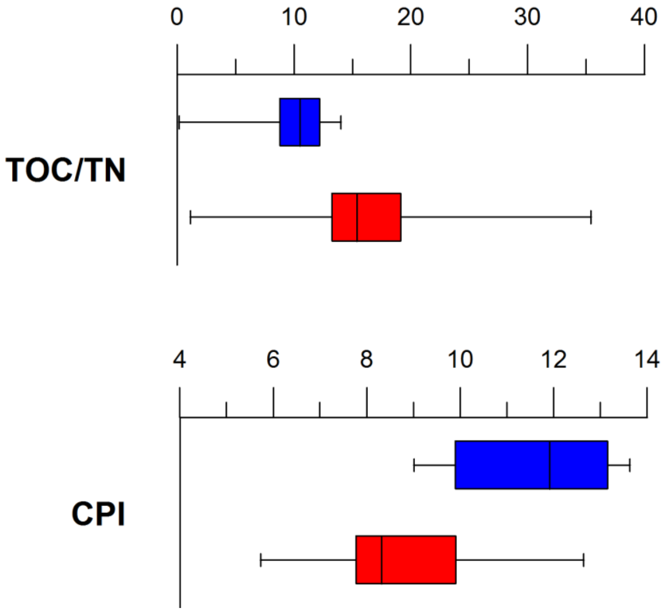

Figure 5.6 Boxplots of TOC/TN ratio and CPI of yedoma (blue; n=6) and thermokarst (red; n=7) deposits.

The TOC/TN values of the thermokarst lake sediments are very high (mean = 22.5), which suggests that the OC is fresh. The TOC/TN and CPI of the DTLB exposures cover a broad range (TOC/TN: 11.3-35.4 and CPI: 5.7-12.6) (Figure 5.3), which can be explained by the mixed character of the deposits: the sediments contain less degraded material originating from the yedoma deposits, as well as fresh input from the thermokarst lake. A large variance is also shown in the CPI values (Figure 5.6).

To discuss future implications of climate change, it is necessary to assess the vulnerability of the OC pool. Climate change will increase the frequency and intensity of fires and floods which can lead to soil removal and disturbances of the ground thermal regime. This can result in rapid local permafrost degradation (Grosse et al., 2011). Because of the high ice content in the yedoma and DTLB deposits on Baldwin Peninsula (>45 wt%, wedge-ice volume excluded), the deposits are highly susceptible and vulnerable to deep permafrost thaw which will lead to deep subsidence and deep thaw features and have a great effect on the topography. With the formation of new, deep lakes, primary productivity is expected to increase on a large scale, which will compensate for increased greenhouse emissions at first. However, due to more intensive permafrost degradation, lake drainage rates will be higher, which could lead to rapid decomposition (Walter Anthony et al., 2014). The largest share of OC on Baldwin Peninsula is stored in the DTLB deposits (~70% of OC in frozen deposits). The OC stored in yedoma deposits, however, as shown by the absolute CPI values as well as the lack of degradation-depth trend in the CPI, is of high quality. Therefore, the OC in the yedoma is especially vulnerable to future microbial degradation and greenhouse gas release. This will enhance the positive feedbacks and therefore enhance the warming.

6. Conclusion

The aim of this research was to reconstruct the late Quaternary depositional environment and organic carbon characteristics of a thermokarst affected landscape. The depositional environment of the sediments was studied for a better understanding of the processes involved in thermokarst affected areas. The extent and quality of the organic carbon pool was studied to identify the vulnerability to climate change. Differences between the different landscape units were discussed to assess the vulnerability of the deposits in different stages of thermokarst development.

The first objective was to characterize the sediments by identifying paleoenvironmental conditions during deposition and the regional coverage of the landscape units. The yedoma deposits on Baldwin Peninsula were deposited under a constant depositional regime. Yedoma formation started in the Early Wisconsinan (> 50 cal ka BP) and likely lasted into marine isotope stage 2 (ca. 30-10.3 ka BP). The drained thermokarst lake basin (DTLB) probably formed during the Holocene in older yedoma deposits. The grain size characteristics show that the transport mechanism was likely dominantly aeolian in both yedoma and DTLB deposits. The similar character of the deposits suggests that the yedoma and DTLB deposits share a common sediment source. Nevertheless, differences in grain size distributions and organic carbon parameters show that the sediments underlying the yedoma deposits were deposited in a different regime, and were probably part of the Baldwin silt unit. The yedoma and DTLB deposits have high ground ice contents (> 45 vol%, wedge-ice excluded). The thermokarst lake sediments originate from the Holocene and the upper 20 cm were dated back to 2,010 cal a BP. The BIT index suggests that the yedoma was deposited in a drier climate than the DTLB. The MBT shows that the older part of the DTLB was deposited in a colder climate than the upper, younger part. Baldwin Peninsula consists of ~65% of DTLB deposits, ~30% yedoma deposits and ~5% thermokarst lakes.

The second objective was to characterize the organic carbon pools by identifying the quantity, source and quality of the OC. The estimated volumetric OC budget is 8 kg m^{-3} in yedoma deposits, 24 kg m^{-3} in DTLB deposits and 61 kg m^{-3} in thermokarst lake sediments. The highest OC content is found in the thermokarst lake sediments, indicating higher productivity in the lake and recent input. The data show that 53 Mt OC is stored on Baldwin Peninsula, of which about 70% is stored in frozen DTLB deposits. Based on the assumption that the peninsula was entirely covered by yedoma deposits during the Late Pleistocene, it has been estimated that the net OC loss since the Late Pleistocene is about 3.3 Mt OC.

The results show a trend from yedoma deposits with low TOC/TN and high $\delta^{13}C$ to thermokarst lake deposits with high TOC/TN and low $\delta^{13}C$. The DTLB deposits are a mix of both facies and fall in the middle. The n-alkane concentrations and average n-alkane chain length show that the OC in the yedoma and DTLB deposits has originated from terrestrial higher land plants. The CPI indicate that the yedoma OC has not been altered (much) by microbial degradation and is therefore poorly degraded. The DTLB deposits show a degradation-depth trend in the CPI, which means that microbial alteration has occurred here. An explanation for the low TOC/TN values in the yedoma is that the sediments were deposited during a stadial indicating a stable environment and reduced productivity. The high TOC/TN values in the thermokarst lake reflect the fresh material, the low $\delta^{13}C$ suggests a lacustrine input.

The third objective was to decipher stratigraphical differences between the different landscape untis. The results show similarities as well as differences between the yedoma and DTLB deposits. The grain size distributions are similar, implying a stable depositional mechanism and a common sediment source. The climate was drier and colder during deposition of the yedoma. The volumetric OC budget of the DTLB is about 3 times higher than the yedoma deposits. Even though the yedoma deposits are thick (~15 m compared to ~5 m of DTLB deposits), the largest share of OC is stored in the DTLB deposits. Differences were found in the OC content and n-alkane and brGDGT concentrations, which indicates that the OC is of a different composition.

Future climate change will warm the Arctic further which will lead to the advanced degradation of permafrost. Because of the high ice content, the deposits are highly susceptible and vulnerable to permafrost thaw. The organic carbon quality of the yedoma OC on Baldwin Peninsula is high as the OC has been freeze-locked in the permafrost with minimal disturbances. Deep thaw features and disturbances will lead to fast decomposition of the OC, contributing to large-scale greenhouse gas emissions. Future research should include biomarker analyses for different environments and study areas, as this proved relevant in this study for deducing climatic parameters and for OC investigations. This study provided a basis for quantifying OC stored in thermokarst affected areas. These areas are very dynamic in the sense that large-scale ground subsidence occurs. Therefore, for improving the OC pool estimations, more data is required on the spatial variation in deposit thickness.

7. References

Andersson, R.A., Meyers, P., Hornibrook, E., Kuhry, P. and Mörth, C. (2012). Elemental and isotopic carbon and nitrogen records of organic matter accumulation in a Holocene permafrost peat sequence in the East European Russian Arctic. *Journal of Quaternary Science*, vol. 27, pp. 545-552.

Andreev, A.A., Schirrmeister, L., Tarasov, P.E., Ganopolski, A., Brovkin, V., Siegert, C., Wetterich, S. and Hubberten, H. (2011). Vegetation and climate history in the Laptev Sea region (Arctic Siberia) during Late Quaternary inferred from pollen records. *Quaternary Science Reviews,* vol. 30, pp. 2182-2199.

Begét, J.E., Stone, D.B. and Hawkins, D.B. (1990). Paleoclimatic forcing of magnetic susceptibility variations in Alaskan loess during the late Quaternary. *Geology*, vol. 18, pp. 40-43.

Blott, S.J. and Pye, K. (2001). GRADISTAT: A grain size distribution and statistics package for the analysis of unconsolidated sediments. *Earth Surface and Landforms*, vol. 26, pp. 1237-1248.

Brown, J., Ferrians, O.J., Heginbottom, J.A. and Melnikov, E.S. (1998). Circum-Arctic Map of Permafrost and Ground-Ice Conditions. Boulder (CO): National Snow and Ice Data Center/World Data Center for Glaciology.

Burn, C.R. and Smith, M.W. (1990). Development of thermokarst lakes during the Holocene at sites near Mayo, Yukon Territory. *Permafrost and Periglacial Processes,* vol. 1, pp. 161-176.

Christopherson, R.W. (2009). Glacial and Periglacial Processes and Landforms, in *Geosystems: An Introduction to Physical Geography*, 7th Edition. Coty, State: publisher.

Cohen, A.S. (2003). Paleolimnologoy: The history and evolution of lake systems. US, New York: Oxford University Press.

Dirghangi, S.S., Pagani, M., Hren, M.T. and Tipple, B.J. (2013). Distribution of glycerol dialkyl glycerol tetraethers in soils from two environmental transects in the USA. *Organic Geochemistry,* vol. 59, pp. 49-60.

Eglinton, G. and Hamilton, R.J. (1967). Leaf Epicuticular Waxes. *Science,* vol. 156, pp. 1322-1335.

Folk, R.L. and Ward, W., C. (1957). Brazos River bar: A study in the significance of grain size parameters. *Journal of Sedimentary Petrology,* vol. 27, pp. 3-26.

French, H.M. (2007). *The Periglacial Environment*. New York, NY: John Wiley and Sons Ltd.

Glombitza, C., Mangelsdorf, K. and Horsfield, B. (2009). Maturation related changes in the distribution of ester bound fatty acids and alcohols in a coal series from the New Zealand Coal Band covering diagenetic to catagenetic coalification levels. *Organic Geochemistry,* vol. 40, pp. 1063-1073.

Grosse, G., Romanovsky, V., Jorgenson, T., Walter Anthony, K., Brown, J. and Overduin, P.P. (2011). Vulnerability and feedbacks of permafrost to climate change. *Eos,* vol. 92, pp. 73.74.

Grosse, G., Jones, B. and Arp, C. (2013). Thermokarst lakes, drainage, and drained basins. In: Shroder, J. (Editor in Chief), Giardino, R., Harbor, J. (Eds.), Treatise on Geomorphology. Academic Press, San Diego, CA, vol. 8, *Glacial and Periglacial Geomorphology*, pp. 325-353.

Hansen, J., Sato, M. and Ruedy, R. (1997). Radiative forcing and climate response. *Journal of Geophysical Research*, vol. 102, pp. 6831-6864.

Hopkins, D.M. and Kidd, J.G. (1988). Thaw lake sediments and sedimentary environments. *Proceedings of the Fifth International Conference on Permafrost*, Trondheim, pp. 790–795.

Hopmans, E.C., Weijers, J.W.H., Schefuß, E., Herfort, L., Sinninghe Damsté, J.S. and Schouten, S. (2004). A novel proxy for terrestrial organic matter in sediments based on branched and isoprenoid tetraether lipids. *Earth and Planetary Science Letters,* vol. 224, pp. 107-116.

Hugelius, G., Strauss, J., Zubrzycki, S., Harden, J.W., Schuur, E.A.G., Ping, C.-L., Schirrmeister, L., Grosse, G., Michaelson, G.J., Koven, C.D., O'Donnell, J.A., Elberling, B., Mishra, U., Camill, P., Yu, Z., Palmtag, J. and Kuhry, P. (2014). Estimated stocks of circumpolar permafrost carbon with quantified uncertainty ranges and identified data gaps. *Biogeosciences,* vol. 11, pp. 6573-6593.

Huston, M.M., Brigham-Grette, J. and Hopkins, D.M. (1990). Paleogeographic significance of middle Pleistocene glaciomarine deposits on Baldwin peninsula, northwest Alaska. *Annals of Glaciology*, vol. 14, pp. 111-114.

IPCC (2014). *Climate Change: Synthesis Report. Contribution of Working Groups I, II and III to the Fifth Assessment Report of the Intergovernmental Panel on Climate Change* [Core Writing Team, R.K. Packauri and L.A. Meyer (eds.)]. IPCC, Geneva, Switzerland, 151 pp.

Jones, B.M., Grosse, G., Arp, C.D., Jones, M.C., Walter Anthony, K.M. and Romanovsky, V.E. (2011). Modern thermokarst lake dynamics in the continuous permafrost zone, northern Seward Peninsula, Alaska. *Journal of Geophysical Research*, vol. 116, pp. 1-13.

Jones, M.C., Grosse, G., Jones, B.M. and Walter Anthony, K.M. (2012). Peat accumulation in drained thermokarst lake basins in continuous, ice-rich permafrost, northern Seward Peninsula, Alaska. *Journal of Geophysical Research,* vol. 117.

Kanevskiy, M., Shur, Y., Fortier, D., Jorgenson, M.T., Stephani, E. (2011). Cryostratigraphy of late Pleistocene syngenetic permafrost (yedoma) in northern Alaska, Itillik River exposure. *Quaternary Research*, vol. 75, pp. 584-596.

Killops, S.D. and Killops, V.J. (2009). Introduction to organic geochemistry. John Wiley and Sons.

Knoblauch, C., Beer, C., Sosnin, A., Wagner, D. and Pfeiffer, E. (2013). Predicting long-term carbon mineralization and trace gas production from thawing permafrost of Northeast Siberia. *Global Change Biology,* vol. 19, pp. 1160-1172.

Lascu, I. (2009). Magnetic susceptibility logging for cores. Limnological Research Center Core Facility, SOP series. Retrieved at 31-01-2017 from: lrc.geo.umn.edu/laccore/assets/pdf/sops/susceptibility.pdf

Lenz, J., Grosse, G., Jones, B.M., Walter Anthony, K.M., Bobrov, A., Wulf, S. and Wetterich, S. (2016a). Mid-Wisconsin to Holocene Permafrost and Landscape Dynamics based on a Drained Lake Basin Core from the Northern Seward Peninsula, Northwest Alaska. *Permafrost and Periglacial Processes*, vol. 27, pp. 56-75.

Lenz, J., Jones, B.M., Wetterich, S., Tjallingii, R., Fritz, M., Arp, C.D., Rudaya, N. and Grosse, G. (2016b). Impacts of shore expansion and catchment characteristics on lacustrine thermokarst records in permafrost lowlands, Alaska Arctic Coastal Plain. *Arktos,* 2:25.

Lenz, J., Wetterich, S., Jones, B.M., Meyer, H., Bobrov, A and Grosse, G. (2016c). Evidence of multiple thermokarst lake generations from an 11800-year-old permafrost core on the northern Seward Peninsula, Alaska. *Boreas,* vol. 45, pp. 584-603.

Lenz, J., Fuchs, M., Nitze, I., Strauss, J., Grosse, G. (in prep). The Expedition of ERC group PETA-CARB “West-Alaska 2016”. In preparation for Berichte zur Polar- und Meeresforschung (in English).

Marzi, R., Torkelson, B.E. and Olson, R.K. (1993). A revised carbon preference index. *Organic Geochemistry,* vol. 20, pp. 1303-1306.

Meyers, P.A. (1994). Preservation of elemental and isotopic source identification of sedimentary organic matter. *Chemical Geology,* vol. 114, pp. 289-302.

Meyers, P.A. (1997). Organic geochemical proxies of paleoceanographic, paleolimnologic and paleoclimatic processes. *Organic Geochemistry,* vol. 27, pp. 213-250.

Meyers, P.A. (2003). Applications of organic geochemistry to paleolimnological reconstructions: a summary of examples from the Laurentian Great Lakes. *Organic Geochemistry,* vol. 34, pp. 261-289.

Morgenstern, A., Grosse, G., Günther, F., Fedorova, I. and Schirrmeister, L. (2011). Spatial analyses of thermokarst lakes and basins in Yedoma landscapes of the Lena Delta. *The Cryosphere,* vol. 5, pp. 849-867.

Murton, J.B., Goslar, T., Edwards, M.E., Bateman, M.D., Danilov, P.P., Savvinov, G.N., Gubin, S.V., Ghaleb, B., Haile, J., Kanevskiy, M., Lozhkin, A.V., Lupachev, A.V., Murton, D.K., Shur, Y., Tikhonov, A., Vasil’chuk, A.C., Vasilçhuk, Y.K. and Wolfe, S.A. (2015). Palaeoenvironmental interpretation of yedoma silt (Ice Complex) deposition as cold-climate loess, Duvanny Yar, Northeast Siberia. *Permafrost and Periglacial Processes,* vol. 26, pp. 208-288.

Peters, K.E., Walters, C.C. and Moldowan, J.M. (2007). The Biomarker Guide. Second Edition, Volume 1. US, New York: Cambridge University Press.

Peterse, F., Van der Meer, J., Schouten, S., Weijers, J.W.H., Fiere, N., Jackson, R.B., Kim, J., Damsté, J.S.S. (2012). Revised calibration of the MBT-CBT paleotemperature proxy based on branched tetraether membrane lipids in surface soils. *Geochimica et Cosmochimica Acta,* vol. 96, pp. 215-229.

Peterse, F., Vonk, J.E., Holmes, R.M., Giosan, L., Zimov, N. and Eglinton, T.I. (2014). Branched glycerol diaklyl glycerol tetraethers in Arctic lake sediments: Sources and implications for paleothermometry at high latitudes. *Journal of Geophysical Research: Biogeosciences*, vol. 119, pp. 1738-1754.

Poynter, J. and Eglinton, G. (1990). 14. Molecular composition of three sediments from hole 717C: the Bengal fan. *Proceedings of the Ocean Drilling Program, Scientific Results*, vol. 116.

Pushkar, V.S., Roof, S.R., Cherepanova, M.V., Hopkins, D.M. and Brigham-Grette, J. (1999). Paleogeographic and paleoclimatic significance of diatoms from middle Pleistocene marine and glaciomarine deposits on Baldwin Peninsula, northwestern Alaska. *Paleogeography, Palaeoclimatology, Palaeoecology,* vol. 152, pp. 67-85.

Radke, M., Willsch, H. and Welte, D.H. (1980). Preparative hydrocarbon group type determination by automated medium pressure liquid chromatography. *Analytical Chemistry*, vol. 52, pp. 406-411.

Reimer, P.J., Bard, E., Bayliss, A., Beck, J.W., Blackwell, P.G., Bronk Ramsey, C. et al. (2013). IntCal13 and Marine13 radiocarbon age calibration curves 0-50,000 years cal BP. *Radiocarbon,* vol. 55, pp. 1869-1887.

Schirrmeister, L., Meyer, H., Wetterich, S. and Siegert, C. (2008). The Yedoma Suite of the northeastern Siberian Shelf region: Characteristics and concept of formation. *Ninth International Conference on Permafrost*, pp. 1595-1600.

Schirrmeister, L., Grosse, G., Wetterich, S., Overduin, P., Strauss, J., Schuur, E.A.G. and Hubberten, H. (2011). Fossil organic matter characteristics in permafrost deposits of the northeast Siberian Arctic. *Journal of Geophysical Research*, vol. 116, pp. 1-16.

Schirrmeister, L., Froese, D., Tumskoy, V., Grosse, G. and Wetterich, S. (2013). Yedoma: Late Pleistocene ice-rich syngetic permafrost in Beringia. *Encyclopedia of Quaternary Science,* vol. 3, pp. 542-552.

Schirrmeister, L., Meyer, H., Andreev, A., Wetterich, S., Kienast, F., Bobrov, A., Fuchs, M., Sierralta, M. and Herzschuh, U. (2016). Late Quaternary paleoenvironmental records from the Chatanika River valley near Fairbanks (Alaska). *Quaternary Science Reviews,* vol. 147, pp. 259-278.

Schulte, S., Mangelsdorf, K. and Rullkötter, J. (2000). Organic matter preservation on the Pakistan continental margin as revealed by biomarker geochemistry. *Organic Geochemistry,* vol. 31, pp. 1005-1022.

Schuur, E.A.G., Bockheim, J., Canadell, J.G., Euskirchen, E., Field, C.B. and Goryachkin, S.V. (2008). Vulnerability of permafrost carbon to climate change: implications for the global carbon cycle. *BioScience,* vol. 58, pp. 701-714.

Schuur, E.A.G., McGuire, A.D., Schädel, C., Grosse, G., Harden, J.W., Hayes, D.J., et al. (2015). Climate change and the permafrost carbon feedback. *Nature,* vol. 520, pp. 171-179.

Sher, A.V. (1997). Yedoma as a store of paleoenvironmental records in Beringida. In *Beringia Palaeoenvironmental Workshop September 1997,* Elias S and Bringham-Grette J (eds), pp. 92-94. Ohana Productions_ Nepean, ON, Canada.

Shur, Y.L. and Jorgenson, M.T. (1998). Cryostructure development on the floodplain of the Colville River Delta, northern Alaska. *Permafrost, Proceedings of 7th International Conference,* Yellowknife, Canada, pp. 993-999.

Shur, Y.L. and Jorgenson, M.T. (2007). Patterns of Permafrost Formation and Degradation in Relation to Climate and Ecosystems. *Permafrost and Periglacial Processes,* vol. 18, pp. 7-19.

Shur, Y., Kanevskiy, M., Jorgenson, T., Dillon, M., Stephani, E. and Bray, M. (2012). Permafrost degradation and thaw settlement under lakes in yedoma environment. *Tenth International Conference on Permafrost*.

Stapel, J.G., Schirrmeister, L., Overduin, P.P., Wetterich, S., Strauss, J., Horsfield, B. and Mangelsdorf, K. (2016). Microbial lipid signatures and substrate potential of organic matter in permafrost deposits: Implications for greenhouse gas production. *Journal of Geophysical Research: Biogeosciences*, vol. 121.

Strauss, J., Schirrmeister, L., Wetterich, S., Borchers, A. and Davydov, S.P. (2012). Grain-size properties and organic-carbon stock of Yedoma Ice Complex permafrost from the Kolyma lowland, northeastern Siberia. *Global Biogeochemical Cycles,* vol. 26, GB3003.

Strauss, J., Schirrmeister, L., Grosse, G., Wetterich, S., Ulrich, M., Herzschuh, U. and Hubberten, H. (2013). The deep permafrost carbon pool of the Yedoma region in Siberia and Alaska. *Geophysical Research Letters,* vol. 40, pp. 6165-6170.

Strauss, J., Schirrmeister, L., Mangelsdorf, K., Eichhorn, L., Wetterich, S. and Herschuh, U. (2015). Organic-matter quality of deep permafrost carbon – a study from Arctic Siberia. *Biogeosciences,* vol. 12, pp. 2227-2245.

Strauss, J., Laboor, S., Fedorov, A.N., Fortier, D., Froese, D., Fuchs, M., Grosse, G., Günther, F., Harden, J.W., Hugelius, G., Kanevskiy, M.Z., Kholodov, A.L., Kunitsky, V.V., Kraev, G., Lapointe-Elmrabti, L., Lozhkin, A.V., Rivkina, E., Robinson, J., Schirrmeister, L., Shmelev, D., Shur, Y., Siegert, C., Spektor, V., Ulrich, M., Vartanyan, S.L., Veremeeva, A., Walter Anthony, K.M. and Zimov, S.A. (2016). Database of Ice-Rich Yedoma Permafrost (IRYP). doi:10.1594/PANGAEA.861733

Stuiver, M., Reimer, P.J., and Reimer, R.W. (2017). CALIB 7.1 [WWW program] at http://calib.org, accessed 2017-4-21.

Thompson, R., Battarbee, R.W., O'Sullivan, P.E. and Oldfield, F. (1975). Magnetic susceptibility of lake sediments. *Limnology and Oceanography*, vol. 20, pp. 687-698.

Ulrich, M., Grosse, G., Strauss, J. and Schirrmeister, L. (2014). Quantifying wedge-ice volumes in yedoma and thermokarst basin deposits. *Permafrost and Periglacial Processes,* vol. 25, pp. 151-161.

UNEP (2010). Global environmental outlook 3 CBD Technical Secretariat of the Convention on Biodiversity.

US Climate Data (2017). Climate Kotzebue – Alaska. http://www.usclimatedata.com/climate/kotzebue/alaska/united-states/usak0135/2017/1. Accessed 2017-03-08.

van Everdingen, R.O. (Ed.) Multi-Language Glossary of Permafrost and Related Ground-Ice Terms, revised May 2005 1998 National Snow and Ice Data Center/ World Data Center for Glaciology, Boulder, CO.

Vasil'chuk, Y.K. and Vasil'chuk, A.C. (2017). Validity of radiocarbon ages of Siberian yedoma. *GeoResJ,* vol. 13, pp. 83-95.

Vonk, J.E., Mann, P.J., Davydov, S., Davydova, A., Spencer, R.G.M., Schade, J., Sobczak, W.V., Zimov, N., Zimov, S., Bulygina, E., Eglinton, T.I. and Holmes, R.M. (2013). High biolability of ancient permafrost carbon upon thaw. *Geophysical Research Letters,* vol. 40, pp. 2689-2693.

Vonk, J.E., Tank, S.E., Bowden, W.B., Laurion, I., Vincent, W.F. et al. (2015). Reviews and syntheses: Effects of permafrost thaw on Arctic aquatic ecosystems. *Biogeosciences,* vol. 12, pp. 7129-7167.

Walter Anthony, K.M., Zimov, S.A., Grosse, G., Jones, M.C., Anthony, P.M., Chapin III, F.S., Finlay, J.C., Mack, M.C., Davydov, S., Frenzel, P. and Frolking, S. (2014). A shift of thermokarst lakes from carbon sources to sinks during the Holocene epoch. *Nature,* vol. 511, pp. 452-456.

Walthert, L., Zimmerman, S., Blaser, P., Luster, J. and Lüscher, P. (2004). Waldböden der Schweiz. Band 1: Grundlagen und Region Jura. Birmensdorf: Eidgenöss Forschungsanstalt Wald Schnee Landschaft, pp. 768.

Washburn, A. L. (1979). *Geocryology: A Survey of Periglacial Processes and Environments*. London: Edward Arnold.

Weijers, J.W.H., Schouten, S., Van den Donker, J.C., Hopmans, E.C., Damsté, J.S.S. (2007). Environmental controls on bacterial tetraether membrane lipid distribution in soils. *Geochimica et Cosmochimica Acta,* vol. 71, pp. 703-713.

Wetterich, S., Grosse, G., Schirrmeister, L., Andreev, A.A., Bobrov, A.A., Kienast, F., Bigelow, N.H. and Edwards, M.E. (2012). Late Quaternary environmental and landscape dynamics revealed by a pingo sequence on the northern Seward Peninsula, Alaska. *Quaternary Science Reviews,* vol. 39, pp. 26-44.

Wetterich, S., Tumskoy, V., Rudaya, N., Andreev, A.A., Opel, T., Meyer, H., Schirrmeister, L. and Hüls, M. (2014). Ice Complex formation in arctic East Siberia during the MIS3 Interstadial. *Quaternary Science Reviews,* vol. 84, pp. 39-55.

Zaiontz, C. (2013). Real Statistics using Excel. http://www.real-statistics.com/one-way-analysis-of-variance-anova/kruskal-wallis-test/ . Accessed 2017-03-14.

Zhang, T., Heginbottom, J.A., Barry, R.G. and Brown, J. (2000). Further statistics on the distribution of permafrost and ground ice in the Northern Hemisphere. *Polar Geography*, vol. 24, pp. 126-131.

Zhou, W., Zheng, Y., Meyers, P.A., Jull, A.J.T. and Xie, S. (2010). Postglacial climate-change record in biomarker lipid compositions of the Hani peat sequence, Northeastern China. *Earth and Planetary Science Letters,* vol. 294, pp. 37-46.

Zimov, S.A., Schuur, E.A.G. and Chapin III, F.S. (2006a). Permafrost and the global carbon budget. *Science,* vol. 312, pp. 1612-1613.

Zimov, S.A., Davydov, S.P., Zimova, G.M., Davydova, A.I., Schuur, E.A.G., Dutta, K. and Chapin III, F.S. (2006b). Permafrost carbon: Stock and decomposability of a globally significant carbon pool. *Geophysical Research Letters,* vol. 33.

A. Appendix

Table A.1: Raw data of cryological, sedimentological and biochemical parameters.

Sample ID	Depth	Magn. suscep.	Absolute ice content	Bulk density	TN	TC	TOC	TOC/TN	δ^{13}C	Vol. C$_{org}$ content	Clay	Silt	Sand	Mean grain size
	[cm]	SI-system	[wt%]	[10^3 kg m^{-3}]	[wt%]	[wt%]	[wt%]		[‰]	[kg m^{-3}]	[vol%]	[vol%]	[vol%]	[µm]
BAL16-B2-20	620	56.0	42.9	0.83	0.1	2.2	1.4	9.5	-25.0	11.7	0.0	0.8	0.2	22.2
BAL16-B2-21	638	58.5	46.7	0.75	0.2	2.4	1.6	10.1	-25.4	11.8	0.0	0.8	0.2	29.1
BAL16-B2-22	673	58.7	45.2	0.78	0.2	3.0	2.0	10.8	-25.4	15.4	0.0	0.8	0.2	26.3
BAL16-B2-23	730	55.2	38.9	0.93	0.2	4.1	2.9	13.1	-25.7	26.6	0.0	0.8	0.1	23.3
BAL16-B2-24	810	42.7	37.1	0.98	0.2	3.0	2.0	11.4	-25.6	19.5	0.0	0.8	0.2	29.2
BAL16-B2-25	920	55.1	47.3	0.73	0.1	2.4	1.4	9.7	-25.4	10.6	0.0	0.8	0.1	23.2
BAL16-B2-26	945	66.7	49.7	0.68	0.3	4.7	3.6	10.4	-26.3	24.6	0.0	0.8	0.2	26.5
BAL16-B2-27	965	61.8	47.1	0.74	0.4	2.8	1.6	4.4	-26.1	12.1	0.0	0.8	0.2	30.4
BAL16-B2-28	1065	44.0	36.2	1.00	0.7	1.4	< 0.1	n/a	n/a	4.5	0.0	0.8	0.2	29.4
BAL16-B2-29	1080	51.2	37.6	0.96	< 0.1	1.3	0.7	7.9	-24.8	6.9	0.0	0.8	0.1	23.1
BAL16-B2-30	1097	47.4	35.5	1.02	< 0.1	1.6	0.7	8.2	-25.0	7.6	0.0	0.8	0.2	28.0
BAL16-B2-31	1117	52.8	36.2	1.00	< 0.1	1.4	0.7	8.1	-25.1	7.3	0.0	0.8	0.2	29.8
BAL16-B2-32	1142	44.5	39.2	0.92	< 0.1	1.8	1.0	10.9	-25.3	9.0	0.0	0.8	0.2	33.2
BAL16-B2-33	1242	45.8	42.4	0.84	< 0.1	1.9	1.0	10.6	-24.8	8.1	0.0	0.8	0.2	25.3
BAL16-B2-34	1265	34.5	41.3	0.87	0.2	3.1	2.1	13.0	-25.6	18.1	0.0	0.8	0.2	27.6
BAL16-B2-35	1290	31.3	43.8	0.81	0.2	3.3	2.5	13.6	-26.0	20.0	0.0	0.8	0.1	25.2
BAL16-B2-36	1314	26.0	37.2	0.97	0.2	3.2	2.3	13.1	-25.9	22.1	0.0	0.8	0.2	31.9
BAL16-B2-37	1331	31.4	45.7	0.77	0.2	4.2	3.2	14.0	-26.1	24.7	0.0	0.8	0.2	24.9
BAL16-B2-38	1366	53.4	66.0	0.40	0.4	5.7	4.7	12.2	-26.3	18.8	0.0	0.8	0.1	20.5
BAL16-B2-39	1399	36.8	54.5	0.59	0.1	1.8	1.6	12.6	-27.9	9.6	0.1	0.8	0.1	15.9
BAL16-B2-1	1500	32.5	48.6	0.71	0.4	4.9	4.3	11.8	-26.9	30.6	0.0	0.8	0.1	21.0
BAL16-B2-2	1525	35.1	50.8	0.66	0.2	3.0	2.7	11.0	-27.1	17.9	0.0	0.8	0.1	18.3
BAL16-B2-3	1555	54.5	69.1	0.35	0.3	3.1	2.9	11.5	-28.3	10.2	0.1	0.9	0.1	14.7
BAL16-B2-4	1594	70.0	52.0	0.64	0.2	1.4	1.3	7.8	-26.5	8.4	0.0	0.9	0.1	17.9
BAL16-B2-5	1600	70.6	39.2	0.92	0.2	2.2	1.6	8.8	-25.4	15.1	0.1	0.8	0.1	17.0

Sample ID	**Depth**	**Magn. suscep.**	**Absolute ice content**	**Bulk density**	**TN**	**TC**	**TOC**	**TOC/TN**	**δ^{13}C**	**Vol. C_{org} content**	**Clay**	**Silt**	**Sand**	**Mean grain size**
	[cm]	**SI-system**	**[wt%]**	**[10^3 kg m^{-3}]**	**[wt%]**	**[wt%]**	**[wt%]**		**[‰]**	**[kg m^{-3}]**	**[vol%]**	**[vol%]**	**[vol%]**	**[µm]**
BAL16-B2-40	1700	80.5	39.0	0.93	0.1	1.6	1.0	10.1	-26.2	9.5	0.1	0.9	0.0	13.0
BAL16-B2-41	1750	85.6	57.9	0.53	< 0.1	1.3	0.9	9.5	-25.9	4.5	0.1	0.9	0.0	8.8
BAL16-B2-42	1870	59.6	34.2	1.06	< 0.1	1.6	0.9	9.6	-26.1	9.1	0.1	0.8	0.1	13.8
BAL16-B3-1	5	13.9	70.6	0.33	1.5	46.8	37.3	24.8	-27.6	123.8	0.1	0.8	0.1	18.0
BAL16-B3-2	25	10.0	41.0	0.88	0.5	14.0	11.4	24.9	-27.8	99.8	0.0	0.8	0.2	23.2
BAL16-B3-3	50	9.8	42.5	0.84	0.5	11.4	11.4	23.4	-27.5	96.3	0.0	0.9	0.1	17.8
BAL16-B3-4	58	20.9	81.6	0.19	1.4	38.9	30.7	22.2	-27.3	58.8	0.0	0.9	0.1	16.2
BAL16-B3-5	84	26.4	82.6	0.18	1.3	49.3	39.0	30.8	-27.6	70.0	0.0	0.9	0.1	13.7
BAL16-B3-6	106	30.2	64.4	0.42	0.3	7.2	5.9	18.4	-27.7	25.2	0.0	0.8	0.2	27.6
BAL16-B3-7	135	19.7	43.9	0.81	0.3	5.7	4.9	19.0	-27.7	39.8	0.0	0.8	0.2	23.9
BAL16-B3-8	170	37.2	63.3	0.44	0.5	7.6	6.3	12.9	-27.1	27.6	0.1	0.9	0.1	16.1
BAL16-B3-9	200	42.7	64.2	0.43	0.1	1.5	1.4	11.6	-27.1	5.8	0.1	0.9	0.1	14.9
BAL16-B4-1	0	10.8	70.9	0.33	1.5	53.5	42.3	29.0	-28.7	139.2	0.0	0.7	0.2	24.5
BAL16-B4-2	8	13.8	74.1	0.29	1.9	48.9	38.9	20.2	-27.6	110.9	0.0	0.8	0.2	22.9
BAL16-B4-3	38	19.4	46.5	0.75	0.4	8.8	7.5	19.1	-28.7	56.1	0.1	0.9	0.0	12.1
BAL16-B4-4	120	36.6	63.8	0.43	0.5	9.8	8.0	15.9	-28.3	34.7	0.1	0.9	0.1	15.1
BAL16-B4-5	140	19.3	52.7	0.63	0.5	9.4	7.8	17.1	-28.0	49.0	0.1	0.9	0.0	13.9
BAL16-B4-6	160	20.4	61.8	0.47	0.5	10.8	8.6	16.9	-28.3	40.0	0.0	0.9	0.1	15.4
BAL16-B4-7	190	22.3	53.6	0.61	0.4	7.9	6.3	16.8	-28.1	38.5	0.1	0.8	0.1	19.0
BAL16-B4-8	215	25.2	50.3	0.67	0.4	7.1	5.7	16.4	-27.7	38.6	0.0	0.9	0.1	16.3
BAL16-B4-9	250	25.1	41.8	0.86	0.3	4.9	5.4	17.0	-27.8	46.8	0.1	0.9	0.1	16.3
BAL16-B4-10	280	25.1	28.0	1.25	0.1	1.6	1.7	13.9	-26.5	21.2	0.0	0.7	0.3	31.1
BAL16-B4-11	300	25.9	29.8	1.19	0.1	1.7	1.7	13.3	-26.5	20.4	0.0	0.7	0.3	35.1
BAL16-B4-12	320	25.5	32.2	1.11	0.2	2.2	2.3	14.6	-26.5	25.8	0.0	0.7	0.2	32.2
BAL16-B4-13	320	25.9	33.5	1.08	0.2	2.4	2.4	13.2	-26.6	25.4	0.0	0.8	0.2	27.5
BAL16-B4-14	340	21.6	33.1	1.09	0.2	2.1	2.2	13.6	-26.5	23.9	0.0	0.8	0.2	31.0

Sample ID	Depth	Magn. suscep.	Absolute ice content	Bulk density	TN	TC	TOC	TOC/TN	δ^{13}C	Vol. C_{org} content	Clay	Silt	Sand	Mean grain size
	[cm]	SI-system	[wt%]	[10^3 kg m^{-3}]	[wt%]	[wt%]	[wt%]		[‰]	[kg m^{-3}]	[vol%]	[vol%]	[vol%]	[µm]
BAL16-B4-15	355	30.6	29.4	1.20	0.1	2.0	2.1	14.9	-26.7	24.9	0.0	0.7	0.3	42.0
BAL16-B4-16	385	35.1	27.2	1.27	0.1	1.6	1.7	12.3	-26.4	21.5	0.0	0.8	0.2	34.1
BAL16-B4-17	410	16.7	34.1	1.06	0.3	3.4	3.7	13.0	-26.8	39.3	0.0	0.8	0.2	28.0
BAL16-B4-18	430	17.4	35.6	1.02	0.3	3.9	4.0	13.9	-26.6	40.6	0.0	0.9	0.1	19.9
BAL16-B4-19	445	18.0	37.9	0.95	0.3	4.6	4.9	14.4	-27.0	47.0	0.0	0.9	0.1	22.3
BAL16-B4-20	453	17.4	35.8	1.01	0.3	4.3	4.3	13.5	-26.9	43.0	0.0	0.9	0.1	21.1
BAL16-B4-21	488	18.5	38.3	0.95	0.4	6.7	5.9	16.3	-27.4	55.4	0.0	0.9	0.1	22.1
BAL16-B4-22	528	13.6	36.3	1.00	0.4	4.2	4.2	11.3	-27.1	41.5	0.0	0.9	0.1	22.1
BAL16-B4-23	553	21.3	37.9	0.96	0.3	4.0	4.3	16.6	-26.7	40.7	0.0	0.9	0.1	17.2
BAL16-B4-24	583	18.1	39.1	0.93	0.5	5.1	5.3	11.5	-27.0	49.1	0.0	0.8	0.1	19.2
BAL16-B4-25	618	26.6	38.5	0.94	0.5	5.4	5.5	12.1	-26.9	51.6	0.0	0.9	0.1	21.5
BAL16-B4-26	638	20.0	35.6	1.02	0.3	5.1	5.3	18.3	-27.5	53.6	0.0	0.8	0.1	20.7
BAL16-B4-27	668	26.0	35.7	1.01	0.2	2.9	3.0	14.7	-26.3	30.1	0.0	0.8	0.2	24.3
BAL16-B4-28	708	28.1	103.9	n/a	0.2	1.7	1.9	11.5	-25.8	n/a	0.0	0.9	0.1	22.7
BAL16-B4-29	748	20.5	37.5	0.97	0.3	4.5	4.8	14.6	-27.0	46.6	0.0	0.8	0.2	26.7
BAL16-B4-30	768	25.0	32.2	1.11	0.1	1.7	1.7	13.5	-26.6	18.9	0.0	0.7	0.2	33.0
BAL16-B4-31	798	68.5	28.2	1.24	< 0.1	1.0	< 0.1	n/a	n/a	1.1	0.1	0.8	0.1	15.3
BAL16-B5-1	0	22.2	72.9	0.30	1.0	37.9	37.0	35.4	-27.9	111.5	n/a	n/a	n/a	n/a
BAL16-B5-2	16	14.3	73.2	0.30	1.4	30.9	29.6	20.7	-26.9	87.9	n/a	n/a	n/a	n/a
BAL16-B5-3	30	9.9	46.5	0.75	0.5	13.4	13.6	26.4	-27.7	102.4	0.1	0.9	0.1	15.8
BAL16-B5-4	82	97.4	62.5	0.45	0.1	2.0	1.6	13.1	-25.9	7.4	0.0	0.8	0.1	18.6
BAL16-UPL1-L1-1	1	n/a	n/a	0.41	0.7	13.7	14.1	21.6	-28.8	57.1	n/a	n/a	n/a	n/a
BAL16-UPL1-L1-1	2	n/a	n/a	0.41	0.7	13.7	14.1	21.6	-28.8	57.1	n/a	n/a	n/a	n/a
BAL16-UPL1-L1-2	4	n/a	n/a	0.43	0.6	14.2	14.0	22.1	-28.7	60.3	n/a	n/a	n/a	n/a
BAL16-UPL1-L1-2	5	n/a	n/a	0.43	0.6	14.2	14.0	22.1	-28.7	60.3	n/a	n/a	n/a	n/a
BAL16-UPL1-L1-3	7	n/a	n/a	0.41	0.7	14.9	15.1	22.3	-28.7	61.5	n/a	n/a	n/a	n/a

Sample ID	Depth [cm]	Magn. suscep. SI-system	Absolute ice content [wt%]	Bulk density [10^3 kg m^{-3}]	TN [wt%]	TC [wt%]	TOC [wt%]	TOC/TN	$\delta^{13}C$ [‰]	Vol. C_{org} content [kg m^{-3}]	Clay [vol%]	Silt [vol%]	Sand [vol%]	Mean grain size [µm]
BAL16-UPL1-L1-3	8	n/a	n/a	0.41	0.7	14.9	15.1	22.3	-28.7	61.5	n/a	n/a	n/a	n/a
BAL16-UPL1-L1-4	10	n/a	n/a	0.43	0.6	14.0	13.9	23.6	-28.5	60.5	n/a	n/a	n/a	n/a
BAL16-UPL1-L1-4	11	n/a	n/a	0.43	0.6	14.0	13.9	23.6	-28.5	60.5	n/a	n/a	n/a	n/a
BAL16-UPL1-L1-5	13	n/a	n/a	0.41	0.7	14.6	14.7	22.1	-28.5	60.5	n/a	n/a	n/a	n/a
BAL16-UPL1-L1-5	14	n/a	n/a	0.41	0.7	14.6	14.7	22.1	-28.5	60.5	n/a	n/a	n/a	n/a
BAL16-UPL1-L1-6	16	n/a	n/a	0.43	0.7	15.1	15.2	22.1	-28.4	64.6	n/a	n/a	n/a	n/a
BAL16-UPL1-L1-6	17	n/a	n/a	0.43	0.7	15.1	15.2	22.1	-28.4	64.6	n/a	n/a	n/a	n/a
BAL16-UPL1-L1-7	18	n/a	n/a	0.43	0.6	14.5	14.5	23.0	-28.3	62.6	n/a	n/a	n/a	n/a
BAL16-UPL1-L1-7	19	n/a	n/a	0.43	0.6	14.5	14.5	23.0	-28.3	62.6	n/a	n/a	n/a	n/a
BAL16-UPL1-L1-8	22	n/a	n/a	0.44	0.6	13.8	13.8	22.6	-28.5	60.9	n/a	n/a	n/a	n/a
BAL16-UPL1-L1-8	23	n/a	n/a	0.44	0.6	13.8	13.8	22.6	-28.5	60.9	n/a	n/a	n/a	n/a
BAL16-UPL1-L1-9	25	n/a	n/a	0.42	0.6	14.4	14.7	22.8	-28.4	61.6	n/a	n/a	n/a	n/a
BAL16-UPL1-L1-9	26	n/a	n/a	0.42	0.6	14.4	14.7	22.8	-28.4	61.6	n/a	n/a	n/a	n/a

Table A.2: n-alkane concentrations [μg g^{-1} TOC].

Sample ID	Ext. ID	nC14	nC15	nC16	nC17	nC18	nC19	nC20	nC21	nC22	nC23	nC24	nC25	nC26	nC27	nC28	nC29	nC30	nC31	nC32	nC33	nC34	nC35
BAL16-B2-20	G016921	0.0	0.0	0.0	1.8	8.2	5.2	12.7	21.5	17.1	50.0	19.1	86.9	16.8	179.3	17.3	233.8	12.8	166.1	4.8	18.0	0.0	1.6
BAL16-B2-26	G016922	0.1	0.1	1.3	1.5	4.8	2.2	5.0	16.5	6.5	31.4	8.9	52.1	7.5	101.5	8.1	138.1	5.9	123.9	3.4	25.4	0.0	0.9
BAL16-B2-31	G016923	0.0	0.0	0.0	0.0	3.9	4.6	10.2	12.4	13.7	31.4	14.7	51.6	15.4	128.4	21.0	451.6	39.9	873.0	25.7	140.4	0.0	4.9
BAL16-B2-39	G016924	5.7	7.4	25.1	28.9	32.4	11.5	17.4	27.6	19.3	48.1	21.3	91.2	22.3	256.5	28.4	272.1	16.5	228.7	12.5	74.3	2.2	3.9
BAL16-B2-1	G016919	0.5	0.3	1.3	0.8	2.5	1.4	2.8	7.2	5.5	18.8	8.2	33.3	9.8	87.7	14.6	306.1	9.1	139.8	3.3	31.4	0.0	4.0
BAL16-B2-5	G016920	0.6	0.7	4.3	4.9	11.5	5.8	12.0	28.9	17.2	52.2	19.1	85.6	15.9	168.6	18.3	220.6	13.0	256.6	8.2	80.5	0.0	5.4
BAL16-B4-2	G016925	0.0	0.0	0.1	0.3	0.9	2.5	3.6	31.3	10.0	44.1	14.4	81.5	15.4	237.5	17.1	197.3	10.1	255.0	7.9	52.4	0.0	1.0
BAL16-B4-4	G016926	0.4	0.0	1.8	6.3	8.8	29.6	26.9	142.1	71.1	257.2	75.3	280.3	67.1	548.5	67.3	584.4	49.2	810.6	37.3	211.0	4.6	6.7
BAL16-B4-6	G016927	0.0	0.0	1.0	8.6	9.9	29.6	29.2	154.7	70.6	257.6	73.0	293.8	60.9	491.7	66.2	603.3	47.4	903.1	39.6	201.4	6.5	6.5
BAL16-B4-14	G016928	0.3	0.0	1.8	4.4	5.6	9.6	14.9	54.7	38.1	115.3	42.5	163.7	40.6	342.1	40.4	473.0	29.3	591.4	18.9	150.0	0.0	6.0
BAL16-B4-18	G016929	0.0	0.0	0.0	0.8	2.0	9.3	19.7	74.3	69.9	208.1	79.4	292.9	68.9	559.9	47.4	459.9	23.7	344.8	12.4	78.9	0.0	6.5
BAL16-B4-24	G016930	0.0	0.0	0.2	1.5	3.5	10.3	15.4	51.9	40.1	126.7	48.8	214.5	42.6	389.4	32.7	301.2	16.7	251.8	9.3	55.2	0.0	4.0
BAL16-B4-31	G016931	0.0	0.0	0.0	0.0	65.6	125.9	329.8	397.3	502.9	1019.3	614.6	1621.4	590.6	2987.6	421.0	3111.1	269.6	3082.7	164.7	984.8	155.6	0.0

Table A.3: brGDGT concentrations [ng g^{-1} TOC].

Sample ID	Ext. ID	brGDGT IIIa	brGDGT IIIb	brGDGT IIIc	brGDGT Iia	brGDGT IIb	brGDGT IIc	brGDGT Ia	brGDGT Ib	brGDGT Ic
BAL16-B2-20	G016921	82.4	4.0	0.0	90.2	29.2	0.0	39.1	9.2	0.0
BAL16-B2-26	G016922	56.9	0.0	0.0	58.1	20.3	0.0	24.5	6.6	0.0
BAL16-B2-31	G016923	n/a	n/a	n/a	n/a	n/a	n/a	n/a	n/a	n/a
BAL16-B2-39	G016924	233.2	0.0	0.0	449.2	87.4	8.3	379.4	107.5	11.8
BAL16-B2-1	G016919	82.6	6.7	0.0	104.8	40.6	0.0	41.8	15.4	0.0
BAL16-B2-5	G016920	303.1	0.0	0.0	202.0	71.3	0.0	85.2	39.8	0.0
BAL16-B4-2	G016925	220.9	0.0	0.0	239.1	0.0	0.0	148.2	5.5	0.0
BAL16-B4-4	G016926	926.1	24.4	0.0	1146.3	109.2	16.8	690.1	106.5	17.4
BAL16-B4-6	G016927	973.1	22.4	0.0	1549.8	104.1	10.6	960.8	140.3	16.6
BAL16-B4-14	G016928	383.2	0.0	0.0	367.9	52.8	0.0	230.4	40.0	0.0
BAL16-B4-18	G016929	318.9	13.8	0.0	325.9	50.3	6.4	155.5	34.3	5.5
BAL16-B4-24	G016930	533.2	10.1	0.0	382.0	29.4	0.0	157.0	25.8	0.0
BAL16-B4-31	G016931	n/a	n/a	n/a	n/a	n/a	n/a	n/a	n/a	n/a

Table A.4: n-alkane and brGDGT parameters.

Sample ID	**Ext. ID**	**Depth**	**TOC**	**Abs. n-alkane conc.**	**CPI**	**ACL**	**brGDGTs conc.**	**BIT**	**CBT**	**MBT**	**MAT**	**MBT'**	**MAT'**
										Weijers et al. (2007)		**Peterse et al. (2012)**	
		[cm]	**[wt%]**	**[µg g^{-1} TOC]**			**[ng g^{-1} TOC]**				**[°C]**		**[°C]**
BAL16-B2-20	G016921	620	1.4	872.9	9.9	28.2	254.1	0.90	0.53	0.19	-1.5	0.19	3.8
BAL16-B2-26	G016922	945	3.6	545.1	13.1	28.5	166.5	0.96	0.49	0.19	-1.3	0.19	3.8
BAL16-B2-31	G016923	1117	0.7	1842.6	13.6	30.0	0.0	n/a	n/a	n/a	n/a	n/a	n/a
BAL16-B2-39	G016924	1399	1.6	1253.1	9.0	28.6	1276.7	1.00	0.63	0.39	7.6	0.39	9.4
BAL16-B2-1	G016919	1500	4.3	688.4	13.2	29.0	291.8	0.97	0.42	0.20	-0.2	0.20	4.7
BAL16-B2-5	G016920	1600	1.6	1030.0	10.7	28.8	701.3	0.88	0.41	0.18	-1.0	0.18	4.0
BAL16-B4-2	G016925	8	38.9	982.3	12.6	28.6	613.7	1.00	1.85	0.25	-10.9	0.25	-1.9
BAL16-B4-4	G016926	120	8.1	3286.6	8.3	28.5	3036.9	1.00	0.93	0.27	-1.4	0.27	3.9
BAL16-B4-6	G016927	160	8.6	3354.5	8.8	28.6	3777.8	1.00	1.01	0.30	-0.8	0.30	4.3
BAL16-B4-14	G016928	340	2.2	2142.9	9.9	28.9	1074.4	0.99	0.81	0.25	-1.1	0.25	4.0
BAL16-B4-18	G016929	430	4.0	2358.5	7.8	27.7	910.5	1.00	0.76	0.21	-2.4	0.22	3.3
BAL16-B4-24	G016930	583	5.3	1615.8	8.3	27.8	1137.4	1.00	0.99	0.16	-7.3	0.16	0.2
BAL16-B4-31	G016931	798	< 0.1	16444.4	5.7	28.3	0.0	n/a	n/a	n/a	n/a	n/a	n/a

Figure A.1: Example integration n-alkanes

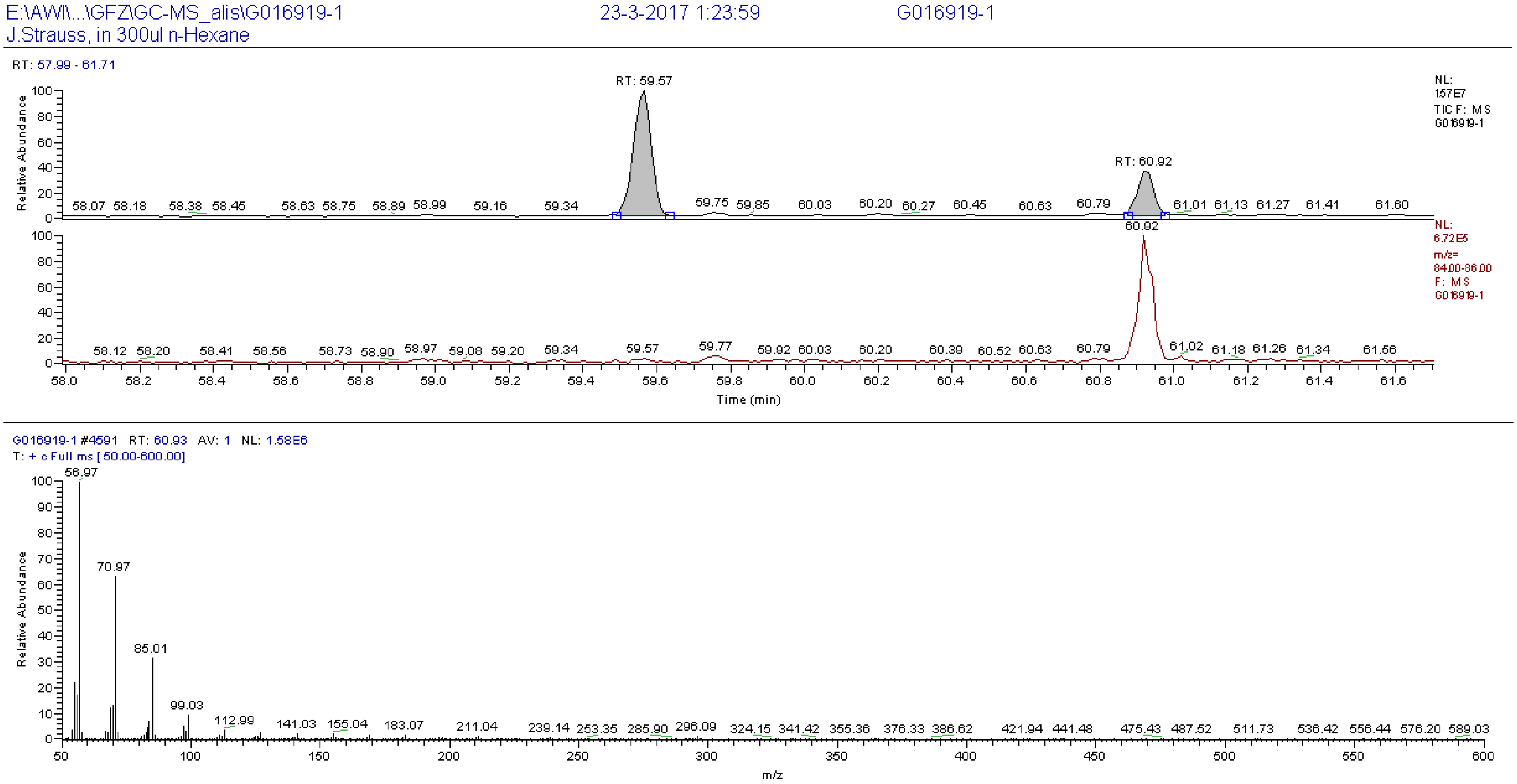

Figure A.2: Example integration brGDGT-III and II

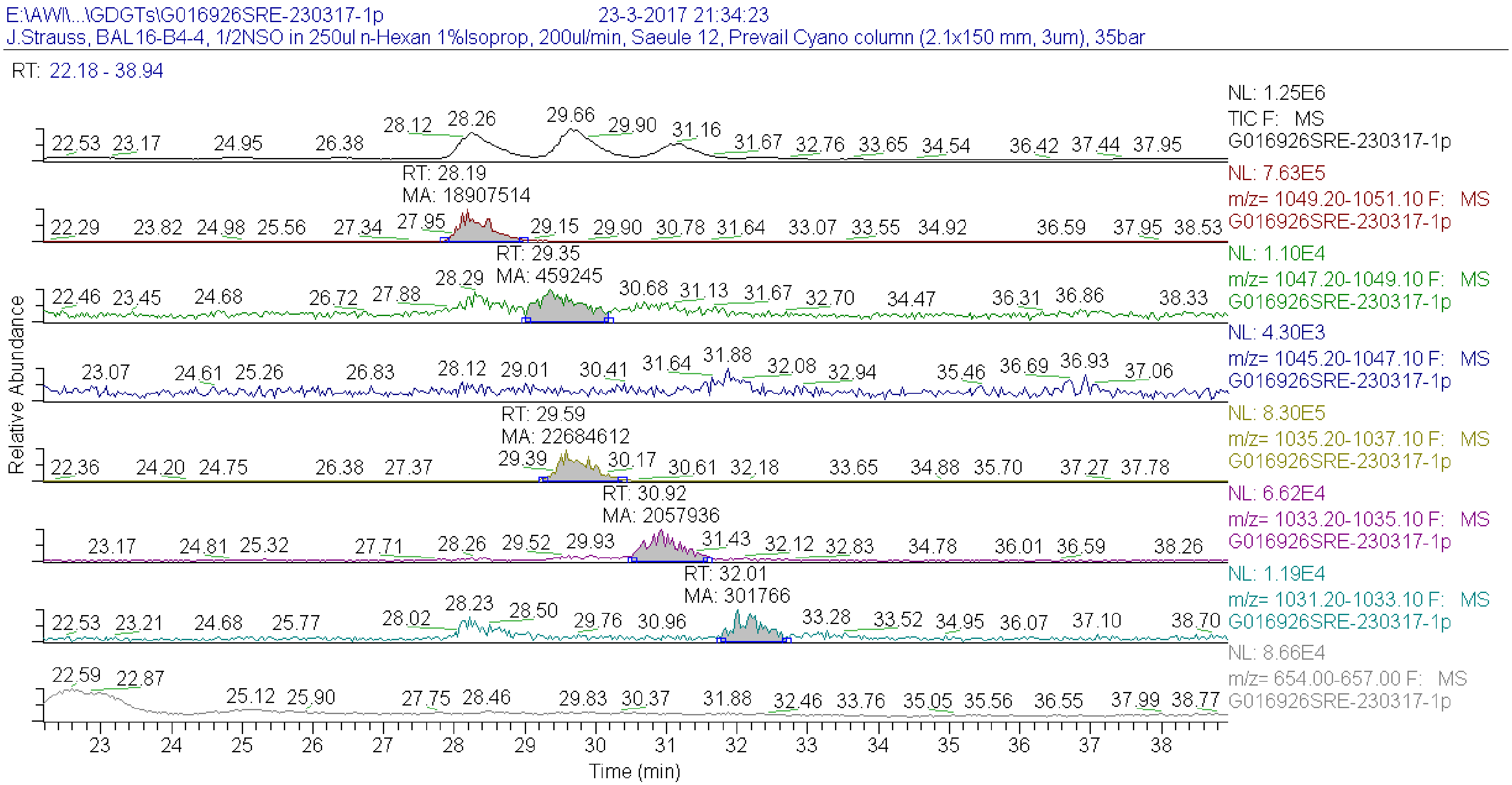

Figure A.3: Example integration brGDGT-I

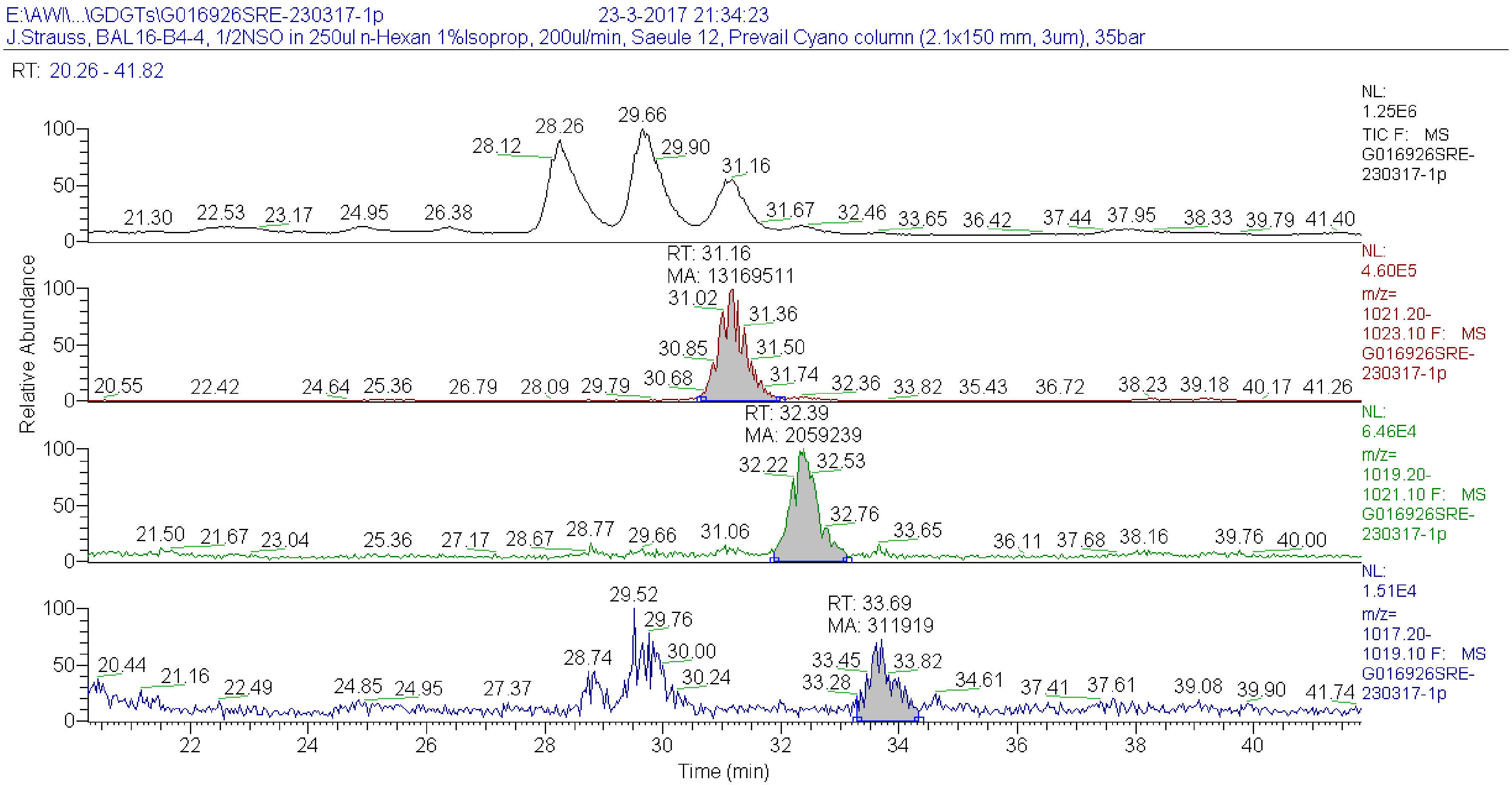

E:\AWI\...\GDGTs\G016926SRE-230317-1p 23-3-2017 21:34:23

J.Strauss, BAL16-B4-4, 1/2NSO in 250ul n-Hexan 1%Isoprop, 200ul/min, Saeule 12, Prevail Cyano column (2.1x150 mm, 3um), 35bar

RT: 20.26 - 41.82

Acknowledgements

This master thesis was carried out at the Alfred Wegener Institute in Potsdam in the section Periglacial Research from December 2016 to June 2017. Therefore, I would first of all like to thank ERC as well as PETA-CARB for making it possible for me to study the wonderful Arctic in this way. And the people of PETA-CARB for a great amount of inspiration.

I thank my internal supervisor Francien Peterse for the remote support and discussion. Many thanks go out to my external supervisors Jens Strauss and Josefine Lenz, who not only supported me all the way, but also made me feel welcome. Also, special thanks go out to my office-mate, guide in the lab, and friend Dyke Scheidemann. I thank Kai Mangelsdorf, Anke Kaminsky, Cornelia Karger from the GFZ for introducing me into the world of biomarkers and helping me out in the lab greatly. Furthermore, I thank my colleagues from AWI for sharing their experiences with me and for the time on the beautiful Telegrafenberg and surroundings.

I say thanks to my loving friends and family who were curious and engaged in my study and time abroad. And last but not least, I thank my parents who have raised my interests and motivations I have today, believe in me every step I take and are always there for me.